# Proceedings of the 23rd International Conference on Biomedical Applications of ELECTRICAL IMPEDANCE TOMOGRAPHY

(EIT 2023)

Edited by Felix Röhren, Florian Voss, Daniel Voss, Patrick Borchers, Steffen Leonhardt

RWTH Aachen University, Germany
12–14 June 2023

This document is the collection of papers accepted for presentation at the

23rd International Conference on Biomedical Applications of Electrical Impedance Tomography
EIT 2023, Aachen, Germany.

Each individual paper in this collection: © 2023 by the indicated authors.
Collected work: © 2023 Felix Röhren, Florian Voss, Daniel Voss, Patrick Borchers, Steffen Leonhardt

**Layout design**:
Marcin J. Kraśny,


Chair for Medical Information Technology
RWTH Aachen University
Pauwelstraße 20,
52074 Aachen
Germany
https://www.medit.hia.rwth-aachen.de/

EIT2023

# Table of Contents

## About the Event

The RWTH Aachen University, and the Chair for Medical Information Technology are pleased to host the 23rd International Conference on Biomedical Applications of Electrical Impedance Tomography (EIT2023).

We are happy to invite everyone to the great city of Aachen for the conference and want to thank for all the support shown by the Electrical Impedance Tomography (EIT) community for the event. Aachen is a hub of scientific research and a vibrant city that has a rich history of innovation and discovery. With its universities, research institutes and industry partnerships, Aachen is the ideal location to bring together leading experts in the field of EIT. We are honored to host this conference and look forward to the exchange of ideas, knowledge and experience that it will bring.
The conference gives a platform for investigators in all aspects of EIT and related areas such as bioimpedance to converse on common fields of interest, whilst also being an opportunity for the community to broaden its outlook in clinical applications and new technologies. We are eager to hear about your contributions to this field and hope that you will make many valuable connections during this event.
We hope you have enjoyable and productive as our guests in Aachen.

EIT 2023 Organizing Committee

## Conference Sponsors





MedST
Profile Area
Medical Science &
Technology
RWTH AACHEN
UNIVERSITY


IFMBE


VDE
DGBMT


mediT
RWTH AACHEN
UNIVERSITY

## Session 1: Thorax I

# Bedside detection of right-to-left intracardiac shunt

Huaiwu He[1], Long Yun[1] and Zhanqi Zhao[2]

[1] Department of Critical Care Medicine, Peking Union Medical College Hospital, Chinese Academy of Medical Sciences, Beijing, China, tjmuhhw@126.com

[2] Institute of Technical Medicine, Furtwangen University, Villingen-Schwenningen, Germany

**Abstract:** An approach to detect right-to-left intracardiac shunt based on the center of heart (CoH) was introduced determined from the early phase of impedance-time curve after hypertonic saline bolus injection. A large shift in CoH was observed in a patient with intracardiac shunt than in the control patients.

## 1 Introduction

Real-time ventilation images assessed by electrical impedance tomography (EIT) have been used to guide individual ventilation setting [1]. Recently, the regional lung perfusion assessment with saline contrast-enhanced EIT is increasingly applied to identify respiratory failure etiologies based on the evaluation of ventilation-perfusion matching [2-4]. The potential use of saline contrast-enhanced EIT as ventriculography was not explored yet. Clinical case reports showed that the radionuclide angiocardiography could be used to detect right-to-left shunt with refractory hypoxemia [5, 6]. Based on the first-pass kinetics theory, we hypothesized that the right ventriculography by saline contrast-enhanced EIT might be feasible to detect right-to-left shunt in refractory hypoxemia. Hereby, we introduce a novel method to detect right-to-left intracardiac shunt using EIT.

## 2 Methods

Functional EIT (fEIT) showing tidal ventilation distribution is calculated by averaging the tidal impedance variation images obtained before the saline bolus injection [7]. The regions with maximum ventilation (in regard of relative impedance change) are identified. The saline contrast method was described in detail in our previous reports [3, 4]. The time of saline injection lasts ~ 1 s and the end of injection is denoted as T0. Saline bolus injection causes a significant impedance drop. When such drop is identified in the maximum ventilation regions, this implies that the saline bolus arrives in the lung regions. This time point is denoted as T1. A moving time window from T0 to T1 is then constructed with steps of 0.5 s. The length of the window is also 0.5 s. The slope of the impedance-time curve in each pixel within the time window is calculated. The fEIT images of saline entering the heart are calculated accordingly using the slope as pixel values. For each fEIT images of saline in heart, maximum slope is identified. Pixel values that are higher than 20% of the maximum are identified as heart region. The center of heart (CoH) (right to left) is calculated as follows:

$$CoH = \sum(x_i \times Slope_i) \Big/ \sum Slope_i \times 100\%$$

where $Slope_i$ is the absolute slope of the impedance-time curve in the corresponding fEIT image for pixel i, and $x_i$ is the pixel location in the image whereby left of the image (right side of the body) is 0% and the right (left side of the body) is 100%. The change of CoH from T0 to T1 indicates the movement of saline bolus in the heart. For patients with right-to-left intracardiac shunt, CoH at T1 should identify the shift of saline to the left heart.

To illustrate how this method works in clinical practice, we calculated the shift of CoH from T0 to T1 in 10 control hypoxic patients without right-to-left shunt.

## 3 Results and conclusions

The shift of CoH between T0 and T1 in the control patients without right-to-left shunt was 1.99±1.43%, whereas the shift in a 41-year-old male patient with right-to-left shunt was 8.82%.

To our best knowledge, this was the first reported concept of right ventriculography for bedside right-to-left intracardiac shunt with EIT. The 10% NaCl bolus, as an EIT contrast agent, passes through right atrium and ventricle, the pulmonary circulation, and left atrium and ventricle, which produces a dilution curve after bolus injection during the apnea period based on the first-pass kinetics theory. With the feature that the saline is concentrated in the right ventricle before it reaches the lung, it could be regarded as a type of right ventriculography. The CoH parameter is proposed to identify the possible intracardiac right-to-left shunt. If the shunt is present, then the saline bolus will arrive in the left ventricle at the early stage prior to lung perfusion. As a result, CoH moves to left side in the right-to-left intracardiac shunt condition. Hence, the change of CoH could be used to assess whether right-to-left intracardiac shunt is present, which could provide an additional information on the etiology of hypoxemia.

## References

[1] H He, Y Chi, Y Yang et al. *Crit Care* 25:230,2021
[2] T Fossali, B Pavlovsky, D Ottolina et al. Crit Care Med. 50:723-32,2022
[3] H He, Y Chi, Y Long et al. *Ann Intensive Care* 11:134, 2021
[4] H He, Y Chi, Y Long et al. Crit Care 24:586, 2020
[5] Z Salimi, J Thomasson, W Vas, A Salimi *Chest* 88:784-6, 1985
[6] R Hussain, Maseeh-uz-Zaman, SA Khan, et al. *J Pak Med Assoc* 56:241-2, 2006
[7] Z Zhao, PJ Yun, YL Kuo et al. Physiol Meas 39:01NT01, 2018

# Pulmonary monitoring with wearable electrical impedance tomography and lung sound registration: a pilot clinical investigation

Inéz Frerichs[1], Rita Paradiso[2], Vassilis Kilintzis[3], Bruno M. Rocha[4], Fabian Braun[5], Michaël Rapin[5], Laura Caldani[2], Nicolaos Beredimas[3], Romanos Trechlis[6], Sander Suursalu[7], Claas Strodthoff[1], Diogo Pessoa[4], Rui P. Paiva[4], Nicolaos Maglaveras[3], Norbert Weiler[1], Josias Wacker[5]

[1]Dept. of Anaesthesiology and Intensive Care Medicine, University Medical Centre Schleswig-Holstein, Campus Kiel, Kiel, Germany, frerichs@anaesthesie.uni-kiel.de; [2]Smartex s.r.l., Pisa, Italy; [3]Aristotle University of Thessaloniki, Laboratory of Medical Informatics, Thessaloniki, Greece; [4]University of Coimbra, Centre for Informatics and Systems, Department of Informatics Engineering – Coimbra, Portugal; [5]Swiss Centre for Electronics and Microtechnology, CSEM, Neuchâtel, Switzerland; [6]Exodus s.a., Research and Development Department, Athens, Greece; [7]Artec Design, Talinn, Estonia

**Abstract:** A wearable device with integrated electrical impedance tomography (EIT), lung sound recording and accelerometry was developed for advanced pulmonary monitoring. Its functionality, safety and user acceptance were successfully examined in a pilot clinical investigation in healthy subjects.

## 1 Introduction

Current wearable lung monitoring devices typically assess only basic respiratory parameters like breathing rate, inspiration and expiration times or relative tidal volume. This information is not sufficient for the lung function assessment of patients suffering from pulmonary diseases which requires the use of auscultation, spirometry and lung imaging.

A vest with 19 multimodal sensors was developed for the purpose of such advanced monitoring (Fig. 1). It offered the measurements of EIT through 256 channels at 40 Hz, skin-electrode contact through 16 channels at 40 Hz, chest sounds through six channels at 5 kHz and accelerometry through one channel at 0.2 Hz. The ability of the wearable to record the intended bio-signals, its safety and wearing comfort were assessed in a first clinical investigation.

## 2 Methods

The study was conducted on 20 healthy adult subjects aged 39 ± 12 years (mean ± SD). It was approved by the Ethics Committee of the Medical Faculty of the Kiel University (A104/21) and the German Institute for Drugs and Medical Devices (94.1.10-5660-13105). It was registered at the German Clinical Trial Registry (DRKS00023703).

Four vests of different sizes in female and male designs were tested. During the examination, the study participants performed various breathing patterns (quiet and deep breathing, slow and forced full expiration, coughing and apnoea) in four different postures according to a 14-step study protocol. The safety of the wearable device was assessed by the number of adverse events. The subjects filled in a questionnaire regarding the properties of the vest and the comfort of wearing. The recorded data was streamed to a study tablet (the quality of the skin-sensor contact, the global EIT and one sound waveform were shown on the screen in real-time), uploaded to a back-end server and analysed offline. EIT waveforms were examined for the presence of baseline drifts, step-like and spike-like disturbances and functional ventilation EIT images for streak and blob artifacts during each measurement phase.

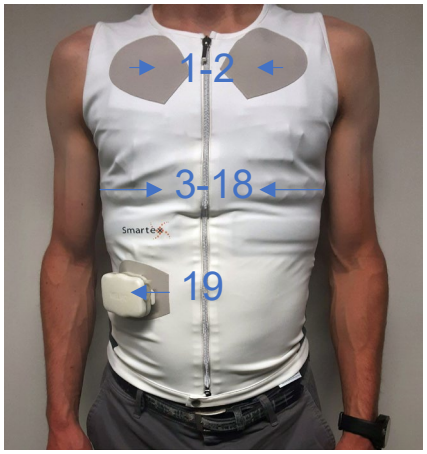


**Figure 1:** Wearable multi-sensor medical device for advanced respiratory monitoring, a male vest model.

## 3 Results

All 20 subjects completed the full study protocol. The vests recorded the data for 934 ± 59 s. Data of two subjects was discarded because of technical issues (a broken wire between the electrodes). The qualitative and quantitative analysis revealed that 89% of EIT waveforms and functional EIT images were of good to excellent quality. Disturbances occurred mainly during coughing and full expiration manoeuvres. Chest acoustic signals with audible heart sounds of good to excellent quality were obtained in 44% to 67% of subjects, depending on the sensor location. Accelerometry correctly identified the posture. No adverse events occurred. The vests were positively rated in the survey, the tactile and thermoregulatory properties of the fabric received the highest scores.

## 4 Conclusions

The multi-sensor vests recorded all the intended bio-signals. The vests were functional, safe and well perceived by the users. They outperformed the predecessor model [1] with respect to the quality of the EIT and sound recordings as well as in the wearing comfort and user friendliness.

## 5 Acknowledgements

The study was funded by the European Commission (Horizon 2020 project WELMO, grant number 825572).

## References

[1] I Frerichs, B Vogt, J Wacker, et al. *Physiol Meas*, 41:015006,2020

# RecruitmEnt Assessed by eleCtRical Impedance Tomography (RECRUIT)

*an international study in COVID-19 ARDS*

Annemijn Jonkman[1,2*], Glasiele Alcala[3*], Bertrand Pavlovski, Oriol Roca, Savino Spadaro, Lu Chen, Jose Dianti, Mayson de Araújo Sousa, Michael Sklar, Gaetano Scaramuzzo, Thomas Piraino, Huiqing Ge, Guang-Qiang Chen, Jian-Xin Zhou, Ewan Goligher, Eduardo Costa, Jordi Mancebo, Tommaso Mauri[4*], Marcelo Amato[3*] & Laurent Brochard[1*] for the PLUG working group. *co-first or co-senior authors;

1. Interdepartmental Division of Critical Care Medicine, University of Toronto, Canada; 2. Intensive Care Medicine, Erasmus Medical Center, Rotterdam, the Netherlands, a.jonkman@erasmusmc.nl; 3. Pulmonology, University of Sao Paulo, São Paulo, Brazil; 4. Anesthesia, Intensive Care and Emergency, Fondazione IRCCS Ca' Granda Ospedale Maggiore Policlinico, Milan, Italy

**Abstract:** In this international study in 108 ventilated COVID-19 patients, we demonstrate the feasibility of EIT for offering a personalized positive end-expiratory pressure (PEEP) adjustment based on the best compromise between lung recruitability and the risks of lung overdistention.

## 1 Introduction

Defining lung recruitability is needed for a safe PEEP selection in mechanically ventilated patients, but no valid method including both recruitability and the risks of overdistention exists when defining optimal PEEP level.

***Objective:*** to describe the range of recruitability using EIT, the effects of PEEP on recruitability, respiratory mechanics and gas exchange, and to describe EIT-based optimal PEEP selection.

## 2 Methods

First (interim) analysis, in patients with COVID-19, from an ongoing international study (NCT04460859) in moderate-severe acute respiratory distress syndrome (ARDS). EIT, ventilator data, hemodynamics and blood gases were obtained during PEEP titration maneuvers.

***EIT-based optimal PEEP*** during a decremental PEEP trial was defined as the crossing point of the overdistention and collapse curves. We also obtained the PEEP level associated with the highest respiratory system compliance.

***Recruitability*** was defined as the amount of modifiable lung collapse when increasing PEEP from 6 to 24 $cmH_2O$ (=$\Delta Collapse_{24\text{-}6}$). Patients were classified as low, medium or high recruiters based on the tertiles of $\Delta Collapse_{24\text{-}6}$.

## 3 Results

In 108 COVID-19 patients, recruitability varied from 0.3% to 66.9% and was unrelated to ARDS severity (Table 1). R/I ratio was higher in higher recruitable patients and correlated with $\Delta Collapse_{24\text{-}6}$ (r=0.52, p=0.001).

**Table 1.** Patient characteristics

| | **Low** (n=36) | **Medium** (n=36) | **High** (n=36) | ***p*** |
|---|---|---|---|---|
| BMI, kg/m² | 28 [25; 32] | 30 [27; 32] | 33*# [27; 39] | 0.01 |
| Age, years | 65 [58; 70] | 61 [54; 65] | 55* [46; 63.5] | <0.01 |
| P/F, mmHg | 113 [97; 134] | 120 [100; 142] | 113 [99; 141] | 0.91 |
| R/I ratio | 0.6 [0.4; 0.8] | 0.8 [0.5; 0.1]* | 0.83 [0.7; 1.0]* | <0.01 |

*R/I, recruitment-to-inflation; p<0.05 diff. from *low or #medium group*

The EIT-based crossing point PEEP level differed between groups (Fig.1, p<0.05) but achieved similar percentages of collapse, overdistention, and respiratory mechanics independent of recruitability (Table 2). This approach assigned a different PEEP level than the highest compliance approach in 81% of patients.

**Table 2.** Mechanics at crossing point PEEP

| | **Low** | **Medium** | **High** | ***p*** |
|---|---|---|---|---|
| Crs, ml/cm$H_2O$ | 29 [24; 38] | 37 [28; 47] | 36 [31; 40] | 0.05 |
| ΔPaw, cm$H_2O$ | 8.2 [7.5; 9.7] | 8.6 [7.1; 10.1] | 8.4 [7.1; 10.9] | 0.92 |
| Collapse, % | 5 [3; 7] | 6 [4; 7] | 5 [3; 6] | 0.22 |
| Overdistention, % | 8 [5; 10] | 8 [7; 10] | 6 [5; 8] | 0.05 |

*Crs, compliance; ΔPaw, driving pressure (with Vt of 5 ml/kgPBW),*

## 4 Conclusions

Recruitability varies widely among COVID-19 patients. EIT allows personalizing PEEP setting as a consistent compromise between recruitability and distension.

Fig.1. Distribution of collapse and overdistention during the decremental PEEP trial.

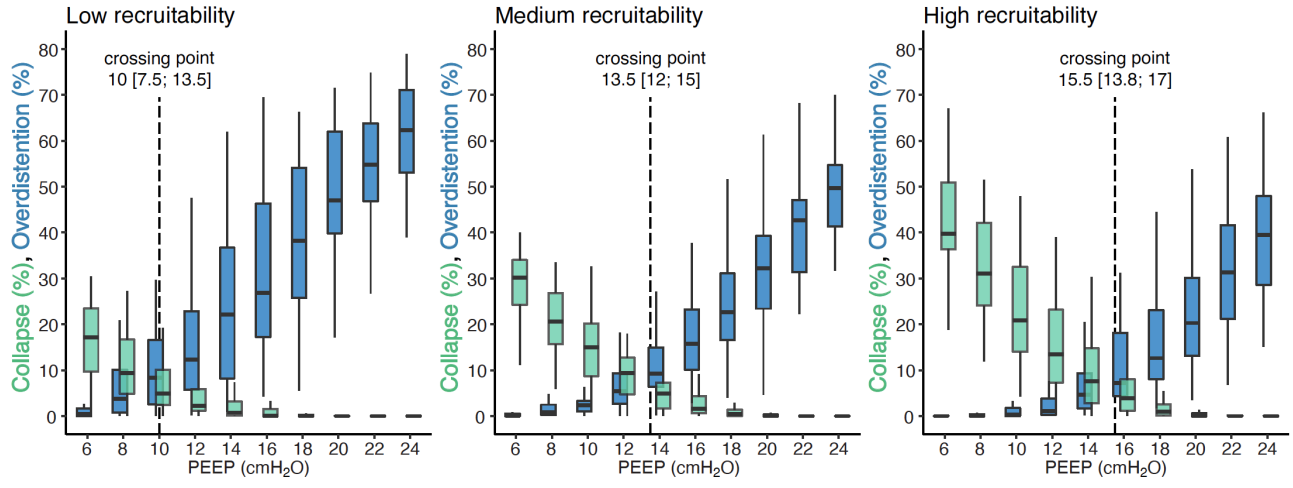

# Perioperative Non-invasive Hemodynamic and Respiratory Monitoring using Electrical Impedance Tomography

You Jeong Jeong[1], Hee Yong Kang[2], Ann Hee You[2], Tong In Oh[1]

[1]Department of Biomedical Engineering, College of Medicine, Kyung Hee University, Seoul, Korea, tioh@khu.ac.kr

[2] Department of Anesthesiology and Pain Medicine, Kyung Hee University, Seoul, Korea

**Abstract:** This study emphasizes the significance of respiratory monitoring to prevent respiratory complications. The study monitored 25 non-intubated patients in the PACU using EIT, capnography, and hemodynamic monitoring to compare preoperative and postoperative recovery after laparoscopic surgery.

## 1 Introduction

Respiratory depression and hypoventilation due to residual anesthetics and the use of opioids cause hypoxemia and hypercapnia. They may lead to permanent disability or life-threatening complications, e.g., organ failure, brain damage, coma, and death, in the post-anesthesia care unit (PACU) [1]. Therefore, respiratory and hemodynamic monitoring are required in these situations. Monitoring peripheral oxygen saturation ($SpO_2$) or end-tidal carbon dioxide ($EtCO_2$) is commonly used to detect hypoxemia or hypercapnia. However, they often trigger false/delayed alarms and cause alarm fatigue. In this study, we used an EIT system with capnography and hemodynamic system to simultaneously measure all tidal volume (TV), respiratory rate (RR), ventilation per minute (MV), $SpO_2$ and $EtCO_2$, SV, and CO measured all. We focused on developing new parameters to evaluate patients' recovery status using estimated data.

## 2 Methods

A clinical trial was conducted in PACU on 25 patients who underwent laparoscopic surgery after general anesthesia. The Capnostream™35 (Medtronic, USA) measured $SpO_2$, $EtCO_2$ derived from the capnography signal[2]. TV and proximal flow were simultaneously measured using an electrical impedance tomography (EIT) device (AirTom™, BiLab, Korea) developed for regional lung ventilation images. We calculated respiratory functional parameters such as global inhomogeneity (GI), dynamic compliance, the center of ventilation (CoVxy), and regional ventilation delay (RVD) [3-5]. In addition, the EIT device and hemodynamic monitor (EV1000, Edwards Lifesciences, USA) were measured simultaneously to compare hemodynamic changes.

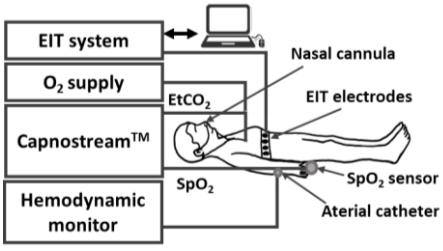


**Figure 1.** Setup for a clinical study.

Fig. 1 shows the clinical study setup. The respiratory status of each patient was monitored for about 30 minutes after being transferred to PACU. During the first half of the period, 4 L/min (36% $FiO_2$) of oxygen was provided to each patient through an oronasal cannula. The institutional review board at Kyung Hee University Hospital approved this clinical study protocol (KHUH-2019-08-058-007). Fig. 2 shows respiratory and hemodynamic signals acquired from patient #19 using AirTom™ with Capnostream™35 and EV1000.

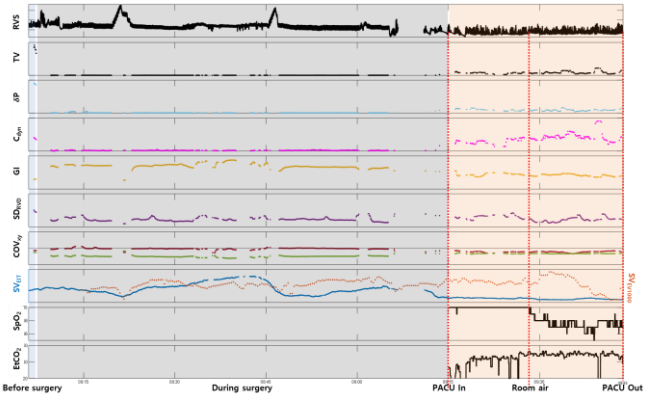


**Figure 2.** Measured respiratory and hemodynamic signals in PACU after finishing laparoscopic surgery with general anesthesia.(blue: before surgery, grey: during surgery, orange: PACU)

## 3 Conclusions

We conducted a study to simultaneously measure respiratory and hemodynamic indices to observe changes when hypoventilation and respiratory events that may occur in a patient perioperative occur. Various indicators, such as GI, $CoV_{xy}$, and dynamic compliance, presented the status of each patient in real time. We focus on developing an integrated indicator that can evaluate the recovery status of patients perioperative.

## 4 Acknowledgments

This research was supported by a National Research Foundation (NRF) grant (NRF-2020R1F1A1077270, NRF-2020R1A2C1008975) funded by the Ministry of Science & ICT in Korea.

## References

[1] LA Lynn, et al., Patient Saf. Surg, 5:3, 2011
[2] M Ronen, et al., J Clin Monit Comput, 31:435-442, 2017
[3] Jang, Geuk Young, et al. Biomed. Eng. Online 18:1-18, 2019
[4] TI Oh, et al., Physiol. Meas, 32:835-849, 2011
[5] GY Jang, et al., Sci Rep, 10:11242, 2020

# Open source software for analysis of chest EIT data acquired during spontaneous breathing and respiratory manoevres

Claas Strodthoff[1] and Inéz Frerichs[1]

[1]Department of Anaesthesiology and Intensive Care Medicine, University Medical Centre Schlewig-Holstein, Campus Kiel, Kiel, Germany claas.strodthoff@uksh.de

**Abstract:** We present the design process of a new software for analysis of spontaneous breathing and respiratory manoevres recorded with thoracic EIT. The software is simple but highly configurable, making it useful for clinicians and researchers alike.

## 1 Introduction

EIT is becoming an increasingly popular tool to monitor and diagnose lung function in mechanically ventilated but also spontaneously breathing patients [1]. So far, software solutions to analyze EIT measurements are targeted at researchers working on a specific study [2]. The requirements for these solutions usually focus on specific devices and particular clinical questions whereas the user experience and configurability are of lower importance. Here we present the design process of a new software for thoracic EIT analysis. Being aimed at both clinicians and researchers, it is simple to use but also highly configurable to fit the needs of different study protocols.

We plan to test this software on data from spontaneously breathing subjects and to compare the results with other lung function measurements in an already running clinical trial.

## 2 Methods

The software was written in Python using the PyQtGraph library for fast interactive plotting. For data processing we used the NumPy and SciPy libraries. Settings are stored as and read from *.json files to allow full configurability.

## 3 Core features

- ☐ Reconstruct EIT images using established algorithms
- ☑ Load pre-reconstructed EIT images
- ☑ Select from a multitude of options: reference interval, filters, regions of interest, breath detection settings
- ☑ Select time intervals and points for analysis with multiple input options
- ☑ Implement numerous analysis parameters/items, see list of implemented items in table 1
- ☑ Output pixel-wise values of all desired items as *.csv (for research use)
- ☐ Output standardized report with most important findings as *.pdf (for clinical use)
- ☑ Configuration file for default values and settings
- ☑ Configuration file for analyses and result generation
- ☐ Documentation of features

## 4 Future features

- ☐ Support for more data formats
- ☐ Integrated visualization/interpretation/aggregation section
- ☐ Automatic detection of certain time points (e.g. begin of forced expiration)
- ☐ Make software open source once core functionality is finished and tested

## 5 Conclusions

The software envisioned here is a large endeavour. We hope that the EIT community will profit from this tool but also hope for community participation to extend its functionality.

## References

[1] I Frerichs Chapter 9 In: A Adler, D Holder: Electrical Impedance Tomography, 2nd Ed., CRC Press, 177-189, 2022

[2] Z Zhao, B Vogt, I Frerichs, U Müller-Lisse, K Möller *Engineering*, 5, 103-107, 2013

**Table 1:** Items implemented in the software. Inspiratory measurements analog to expiratory.

| item | description |
|---|---|
| pixel-wise values from regular breathing | |
| *tidal* | mean tidal impedance variation ("tidal image") |
| *phase* | phase shift of pixel signal vs. summed ("global") signal |
| pixel-wise values from forced respiratory manoevres | |
| *FVC* | forced expiratory vital capacity |
| *FEVx* | forced expiratory volume in time x |
| *MEFxx* | mean expiratory flow at xx % of the forced vital capacity expired |
| *MEFxx-yy)* | mean expiratory flow between xx and yy % of the forced vital capacity expired |
| *tExx* | time to expire xx % of the vital capacity |
| values composed of/calculated from the above | |
| $FEV_1/FVC$ | volume fraction expired after 1 s of forced full expiration |
| $CoV_{rl}$; $CoV_{vd}$ | centre of ventilation left/righ or ventral/dorsal |
| *CV/GII* | coefficient of variation/global inhomogeneity index |
| ... | ... |

# The effect of anti-inflammatory therapy on compliance, alveolar overdistension and collapse in EIT guided PEEP: MaastriCCht cohort

SJH Heines[1], E Aydeniz[1], BCT van Bussel[1], MCG van de Poll[1], ICC van der Horst[1], DCJJ Bergmans[1]

[1]Department of Intensive Care, Maastricht University Medical Centre+, Maastricht, The Netherlands, S.heines@MUMC.nl

**Abstract:** Electrical impedance tomography (EIT) enables alveolar overdistension (OD) and collapse (CL) calculation during a PEEP trial. The effect of dexamethasone and tocilizumab on OD, CL and dynamic respiratory system compliance (Cdyn) in mechanically ventilated patients with coronavirus disease-19 (COVID-19) is described.

## 1 Introduction

It was shown that Cdyn, OD and CL change over time in COVID-19 patients [1]. We hypothesise that therapy with dexamethasone and tocilizumab improves pulmonary function in ventilated patients with COVID-19. This study describes the difference between Cdyn, OD and CL at optimal PEEP in patients who received no anti-inflammatory therapy (NoAIT), dexametazone (DEXA) and DEXA with tocilizumab (DEX+T) in COVID-19 patients.

## 2 Methods

This prospective observational study was conducted in COVID-19 patients of the MaastriCCht cohort, which has been described extensively elsewhere [2]. Optimal EIT-guided PEEP was determined at a level of CL≤5% during a decremental PEEP trial. The level of Cdyn, imported from the ventilator, OD and CL at optimal PEEP was compared between patients with NoAIT, DEXA and DEXA+T. Patients with spontaneous breathing or in prone position were excluded (Figure 1). During the COVID-19 pandemic, EIT measurements (Pulmovista® 500, Dräger Medical GmBH) were performed to support clinical practice.

### 2.1 Statistics

Linear mixed-effects regression with random intercept and random slope with time was conducted between the NoAIT, DEXA and DEXA+T group and over days since intubation. Crude models were adjusted for age, sex and Acute Physiology And Chronic Health Evaluation II score to investigate potential confounding.

### 2.2 Results

Compared with NoAIT, optimal PEEP was 1.4 $cmH_2O$ (-2.6; -0.2) lower in the DEXA group ($p$=.023) and increased 0.1 $cmH_2O$ (0.0; 0.2) per day during admission ($p$=.006). The DEXA+T group showed no significant difference in optimal PEEP. However, an increase of 0.2 $cmH_2O$ (0.1; 0.4) per day during admission was observed ($p$=.004). At optimal PEEP, Cdyn, OD and CL did not differ statistically significant between the three groups.

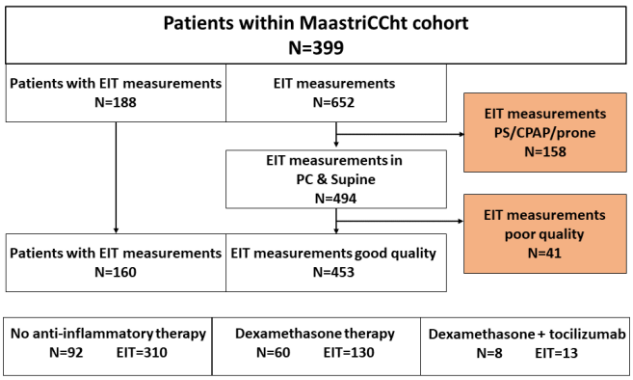


**Figure 1:** Number of patients, EIT measurements and treatment groups.

### 2.3 Discussion

Concerning pulmonary pathophysiology, Cdyn, OD and CL showed that the pattern over time was similar between patients who received NoAIT, DEXA and DEXA+T, which is in line with a previous report [1]. Therefore, the present study did not provide evidence that anti-inflammatory therapy improves pulmonary function in mechanically ventilated COVID-19 patients. However, this study cannot fully rule out the beneficial effect of anti-inflammatory treatment. Anti-inflammatory therapy was not used in the first pandemic wave which had different viral strains that evolved over time, most likely have also influenced these outcomes. The small sample size in the DEXA+T group is a limitation which makes it hard to make conclusions on the effect of the therapy on lung function. Optimal PEEP values were lower during the first 10 days of admission in the DEXA and DEXA+T group compared to the NoAIT group. This indicates less pulmonary support. However, Cdyn, OD and CL did not differ between groups. An explanation for these results could be that patients were included from different waves of the pandemic, in which management of COVID-19 changed.

## 3 Conclusions

Optimal PEEP was lower in the DEXA and DEXA+T group than in the NoAIT group, implying less severe damage. However, Cdyn, OD and CL did not significantly differ which implies no beneficial effect of these therapies.

## 4 Acknowledgements

Not applicable.

## References

[1] S Heines, B van Bussel, M Jong, et al. *Sci Rep*, 12(1):14517, 2022
[2] J Tas, R van Gassel, S Heines, et al. *BMJ Open*, 10(9):e040175, 20

# Observatory study of end-expiratory lung volume and stroke volume changes during obstructive sleep-breathing disordered events

Thi Hang Dang and Tong In Oh

Department of Biomedical Engineering, Kyung Hee, Univerisity, tioh@khu.ac.kr

**Abstract:** Electrical impedance tomography (EIT) obtained in the thorax can simultaneously monitor end-expiratory lung volume change (ΔEELV) and stroke volume change (ΔSV). We observed ΔEELV and ΔSV when occurring obstructive sleep-breathing disordered events for OSA patients. Those were significantly associated when comparing ΔEELV with ΔSV during and after apnea/hypopnea. High variation of ΔEELV due to the severe OSA events induced hemodynamic instability during sleep.

## 1 Introduction

Obstructive sleep apnea (OSA) is the most common sleep-related breathing disorder associated with cardiovascular morbidity and mortality. Repetitive partial or completed occlusion of the upper airway and arousal events with hyperventilation generate intrathoracic pressure changes causing unstable hemodynamic states during sleep [1]. Therefore, ΔEELV affected by upper airway collapsibility could associate with hemodynamic variables [2]. In this study, we observed the relationship between ΔEELV and ΔSV caused by respiratory events during sleep.

## 2 Methods

We have monitored ΔEELV and ΔSV for 30 subjects using AirTom™ (Bilab, Korea) when undergoing full-night level I polysomnography (Embla S7000, Embla Systems, USA) (IRB no. 2019-05-094). A certified sleep technician manually scored measured PSG data following AASM guidelines. The event section of apnea and hypopnea was defined according to the PSG analysis. The post-event section was determined from the end of each event to a maximum of 10 seconds before the next event. In addition, we extracted respiratory volume signal (RVS) and cardiac volume signal (CVS) from the time series of EIT images [3]. After applying a customized motion artifact removal algorithm, we detected valleys and peaks of RVS and CVS. As shown in Fig. 1, the impedance values at the valleys of RVS were defined as the end-expiratory lung impedance (EELI). We calculated ΔEELI as the maximum difference between EELI during the event and post-event sections. ΔEELI was converted to ΔEELV using a scale factor (α) computed from the spirometry. In addition, we calculated stroke volume (SV) from the difference between the peak and valley of CVS in each cardiac cycle. Similar to ΔEELV, ΔSV was defined as the ratio of standard deviation and mean of SV values during the event and post-event sections. For further analysis, we divide all respiratory events into two groups using a threshold of 400 ml ΔEELV. Finally, we compared ΔSV calculated from each group using a two-sample t-test. The statistical analysis was performed using the Matlab software (MathWorks, USA).

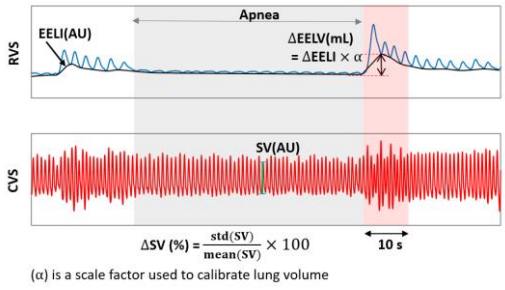


**Figure 1.** Calculation of ΔEELV and ΔSV in an event

## 3 Results

Thirty patients have been involved in PSG and EIT measurements simultaneously, but two failed to obtain them because of the loss of connection during measurement. We processed 4779 apnea/hypopnea events from 28 patients to assess the relationship between ΔEELV and ΔSV. Fig. 2 presents examples of ΔEELV and ΔSV, which belong to each group. The ΔEELV calculated for patient #9 (P9) was significantly larger than that for patient #13 (P13), and the ΔSV for P9 was also prominent when comparing the value for P13. As a result of analyzing all events, we confirmed that ΔSV varied more significantly in the group with a significant change in ΔEELV.

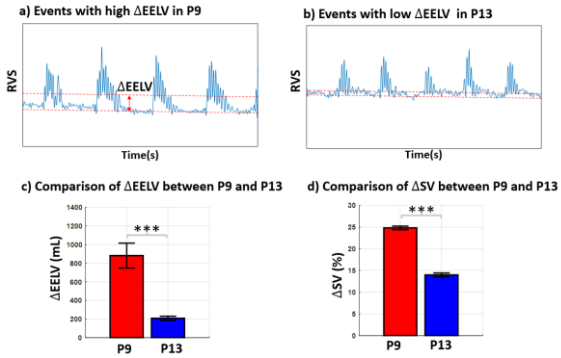


**Figure 2.** Examples of respiratory events with high ΔEELV (P9) and low ΔEELV (P13). Comparison ΔSV calculated from events with high ΔEELV and low ΔEELV. ***p<0.001

## 4 Conclusions

The results indicated a significant association between ΔEELV and ΔSV in OSA events. These findings suggest that the ΔEELV should be considered when assessing hemodynamic instability during the PSG test.

## 5 Acknowledgements

Research was supported by the National Research Foundation of Korea (NRF) fund (NRF-2020R1A2C1008975) and MOTIE(20006024) in Korea.

## References

[1] TD Bradley, *Chest*, 2001, 119(6),pp.1827-1835
[2] RL Owens *Journal of applied physiology*, 2010, 108(2),pp.445-451
[3] GK Jang *Scientific Reports*, 2020, 10(1),pp.1-12

# Respiratory Rate Monitoring in ICU patients and healthy volunteers using EIT: A validation study

J. Wisse-Smit[1, 2], T. Goos[2, 3], A. Jonkman[1], H. Endeman[1], I. Reiss[2], D. Gommers[1]

[1]Department of Adult Intensive Care, Erasmus Medical Centre, the Netherlands, j.j.smit@erasmusmc.nl

[2]Department of Paediatrics, Division of Neonatology, Erasmus Medical Centre – Sophia Children's Hospital, Rotterdam, The Netherlands

[3]Department of Biomechanical Engineering, Faculty of Mechanical, Maritime and Materials Engineering, Delft University of Technology, Delft, The Netherlands

**Abstract:** The objective was to determine the accuracy of the respiratory rate (RR) provided by EIT compared to the gold standard clinical count of $etCO_2$ capnogram and ECG-derived bioimpedance RR. The results obtained support the EIT device's claims for RR accuracy with an root mean square error smaller than 2 breaths per minute.

## 1 Introduction

Respiratory rate (RR) is considered one of the most informative vital signals, such as for predicting patient's deterioration. [1] The gold standard RR measurement in intensive care unit (ICU) patients is RR derived from monitoring of End Tidal $CO_2$ ($etCO_2$) by capnography. We investigated the accuracy of the RR provided by a relatively new EIT device LuMon, (Sentec AG, Landquart, Switzerland)) in spontaneous breathing healthy volunteers and invasively ventilated and spontaneous breathing ICU patients. EIT-derived RR was primarily compared to the RR from capnography. ECG-derived bioimpedance RR (Dräger Infinity M540), which is the reference standard for RR monitoring of spontaneously breathing non-intubated patients in our ICU was also used for comparison.

## 2 Methods

Twenty healthy volunteers were equipped with an EIT belt and ECG electrodes and were asked to breathe through a mainstream end-tidal $CO_2$ capnogram at different frequencies in the range of 10-40 breaths per minute (BMP) for continuous and simultaneous measurement of RR derived from EIT (EIT-RR), capnography (Capnogram-RR) and ECG bioimpedance (Bioimpedance-RR). In 26 ICU patients, similar measurements were obtained in a three-day period surrounding weaning, including spontaneous breathing trials, mechanical ventilation and spontaneous breathing after extubation. For the selection of intervals to be extracted and compared, which is particularly relevant in ICU patients with highly variable conditions, stable breathing sequences were first selected by adapting the algorithm of Haris et al. [2]

To evaluate agreement between different methods, the following analyses were computed: 1.) Correlation and regression analysis with estimates of slope and intercept along with confidence intervals (CIs) of the estimates, considering repeated measurements and using bootstrap resampling approach for the confidence intervals; Deming and linear regression were used. 2.) ARMS (root mean square) accuracy. 3.) Bias and precision with Bland-Altman analysis for repeated measurements, using bootstrap resampling for the confidence intervals of limits of agreement (LOAs).

## 3 Results

The results of the regression analysis of the healthy volunteers showed slopes very close to 1 with tight CIs and low RMS errors <0.3. The Bland-Altman analysis determined a bias less than 0.1 BPM, the LOA including their CIs are tight and within ±1 BPM (Table 1). All regressions exhibited in the analysis of ICU patients resulted in slopes very close to 1 with low RMS-errors <0.5. The Bland-Altman analysis resulted in a bias smaller than 0.14 for all on-ventilator and off-ventilator comparisons with LOAs below ± 1.1 BPM (Table 1). RR determination was excellent across the range of 10-40 BPM obtained in heathy volunteers and patients in the ICU setting.

## 4 Conclusion

During stable breathing periods in healthy volunteers and ICU patients, the LuMon EIT device has excellent accuracy in monitoring respiratory rate.

## 5 Acknowledgements

This project was funded by Sentec AG.

## References

[1] C.P. Subbe, *Sensors*. 18 (8), 2700, 2018
[2] K. Haris, *Physiol. Meas.* 42 (6), 64003, 2021

**Table 1:** Summary of the Bland-Altman bias and limits of agreement (LOA) for the healthy volunteers and ICU patients. Comparing the respiratory rate as measured by EIT (EIT-RR), RR by the $etCO_2$ Capnogram (Capnogram-RR), RR from ECG derived bioimpedance measurement from the vital monitor (Bioimpedance-RR).

| Cohort, Ventilator(On/Off), Number(n) | Comparison | Bias (BPM) | SD (BPM) | Lower LOA | Upper LOA |
|---|---|---|---|---|---|
| Healthy Volunteer (Off), n=20 | EIT-RR vs Capnogram-RR | -0.007 | 0.267 | -0.531 | 0.518 |
| Healthy Volunteer (Off), n=20 | Bioimpedance-RR vs Capnogram-RR | -0.039 | 0.202 | -0.435 | 0.357 |
| ICU patient (On), n=26 | EIT-RR vs Capnogram-RR | 0.126 | 0.481 | -0.816 | 1.068 |
| ICU patient (On), n=26 | Bioimpedance-RR vs Capnogram-RR | -0.016 | 0.236 | -0.478 | 0.446 |
| ICU patient (On), n=26 | EIT-RR vs Bioimpedance-RR | 0.138 | 0.490 | -0.822 | 1.099 |
| ICU patient (Off), n=26 | EIT-RR vs Bioimpedance-RR | 0.079 | 0.408 | -0.721 | 0.878 |

# Predicting spirometry indicators using EIT for lung disease patients

Fedi Zouari[1], Wang C. Kwok[2], Adrien Touboul[1], Pak To Cheung[1], Venice Sin[1], Eddie C. Wong[1], Iris Y. Zhou[3], Terence C. C. Tam[2], Russell W. Chan[1,*]

[1]Gense Technologies Limited, Hong Kong, China, russell@gense.tech
[2]Department of Medicine, Li Ka Shing Faculty of Medicine, The University of Hong Kong, Hong Kong, China
[3]Department of Radiology, Harvard Medical School, Harvard University, Boston, Massachusetts, USA

**Abstract:** Here, we train and validate a regression model to predict spirometry indicators in lung disease subjects using electrical impedance tomography (EIT). Subjects' anthropometric are used to counterweight the change of impedance due to body compositions. The results show significant correlation between EIT and spirometry.

## 1 Introduction

Spirometry is the gold standard lung function assessment. It uses the measured airflow under forced breathing scenario to diagnose different obstructive and resistive pulmonary diseases. Time-difference electrical impedance tomography (tdEIT) provides dynamic changes of the conductivity in a cross-section of the thorax.
Predicting spirometry indicators from EIT conductivity measurements can empower the use of EIT in screening or/and diagnosing pulmonary diseases. This paper builds on our previous study [1] where we show that EIT can predict spirometry indicators on healthy subjects. Here, we expand our results to lung disease patients.

## 2 Methods

### 2.1 Data acquisition

We recruited 70+ subjects, including 24 healthy and 46 patients with respiratory diseases to perform simultaneous spirometry (Vmax 22 Encore system, Carefusion GmbH, Germany) and EIT (Mediscan, Gense Technologies Ltd., Hong Kong) tests. All experiments are performed with subject's informed consent and following the guidelines and regulations approved by the Hong Kong West Cluster (IRB/REC No. UW 21-644). The clinical trial is registered on ClinicalTrials.gov (NCT05346081). Lung disease patients include 12 interstitial lung disease (ILD), 10 asthma, 8 chronic obstructive pulmonary disease (COPD), 8 bronchiectasis, and 8 with other diseases including left pneumonectomy, lung cancer, lung tumor, lymphangioleiomyomatosis, motor neuron disease, heart failure and bronchiolitis obliterans syndrome.

### 2.2 Data analysis

EIT voltage measurements are pre-processed and used to reconstruct conductivity images using the Newton's one-step error reconstructor (NOSER), which are then filtered spatially and temporally. A global conductivity-time curve is obtained by a weighted sum of the conductivity curves at all pixels. Spirometry indicators are computed from the conductivity curve following the standardization consensus [2], namely, the full vital capacity (FVC), forced exhale volume in one second (FEV1) and the Tiffeneau-Pinelli index (FEV1/FVC). The indicators measured using EIT and subjects' anthropometrics are used to predict the ground truth spirometry indicators using a linear regression model. The model parameters are obtained from the training data which excluded data for testing that comprise all data from 10 randomly selected subjects and another 10% of the data from the remaining subjects.

## 3 Conclusions

EIT indicators are significantly correlated with spirometry both on the train and test sets (Figure 1), indicating its potential use for diagnostic screening of pulmonary diseases. Furthermore, EIT also provide spatial and structural information about lungs' health and can be used for other applications such as liver [3]and kidney [4].

## References

[1]F. Zouari *et al.*, *Sci Rep*, vol. 12, no. 1, p. 20613, Nov. 2022, doi: 10.1038/s41598-022-24330-2.
[2]M. R. Miller, *Eur Respir J*, vol. 26, pp. 319–338, 2005.
[3]A. Touboul *et al.*, EMBC, doi: 10.1109/EMBC48229.2022.9871313
[4]D. Yap *et al.,NDT,* doi: 10.1093/ndt/gfac069.013.

**Figure 1:** Correlation between measured spirometry indicators and predicted indicators from EIT.

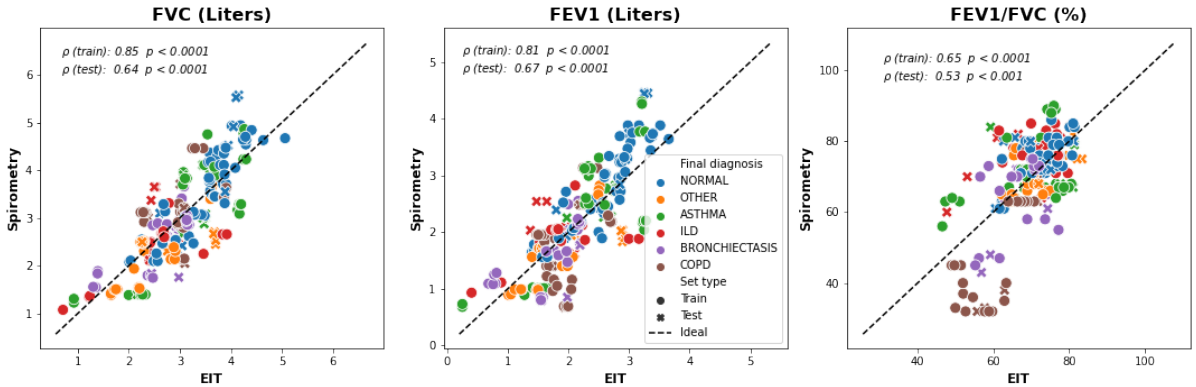

# Regional ventilation in healthy and COPD during breathing exercises

Lin Yang[1], Meng Dai[2], Yifan Liu[2], Feng Fu[2] and Zhanqi Zhao[2]

[1]Department of Aerospace Medicine, The Fourth Military Medical University, Xi'an, China; [2]Department of Biomedical Engineering, The Fourth Military Medical University, Xi'an, China. daimeng@fmmu.edu.cn

**Abstract:** In the present study, we demonstrated for the first time the influences of breathing exercises on regional ventilation in healthy and COPD subjects. The influences in healthy volunteers were systematic. On the other hand, the effects of breathing exercises varied in COPD patients with larger inter-subject variations.

## 1 Introduction

Chronic obstructive pulmonary disease (COPD) is a prevalent lung disease associated with high mortality. Breathing exercises, as part pulmonary rehabilitation, is important for COPD patients to improve their quality of life [1]. Pursed lip breathing and diaphragmatic breathing are two common breathing techniques that help ease the COPD symptoms and improve lung functions [2]. Although these breathing techniques have been widely used in COPD pulmonary rehabilitation programs, the effects on regional ventilation were unclear.

With EIT to assess the regional ventilation and flow limitation, we have initiated a study with the intention to examine the home breathing exercise effects on ventilation inhomogeneity in patients suffering COPD and the potential to optimize rehabilitation program for such patient group. We hypothesized that the respiratory exercises have uniform effects on ventilation in healthy subjects but the effects varied in COPD patients.

## 2 Methods

The prospective observational study was approved by the ethics committee of the Fourth Military Medical University (KY20224101-1). Informed consent was obtained from all subjects prior to the study. A total of 30 healthy volunteers (age, 25.83±0.65 years; height, 176.9±5.84 cm; weight, 74.77±11.65 kg) and 9 COPD patients (age, 68.67±9.71 years; height, 170.11±7.18 cm; weight, 68.00±10.69 kg; 4 subjects GOLD-2, 3 GOLD-3 and 2 GOLD-4) were included. Data were recorded continuously during a period of quiet tidal breathing followed by (1) diaphragmatic breathing; (2) pursed lip breathing with full inhalation; (3) pursed lip combining diaphragmatic breathing. A 10-min training session of the breathing exercises was conducted for all subjects. The EIT examinations were performed while the subjects were seated and instructed not to speak or to move their upper torso during the data acquisition. The sequence of the 3 breathing exercises was randomized using machine generated random permutation.

Spatial and temporal ventilation distributions were evaluated with EIT, including tidal variation (TV), change of end-expiratory lung impedance (EELI), center of ventilation (CoV), the global inhomogeneity index (GI) and regional ventilation delay (RVD). The exact calculation of these parameters were described in the consensus paper [3].

## 3 Results

TV was significantly larger during varous breathing exercises compared to quiet tidal breathing, in both healthy and COPD subjects ($p<0.01$). However, for other EIT-based parameters, statistical significances were only observed in healthy volunteers, not in COPD patients. Diaphragmatic breathing alone might not be able to decrease functional residual capacity in COPD and the effect varied largely from patient to patient (6:3, decrease vs. increase). Ventilation distribution moved towards ventral regions in healthy during breathing exercises ($p<0.0001$). Although this trend was observed in the COPD, however, the differences were not significant. Ventilation became more homogeneous when diaphragmatic breathing technique was implemented ($p<0.0001$). Again, the improvements were not significant in COPD. Regional ventilation delay was relatively high in COPD and comparable in various breathing periods.

## 4 Discussion and Conclusions

Pursed lip breathing and diaphragmatic breathing techniques are easy to learn, and patients can practice at home to ease the symptoms [2]. In the control cohort, we found that these breathing exercises can increase lung ventilation through active inhalation and exhalation (TV and EELI). Besides, ventilation redistributed towards ventral regions (CoV) and introduce a slightly higher temporal ventilation difference (RVD). Diaphragmatic breathing improves ventilation homogeneity while pursed lip breathing does not (GI). The impacts of breathing exercises were relatively consistent on the healthy subjects examined in the study. Although similar trends were observed in the COPD patients, the variation of impacts of breathing exercises was much larger, which led to statistically insignificant results. Some patients benefited from diaphragmatic breathing and were able to lower their functional residual capacity while the others not. Pursed lip breathing on the other hand was able to lower the functional residual capacity but not necessary the ventilation homogeneity. The variation of impacts on COPD patients could be due to individual pathological status.

The impact of pursed lip and diaphragmatic breathing varied in different COPD patients. Breathing exercise may need to be individualized to maximize the training efficacy.

## References

[1] A Hasanpour Dehkordi et al., *Expert Rev Respir Med*, 15:161-9,2020
[2] Y Yang et al., *Physiother Theory Pract,* 38:847-57,2020.
[3] I Frerichs et al., *Thorax*, 72:83-93,2017.

# Monitoring Induction of General Anaesthesia

Silke Borgmann[1,2], Kim Linz[1,2], Sara Lozano[1,2], Johannes Schmidt[1,2], Sashko Spassov[1,2], Christin Wenzel[1,2], Stefan Schumann[1,2]

[1]Department of Anesthesiology and Critical Care, Medical Center, University of Freiburg, Freiburg, Germany
[2]Faculty of Medicine, University of Freiburg, Freiburg, Germany, silke.borgmann@uniklinik-freiburg.de

**Abstract:** Induction of general anaesthesia has a considerable impact on the lung. Monitoring induction of anaesthesia from spontaneous breathing until established mechanical ventilation with EIT in obese patients, we found that the onset of changes induced by mechanical ventilation starts from the first breath under mechanical ventilation.

## 1 Introduction

General anaesthesia is undoubtedly a vital part of modern medicine. Despite this, conditions of the lung change during general anaesthesia until mechanical ventilation is established [1]. Particularly, tidal volume is redistributed from dorsal to ventral areas of the lung, functional residual capacity reduces and the homogeneity of ventilation distribution degrades. It has already been shown that changes within the ventilation conditions of the lung occur five to ten minutes after induction of anaesthesia [2]. These changes are potentially more harmful for obese patients, since atelectatic areas can be found in these patients already during spontaneous breathing [3]. Using EIT, we monitored the process of anaesthesia induction in obese patients from spontaneously breathing to established mechanical ventilation.

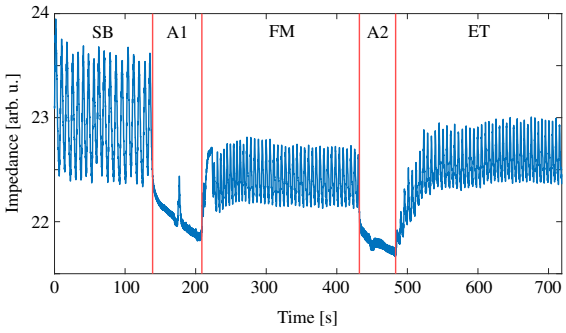


**Figure 1:** The different phases during induction of anaesthesia as seen in the global impedance curve extracted from EIT measurements. In the beginning, the patients breathed spontaneously (SB). After breathing ceased (first apnoe phase, A1), ventilation was provided via facial mask until the muscle relaxant took effect (FM). Subsequently, patients were intubated (second apnoe phase, A2) and mechanically ventilated after endotracheal tube placement (ET).

## 2 Methods

We studied 15 lung-healthy obese (body mass index $> 30$ kg/m$^2$) adult patients. Exclusion criteria were an American Society of Anesthesiologists physical status $>$ III, pregnancy, active implants, rapid sequence induction or suspected difficult airway. Patients were equipped with an electrode belt for EIT measurements and with routine monitoring. Anaesthesia was induced following the standard protocol of our hospital. This included supine positioning with 30° elevated upper body. Monitoring via EIT started with the awake patient breathing spontaneously and was continued during ventilation via a facial mask and subsequent intubation until mechanical ventilation was established Fig. 1.

After image reconstruction (EIT Data Analysis Tool 6.1, Dräger medical, Lübeck, Germany) we calculated the tidal variation [4] and the global inhomogeneity index [5]. For the phase of spontaneous breathing we used an average over all breaths while for each mechanical ventilation phase, we used the first breath only.

## 3 Results

During spontaneous breathing, regional ventilation mainly distributed to the ventral part of the lung ($56 \pm 9$ %). During mechanical ventilation the ventral share was further increased (face mask ventilation: $79 \pm 8$ %; established ventilation via tube: $78 \pm 8$ %, both cases $p < 0.0001$).

The global inhomogeneity index was higher during mask ventilation and intubated ventilation than during spontaneous breathing (all $p < 0.005$, Fig. 2).

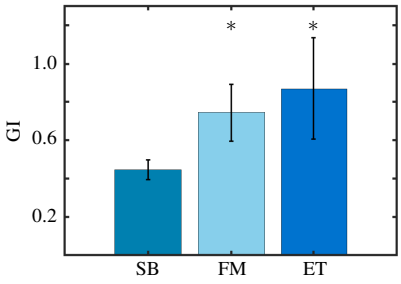


**Figure 2:** Global inhomogeneity index during spontaneous breathing (SB), face mask ventilation (FM) and established ventilation via tube (ET). $*$ marks a significance against SB.

## 4 Conclusions

Changes in lung ventilation are present with the first breath after each apnoeic phase in obese patients. The first apnoe phase of anaesthesia induction had much more impact on the first breaths than the second apnoe phase in obese patients.

## References

[1] G Hedenstierna, L Edmark *Intensive Care Medicine*, 31:1327–1335, 2005
[2] C Bruells, R Rossaint *European Journal of Anaesthesiology*, 28:570–579, 2011
[3] Eichenberger et al. *Anesthesia and Analgesia*, 95:1788–1792, 2002
[4] Frerichs et al. *Thorax*, 72:83–93, 2017
[5] Z Zhao et al. *Critical Care*, 13:P51

# Correlation between hypertonic saline transit time measured with EIT and cardiac output

M. Leali[1], E. Spinelli[2], A. Damia[1], I. Marongiu[1,2], M. Battistin[3], S. Oldoni[3], Z. Zhao[5], S. Gatti[3], T. Mauri[1,2†]

1. Department of Pathophysiology and Transplantation, University of Milan, Italy 2. Department of Anesthesia, Critical Care and Emergency, Fondazione IRCCS Ca' Granda Ospedale Maggiore Policlinico, Milan, Italy 3. Center for Preclinical Research, Fondazione IRCCS Ca' Granda, Ospedale Maggiore Policlinico, Milan, Italy 4. Furtwangen University, Institute of Technical Medicine, Villingen-Schwenningen, Germany † Correspondence to tommaso.mauri@unimi.it.

**Abstract:** Here we analysed EIT data from experiments in healthy swine models undergoing one or two lung mechanical ventilation for 24 hours. We measured the heart-to-lung and right-to-left heart transit times of a 10 ml bolus of hypertonic saline by EIT and tested their correlation with cardiac output measured by transpulmonary thermodilution.

## 1 Introduction

Assessing the trend over time of cardiac output is essential to guide personalised fluid resuscitation, to verify the impact of mechanical ventilation settings and to follow up recovery from myocardial injury. Pulmonary artery catheters (PAC) remain the clinical gold standard for measuring cardiac output, but less invasive monitoring should be developed. To date, most systems still require an arterial catheter and, possibly, a central line [1]. Here we explored the correlation between cardiac output and .the transit time (TT) of a hypertonic saline bolus measured by electrical impedance tomography (EIT). Significant correlation could suggest a potential for less invasive monitoring for trends of cardiac output over time by EIT plus a central line.

## 2 Methods

The study was approved by the Italian Ministry of Health, Rome, Italy (Aut. No. 246/2022-PR, Protocol No. 568EB.34 (ex 32)). We analysed data from 28 healthy swine studied in our laboratory, comprising n=134 independent cardiac output (CO) measurements performed with the thermodilution method (Vigilance, Edwards, US) by means of a PAC. Immediately after, EIT data were acquired at a 50 Hz sampling frequency (Pulmovista, Drager, Germany). An end-inspiratory pause was performed and a 10 ml bolus of 5% NaCl was injected via jugular central line [2]. These measures were performed after 2, 6, 12, 18 and 24 hours of controlled mechanical one-lung ventilation with tidal volume 7.5 ml/kg (OLV7.5, n=46), with tidal volume 15 ml/kg (OLV15, n=58) and two-lung ventilation with tidal volume 15 ml/kg (n=30). The impedance change corresponding to the hypertonic bolus flowing through the pulmonary circulation was analysed. Baseline drift was subtracted by piecewise linear fitting, as previously described [3]. Indicator transit time through lung circulation was modelled as a gamma-variate, which was fitted to data with the method of moments [4]. The fitted curve was then subtracted to data, so that three peaks corresponding to saline passage through the right heart (RH), the lungs and the left heart (LH) were apparent (Fig. 1A-B).

For each of the three peaks the first order temporal moment was calculated as in equation (1).

$$\mu'_1 = \frac{-\sum t*Z(t)}{\sum C\,(t)} \quad (1)$$

Z(t) is impedance over time and t is time

The right heart to lung ($TT_{RH\text{-}lung}$) and the right to left heart ($TT_{RH\text{-}LH}$) transit times were calculated as the difference between the corresponding moments.

Coefficients of correlation and p-values were calculated from Spearman's rank correlation.

## 3 Results

Cardiac output ranged between 1.7 and 6.8 l/min. We disclosed a significant non-linear correlation between cardiac output and both transit times: $TT_{RH\text{-}lung}$ ($\rho$=-0.41; $p<0.001$) and $TT_{RH\text{-}LH}$ ($\rho$=-0.45; $p<0.001$) (Fig. 1C-D).

## 4 Conclusions

Hypertonic saline transit times measured by EIT are correlated with cardiac output and could be used as a less invasive measure to assess CO trends over time.

## References

[1] JL Teboul, et al. *Intensive Care Medicine*, 42: 1350–1359, 2016.
[2] E Spinelli, et al. *Critical Care* 2021;25(1):192.
[3] M Kircher et al. *IEEE Trans on Med Imaging*, 40: 251–261, 2021.
[4] HK Thompson, et al. *Circulation Research*, 14:502–515, 1964.

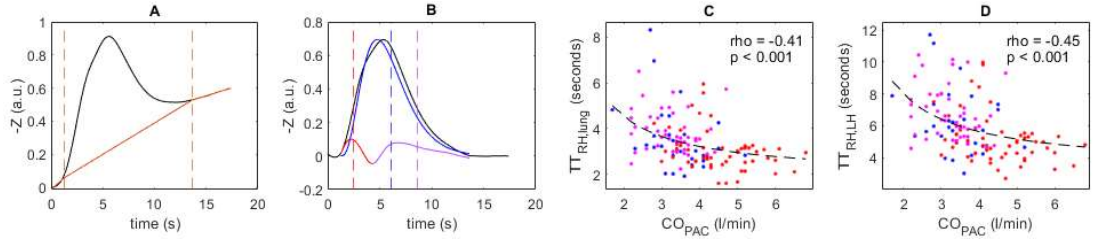


**Figure 1:** A – Impedance change due to the hypertonic saline bolus. Bolus arrival and end time are displayed as orange dashed lines, the estimated drift as an orange solid line. B – Impedance after detrending (black line). Blue line is the fitted gamma-variate, passage through the right and left heart are displayed respectively as a red and a purple solid line. First temporal moments are identified by vertical dashed lines of corresponding colours. C and D – transit times plotted versus cardiac output measured at the PAC, blue dots correspond to controls, red dots to OLV7.5, magenta dots to OLV15 animals (see text).

# Comparison of phrenic nerve stimulated breathing to mandatory ventilation using EIT in a pig model

Dmitrij Ziles[1*], Matthias Manfred Deininger[1*], Teresa Seemann[1], Arnhold Lohse[2], Carl-Friedrich Benner[2], Marian Walter[2], Steffen Leonhardt[2], Thomas Breuer[1]

[1] Department of Intensive and Intermediate Care, Medical Faculty, RWTH Aachen University, Aachen, Germany, dziles@ukaachen.de
[2] Chair for Medical Information Technology, Helmholtz-Institute for Biomedical Engineering, RWTH Aachen University, Aachen, Germany
* Both authors contributed equally

**Abstract:** We established a pig model for direct breath-by-breath comparison of mechanical ventilation (MV) with phrenic nerve stimulated breathing (PNS) and used EIT to support our hypothesis that breaths delivered by PNS yield a better prevention of compression atelectasis in dorsal lung areas than MV.

## 1 Introduction

MV is a life-saving treatment for critically ill patients in the intensive care unit (ICU) with respiratory failure. However, MV is associated with several disadvantages, including preferential ventilation of ventral lung segments, thus resulting in dorsal atelectasis. The latter is associated with complications e.g., increased pneumonic risk, decreased oxygen-intake [1]. One possible solution might be active diaphragmatic stimulation by PNS. We hypothesize that active diaphragmatic contraction may lead to improved ventilation of the dorsal lung segments.

## 2 Methods

### 2.1 General Experimental setup

Therefore, we established a PNS model in juvenile female German landrace pigs (40-50 kilograms) under deep general anaesthesia. Two nerve stimulation needles were placed bilateral in a minimal invasive, sonographic-guided manner transcutaneous in proximity to phrenic nerve. Using a custom-built stimulator-ventilator-device, we were able to switch between PNS and MV breath-by-breath, allowing a direct comparison of the two ventilation methods. We maintained a lung-protective ventilation at 4-6 ml/kg body weight with a constant PEEP of 5 cm $H_2O$. EIT (PulmoVista 500, Dräger, Lübeck, Germany) was used to investigate ventilation of caudal lung segments.

### 2.2 Data analysis

The geometrical center of the ventilated area in the EIT image (CoV) can be described by x and y coordinate pairs each between 0 and 1. The y-axis describes the ventro-dorsal axis and larger values represent a more dorsally located CoV [2]. In the present study, CoV was calculated for 500 breaths of PSV and MV separately breath-by-breath. Comparison between the MV and PNS groups were made by a non-parametric Mann-Whitney-U-Test. Significance was defined as $p < 0.05$. Statistical analysis was performed using Prism 9.0 (GraphPad Software Inc., San Diego, CA, USA). All statistical tests are two-tailed.

## 3 Results

The analysis showed a larger tidal volume fraction in the dorsal region (region of interest 3, ROI 3) under PNS in the qualitative breath-by-breath comparison (Fig. 1 a, b) and in the quantitative CoV analysis a significantly higher y-value for both pigs (Fig. 1 c).

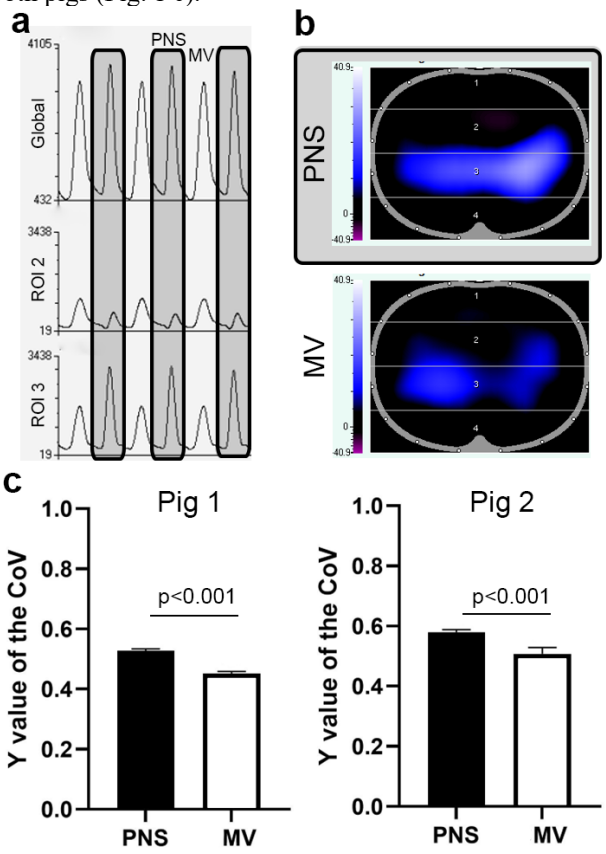


Fig. 1: a illustrates sample impedance curves of global and region of interest (ROI 2 and 3) breath-by-breath changes between PNS and MV ventilation mode. b depicts exemplary tidal images during maximum inspiration generated for PNS and MV. Ventilated lung areas are colored blue. c shows the quantitative analysis of geometrical center of the ventilated area (CoV) separately for the two pigs. Mean + SD is illustrated.

## 4 Conclusions

EIT seems to be suitable as an evaluation method for direct breath-by-breath analysis of different ventilation methods. As an example, in this study we were able to illustrate a higher fraction of ventilation of dorsal lung segments and a higher CoV y-value during PNS breaths compared to MV.

## References

[1] Rohrs, E. C., Bassi, T. G., Fernandez, K. C., Ornowska, M., Nicholas, M., Wittmann, J. C., & Reynolds, S. C. Journal of Applied Physiology, 131(1), 290–301. 2021
[2] Sobota, V., & Roubik, K. (2016). *IFMBE Proceedings*, *57*, pp.1264–1269, Pathos, Cyprus, March 2016

# Functional image of separated ventilation and cardiac activity in EIT

Alberto Battistel[1], Rongqing Chen[1], Erik Stein[1], Noël Hallemans[2,3], Knut Möller[1]

[1]Institute of Technical Medicine (ITeM), Furtwangen University (HFU), Jakob-Kienzle-Strasse 17, 78054 Villingen-Schwenningen, Germany

[2]Department ELEC, Vrije Universiteit Brussel, Belgium

[3]WMG, University of Warwick, UK

**Abstract:** Although primary used for monitoring ventilation, Electrical Impedance Tomography (EIT) can also give valuable information regarding cardiac activity. In this contribution we show a set of functional images which display the spatial intensity and relative phase of both the ventilation and the cardiac activity.

## 1 Introduction

Given the large impedance variation of the lungs during the respiration, Electrical Impedance Tomography (EIT) is routinely used to monitor the ventilation of a patient.

However, information associated with the cardiac cycle are also present [1]. These are likely connected with the volume changes, deformation in the heart, and with the shifting of structures produced by the cardiac dynamics [1]. Unfortunately, in a standard EIT setup, the intensity of the cardiac-related signals is much lower than that of the ventilation [1].

We propose to separate the ventilation and cardiac-related signals in EIT through an harmonic analysis [2, 3].

As schematized in the first row of Fig. 1, the impedance trend at every pixel of a series of EIT images can be expressed as an amplitude modulation of the harmonics of the ventilation $\mathbb{V}$ and cardiac-related signal $\mathbb{C}$ [2, 3].

$$p(t) = \sum_{f \in \mathbb{V} \cup \mathbb{C}} g_f(t)\cos(2\pi f t) - h_f(t)\sin(2\pi f t) \quad (1)$$

where $g_f(t)$ and $h_f(t)$ are the in-phase and out-of-phase modulations at the frequency $f$, respectively, and they can be expressed through suitable polynomials [4].

Taking independently the frequencies belonging to $\mathbb{V}$ and to $\mathbb{C}$, the ventilation and cardiac-related signal can be reconstructed separately (see second row of Fig. 1).

From the polynomials $g_f(t)$ and $h_f(t)$ one can calculate the amplitude for the ventilation and cardiac-related signal for every pixel. These amplitudes can be used to construct two functional images, $A_V$ and $A_C$, (third row of Fig. 1) which respectively map the local magnitude of the ventilation and cardiac activity at every pixel. Similar functional images are also possible for the phase $\phi_f$.

## 2 Methods

The reliability of the functional image reconstruction based on the harmonic separation of the ventilation and cardiac-related signals was tested on a set of simulated data as well as on clinical data.

The pixel-wise algorithm was based on the extraction of the principal component (PCA) of the impedance trends.

## 3 Results

The functional images, $A_V$ and $A_C$, clearly identified the location of maximal activity for ventilation and cardiac dynamics. For the simulated data, $A_V$ and $A_C$ well matched the ground truth. For the clinical data, the location of maximal activity for the ventilation and for the cardiac activity fell at the expected position of lungs and heart, respectively.

The phase-related functional images showed clear phase delay between the region of maximal activity and the surrounding areas. However the interpretation of these images is at the moment not clear.

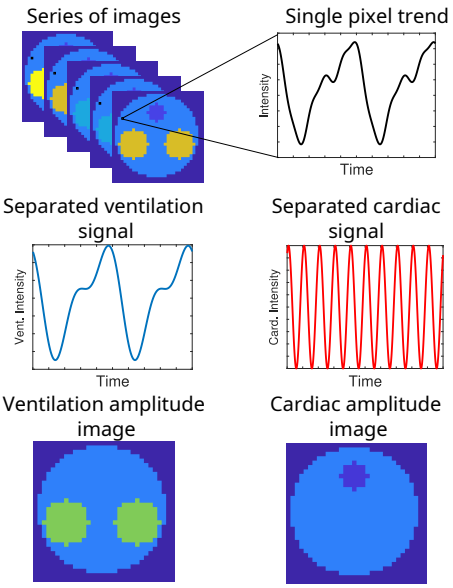


**Figure 1:** Schematic to represent the procedure to construct EIT functional images from a series of EIT frames.

## 4 Conclusions

Through harmonic analysis it is possible to create EIT functional images which display the region of maximal activity of the ventilation and cardiac dynamics.

## 5 Acknowledgments

This research was partially funded by the BMBF (MOVE, Grant 13FH628IX6), H2020 MSCA Rise (#872488 DCPM), and AIRLobe (32-7545.220/42/1).

## References

[1] JM Deibele, H Luepschen, S Leonhardt *Physiol. Meas.*, 29: S1–S14, 2008

[2] A Battistel, C Rongqing, N Hallemans, R Pintelon, J Lataire, K Möller, *IFAC-PapersOnLine*, 54: 281–286, 2021

[3] A Battistel, C Rongqing, N Hallemans, R Pintelon, J Lataire, J Lovas, K Möller, *AUTOMED 2021* , Basel, Switzerland, 2021

[4] N Hallemans, R Pintelon, X Zhu, T Collet, R Claessens, B Wouters, A Hubin, J Lataire *IEEE Trans. Instrum. Meas*, 70: 1–14, 2021

# Regional ventilation characteristics in infants after liver transplantation: A pilot study

Xiaolan Chen[2], Chen Chen[1], Leiqin Gao[1], Yuan Gao[1], Yuxiao Deng[1], Zhe Li[1] and Zhanqi Zhao[3]

[1]Shanghai Jiao Tong University School of Medicine Affiliated Renji Hospital, Shanghai, China. slamy1987@126.com
[2] Shanghai Pulmonary Hospital, Shanghai, China.
[3]Furtwangen University, VS-Schwenningen, Germany.

**Abstract:** In the present study, we explored the ventilation variations in infants after pediatric liver transplantation with electrical impedance tomography.

## 1 Introduction

Pediatric liver transplantation (PLT) is currently the most effective treatment for end-stage liver disease in children [1]. The liver and lungs are anatomically adjacent, and pulmonary complications are a common and major risk factor for postoperative mortality and prolonged stay in the intensive care unit (ICU) in PLT patients [2,3]. However, due to the limitations of bedside respiratory monitoring techniques in children, the postoperative respiratory status of PLT recipients is poorly studied.

The present study aimed to describe the physiological changes of ventilation variations during controlled mechanical ventilation (MV), spontaneous breathing trial (SBT), and weaning process and to explore the phenotypic pattern of the postoperative ventilatory status after PLT by EIT.

## 2 Methods

The prospective observational study was approved by the Local Ethics Committee (LY2002-025-B). Informed consent was obtained from the patients' parents prior to the study. A total of 5 patients (9.23±2.17 months; height, 65.23 ± 6.99 cm; weight, 6.72 ± 2.98 kg) who were transferred to the ICU under postoperative anesthesia were included. All patients underwent 5 phases measurements with EIT (VenTom-100, MidasMED Biomedical Technology, Suzhou, China): 1) MV (Assist-Control mode); 2) pressure support ventilation (PSV) of 15/5 $cmH_2O$; 3) SBT (low-level PSV 12/3 cmH2O for 2h); 4) right after weaning; 5) day 2 after weaning. Successful SBT was defined as: 1) $SPO_2 \geqq 95\%$; 2) Exhale tidal volume ≧5ml/kg (ideal weight); 3) Respiratory rate: 20-60bpm (<6 months) or 15-45bpm (6 to 24 months). Clinical data such as gender, age, Pediatric End Stage Liver Disease (PELD) score, and respiratory parameters such as the PaO2/FiO2 ratio and vital signs were collected.

EIT records at 5 phases were collected. The tidal impedance variation (TIV) was evaluated.

## 3 Results

The left lung ventilation of all 5 patients was poor on the first day of MV after surgery. After extubation, the right side ventilation of 3 patients increased compared with that before (Fig. 1). However, one patient had extremely uneven ventilation distribution after extubation, which showed that the left lung ventilation increased and the right lung ventilation significantly decreased (Pat. 4, Fig. 2). We screened the chest X-ray and found that the right diaphragm of this patient moved up (Fig. 2).

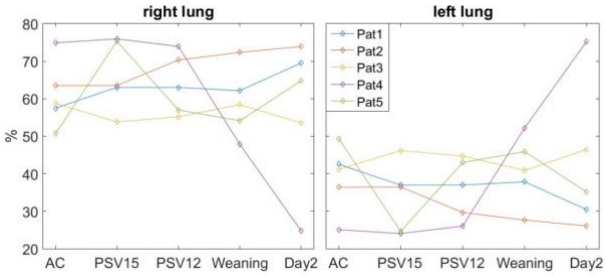


Figure 1. Variations of ventilation distribution between right and left lungs after pediatric liver transplantation. X-axis: five phases

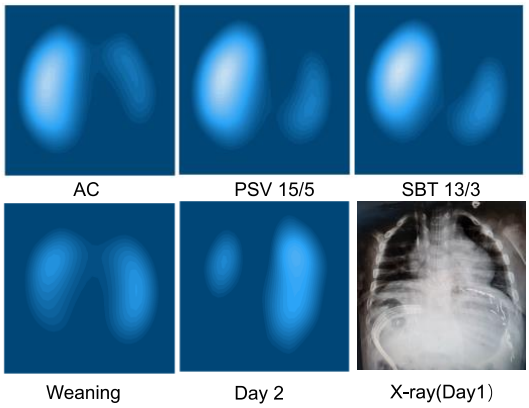


Figure 2. Representative EIT images of ventilation distributions and the Chest X-ray of Patient 4

## 4 Discussion and Conclusions

We conducted ventilation monitoring for the first time in infants after PLT. We found that the gas distribution of all patients was mainly on the right side and their recovery varied from patient to patient. We speculate that due to the injury of the left diaphragm caused by PLT, positive pressure ventilation would result in higher gas flow into the right lung. After the recovery of spontaneous respiration, the right diaphragm compensation makes more increased ventilation than before. Nevertheless, the current findings suggest there is a need for bedside monitoring of respiratory recovery after PLT to provide intervention promptly.

### References

[1] M Spada et al. *World J Gastroenterol* 15:648–74, 2009.
[2] C Araz et al. *Transplant Proc*. 36:214-7, 2004
**[3]** OO Nafiu et al. *Anesthesiol Res Pract* 2017:3728289,2017

# $\dot{V}/\dot{Q}$ analysis with 3D EIT

Joaquin Araos[1], Symon Stowe[2], Andy Adler[2]

[1]Dept Clinical Science, College of Veterinary Medicine, Cornell University, Ithaca, USA
[2]Systems and Computer Engineering, Carleton University, Ottawa, Canada

**Abstract:** Bedside measurement of $\dot{V}/\dot{Q}$ matching with EIT has clinical potential. Previous work showed feasibility in 2D, but 3D lung heterogeneity is significant. We demonstrate $\dot{V}/\dot{Q}$ in 3D in data from pigs. Additionally, analysis software is made available.

## 1 Introduction

Critically ill patients often have significant alterations in gas exchange. Regional matching of ventilation and perfusion ($\dot{V}/\dot{Q}$) is key to ensure optimal gas exchange in the lungs, and thus the importance of bedside monitoring of $\dot{V}/\dot{Q}$ matching. However, even healthy lungs are highly heterogeneous, and current work in EIT-based $\dot{V}/\dot{Q}$ only describes a single 2D image of the thorax [1]. In this study, we develop a two-plane, 3D analysis of regional $\dot{V}/\dot{Q}$.

While EIT-based measurement of air flow ($\dot{V}$) is well understood, work on perfusion ($\dot{Q}$) is ongoing, and both pusatility- and conductivity bolus-based techniques are used. In all techniques, lung perfusion analysis requires complex signal processing techniques to remove the cardiac component. We developed a software tool using a first pass kinetics bolus approach [1] to determine pulmonary blood flow and report regional $\dot{V}/\dot{Q}$. This software is made available (see [3]) to allow comparisons of the signal processing.

## 2 Methods

With ethics approval, eight female, Yorkshire cross pigs (four months, 55–59 kg, were included. Pigs were sedated anesthetized and mechanically ventilated in a supine position. Standard ICU clinical parameters were monitored. A Swan-Ganz catheter was floated to the pulmonary artery and used to inject saline bolus (10 mL of 7.2% hypertonic saline) during an 30 s apnea. The study consisted of phases designed to modify $\dot{Q}$: Baseline, Dobutamine infusion, Phenylephrine infusion, and Controlled hemorrhage. EIT data were recorded at 47.7 frames/s using a Sentec Pioneer Set and a custom-made, $2\times16$ electrode EIT belt was placed over the shaved chest region. Three transverse EIT image layers were reconstructed [2].

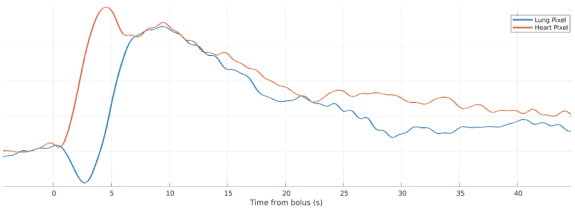


**Figure 1:** Heart and Lung voxels after bolus injection.

Ventilation images were generated by ensemble averaging over multiple breaths. Perfusion imaging followed the approach of [1]. Voxels corresponding to the heart and lungs were identified manually, the propagation of the bolus through the heart was fit to a gamma function. This function was then fit to all other image voxels and subtracted to yield the lung-perfusion signal (see Fig 1).

The $\dot{V}/\dot{Q}$ ratio for each voxel was calculated using the 3D ventilation, $\Delta Z_{\dot{V},\mathrm{vox}}$, and perfusion, $\Delta Z_{\dot{Q},\mathrm{vox}}$, distributions. Units were calculated using tidal volume ($V_T$), respiratory rate ($RR$), cardiac output ($CO$) and dead space fraction ($V_D/V_T$), calculated using the Bohr equation:

$$\frac{\dot{V}_{\mathrm{vox}}}{\dot{Q}_{\mathrm{vox}}} = \frac{\frac{\Delta Z_{\dot{V},\mathrm{vox}}}{\Delta Z_{\dot{V},\mathrm{tot}}} \times V_T \times RR \times (1-\frac{V_D}{V_T})}{\frac{\Delta Z_{\dot{Q},\mathrm{vox}}}{\Delta Z_{\dot{Q},\mathrm{tot}}} \times CO} \quad (1)$$

This equation can be motivated as follows: impedance ratios represent the unitless fraction of impedance change in each voxel. Conversion to $\dot{V}$ and $\dot{Q}$ units requires multiplication by air and blood flows: $V_T \times RR \times (1-\frac{V_D}{V_T})$ represents effective alveolar ventilation.

## 3 Results & Discussion

Using these calculations, it is possible to calculate 3D EIT image of the distributions of $\dot{V}$,$\dot{Q}$ and their ratio $\dot{V}/\dot{Q}$ (Fig 2). Note the variability of all parameters across the planes, with a ventral movement in the anterior plane.

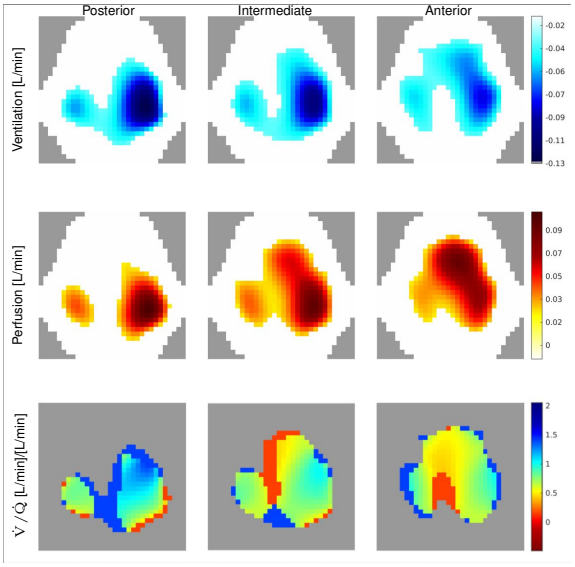


**Figure 2:** Example (cranial, intermediate and caudal) image slices in an animal. Top: Ventilation, Center: Perfusion, Bottom: $\dot{V}/\dot{Q}$.

In this paper, we are motivated by the importance of monitoring the 3D distribution of $\dot{V}/\dot{Q}$ matching, which would be important clinically due to the heterogeneous nature of these phenomena. We conducted experiments and developed analysis software software to demonstrate feasibility. To further collaboration, software have been released [3] under the GPL license.

## References

[1] JB Borges *et al* J Appl Physiol 112:225–236 2012
[2] B Grychtol *et al* Physiol Meas 40:074006 2019
[3] J Araos *et al*, sf.net/p/eidors3d/code/HEAD/tree/trunk/dev/VQ_analyze/ "$\dot{V}/\dot{Q}$ analysis software", 2023

# A model of a rat thorax with a two-compartmental lung surrogate

Silke Borgmann[1,2], Patryk Dzierzawski[1,2], Bernd Flamm[1,2], Sashko Spassov[1,2], Christin Wenzel[1,2], Stefan Schumann[1,2]

[1]Department of Anesthesiology and Critical Care, Medical Center, University of Freiburg, Freiburg, Germany
[2]Faculty of Medicine, University of Freiburg, Freiburg, Germany silke.borgmann@uniklinik-freiburg.de

**Abstract:** Studies in physical models can spare experiments on live animals. We propose an enhanced model for a rat thorax and lung comprising a latex balloon filled with saline-cooked agar agar and a urinary catheter with a cuff. The cuff was modified to model two compartments which fill sequentially. We confirmed the filling pattern using EIT.

## 1 Introduction

A main part of clinical research is comprised of pre-clinical studies mostly done on animals. Small animals make up the vast majority of animal studies. In Germany alone, the fraction of animal studies using small animals amounts to more than 80% [1]. We have already developed a model of the rat thorax, enabling testing of a dedicated EIT device for monitoring lung function of rats [2]. Such a model not only helps reducing animal experiments but also may provide standardized test conditions which is favourable for testing of hardware components and for developing image reconstruction methods. We modified our previous model by using a cuff with a partially reinforced contour. This resulted in two compartments which fill after one another and thus simulate a temporal delay in recruitment.

## 2 Methods

The main part of the rat thorax model comprises a latex balloon filled with saline (NaCl 0.9%, Braun, B. Braun Melsungen AG, Melsungen, Germany) cooked agar agar (Carl Roth GmbH+Co.KG, Karlsruhe, Germany). The balloon skin was reinforced with latex milk (natural rubber, kept liquid with ammonia) to enable the penetration of the sixteen subdermal hooked needle electrodes (GVB- geliMED GmbH, Bad Segeberg, Germany) used for EIT imaging. As a substitute for the lung, we placed a urinary catheter with inflatable cuff inside the balloon. The main tube of the catheter was blocked to make it air-tight. Inflation of the cuff simulated inspiration of air, deflation of the cuff simulated expiration accordingly. The cuff itself was reinforced with a thin strip of latex milk (natural rubber, kept liquid with ammonia) spanning its contour from pole to pole on opposite sides (Fig. 1).

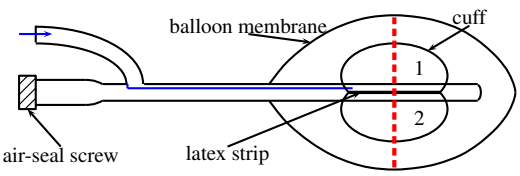


**Figure 1:** Schematic drawing of the rat model and the modified cuff. The rat model is comprised of a latex balloon that is filled with saline-cooked agar agar. The inflated cuff of the urinary catheter is reinforced with a latex strip spanning its contour from pole to pole creating two compartments (1 and 2). Inflation was done using air applied via a syringe into the cuff lumen (blue arrow). A screw was used as air-seal for the main lumen of the catheter. The red dashed line marks the electrode plane.

This strip divided the cuff into two compartments with a local minimum in cuff diameter at the position of the strip. Due to this modification and the inflation from one side, the two compartments are filled after one another and separated spatially by the strip. The inflation itself was done manually via syringe.

For EIT imaging we used the Sciospec EIT32 system in sixteen electrode mode. We chose an adjacent injection pattern with 5 mA injection current and 10 kHz frequency.

For image reconstruction we used the dedicated Sciospec software that is based on a circular finite element model and a Newton-Raphson reconstruction algorithm. EIT imaging showed, that after applying volume with the syringe, the first compartment was filled quickly. It took 1.4 seconds of continued application of air for the second compartment to start filling as well (Fig. 2). The peripheral position observed in the EIT images was confirmed by visual inspection while shining light through the model.

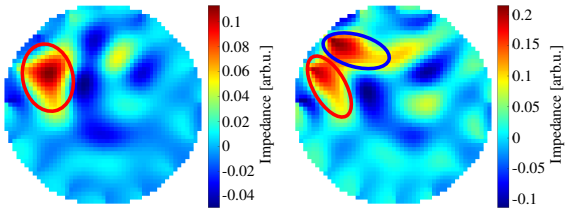


**Figure 2:** Filling of the cuff as visualized with EIT. First, only one compartment was filled (left image, red ellipse). After 1.4 seconds of continuing application of air via the syringe, the second compartment started to fill as well (right image, first compartment red ellipse, second compartment blue ellipse).

## 3 Conclusions

We could visualize the two compartments as well as their filling behaviour using EIT in the described configuration. The modified cuff together with the rat thorax model was suitable to test EIT measurements and the appropriate settings.

## 4 Acknowledgements

This work was funded by the Deutsche Forschungsgemeinschaft under grant DFG SCHU 2499/13-1.

## References

[1] Bericht des Bundesministeriums für Ernährung und Landwirtschaft 2021
[2] Borgmann et al., Proceedings of the International Conference of Bioelectromagnetism, Electrical Bioimpedance, and Electrical Impedance Tomography 2022

# Electrical impedance tomogrphy and ultrasound tomography for lung imaging

Manuchehr Soleimani[1] and Tomasz Rymarczyk[2]

[1]M. Soleimani is with the Electrical and Electronic Engineering Department, University of Bath, UK, ms350@bath.ac.uk
[2]T. Rymarczyk is with Research & Development Centre Netrix S.A., Wojciechowska 31, 20-704 Lublin, Poland. (Email: tomasz@rymarczyk.com)

**Abstract:** The dual mode EIT and ultrasound imaging have been studied extensively. In this study, we consider the EIT and the transmission mode ultrasound tomography (UST) for lung imaging. The article presents an experimental phantom study involving both EIT and UST in lung imaging. Two rings of 16 electrodes EIT and two rings of 16 transducers in UST are deployed allowing volumetric imaging for both modalities.

## 1 Introduction

Electrical impedance tomography (EIT) is an established and clinically approved tool for lung imaging [1]. For example, the EIT provides vital information on lung ventilation in ICU units. On the other hand, the FDA has approved ultrasound tomography (UST) for breast cancer screening. The UST produces high-quality images for breast cancer detection [2]. The subject of this presentation is the application of UST imaging as a complementary or alternative imaging modality to the EIT. Clinical ultrasound imaging is generally carried out in a few MHz, mainly on reflection mode boundary imaging. To do a transmission mode UST imaging in a complex medium such as the thorax, a lower frequency (less than 700 kHz) may be more suitable. In our phantom study a 400 kHz excitation for the UST.

## 2 Results

Figure 1 shows the sensor arrangement for both EIT and UST sensors in a thoracic-like shape phantom. The 3D images are created in time difference imaging mode for both. For the 3D UST imaging a ray-based forward model and a total variation regularisation reconstruction algorithm are used and for the 3D EIT, a finite element based forward model from EIDORS and a Tikhonov-based regularisation method are used. For measurement data acquisition, a phantom was built using Netrix and UST 3.0, and EIT 2.1 tomographs (Figure 2) is used. Figure 3 shows the central slice from a 3D UST reconstruction when the air was dynamically pumped in and removed from the left lung. The results of measurements using the EIT technique are shown in Figure 4, where the image reconstruction is presented for both filled lungs and one lung pumped out and the other wholly filled.

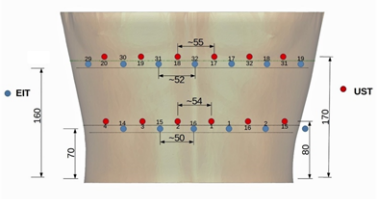


Figure 1: Sensor configuration for UST and EIT

Figure 2: Measuring system using Netrix UST 3.0 and EIT 2.1 tomographs

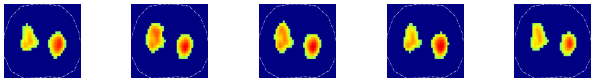

Figure 3: UST Image with changes in air volume on the left lung

a)

b)

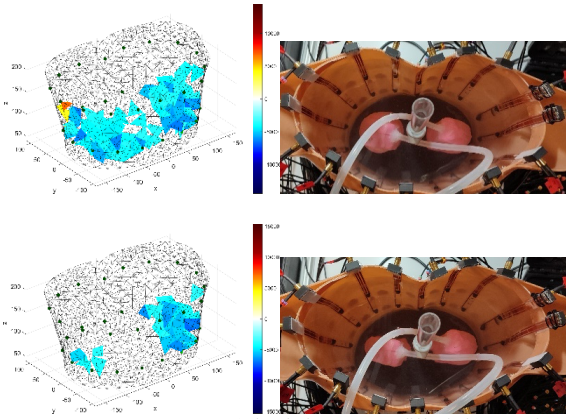

Figure 4: EIT Image 3D, a) both lungs are filled, b) one lung is pumped out, and the other lung is filled

## 3 Conclusions

This paper makes a first step experimental evaluation of the UST and EIT system for possible use in lung imaging. In addition, comparisons between the two modalities will be presented. We will further explore the opportunities for image fusion taking advantage of both modalities. In particular the image fusion will be used for the EIT with enhanced imaging near the boundary, and the UST with better image quality in the central imaging area. This can lead to more reliable lung imaging with safe, low cost and radition free imaging modalities.

## References

[1] C. Li, *et al.*; "Comparison of ultrasound attenuation tomography methods for breast imaging," Med. Imaging 2008 Ultrason. Imaging Signal Process., vol. 6920, p. 692015.
[2] Frerichs I, *et al.*; "TREND Study Group. Chest electrical impedance tomography examination, data analysis, terminology, clinical use and recommendations: consensus statement of the TRanslational EIT developmeNt stuDy group. " *Thorax* 2017;72:83–9.

# EIT-based synchronized positive pressure ventilation in newborns

Andy Adler[1], Andreas D Waldmann[2], Christoph M Rüegger[3]

[1]Systems and Computer Engineering, Carleton University, Ottawa, Canada
[2]Department of Anaesthesiology and Intensive Care Medicine, Ros- tock University Medical Center, Germany
[3]Newborn Research, Department of Neonatology, University Hospital and University of Zürich, Switzerland

**Abstract:** Synchronizing ventilation with patient efforts is associated with improved outcomes, but it is challenging to reliably detect weak breathing efforts without false positives. We propose that electrical impedance tomography (EIT) may allow improved and more accurate detection of the breath efforts. Retrospective data is analyzed to suggest that such EIT-based detection could be useful.

## 1 Introduction

Synchronized ventilation is widely used in neonatal care and associated with improved outcomes[1, 2]. Commonly used methods for synchronization include pneumatic capsules, flow or pressure sensors, and neurally adjusted ventilator assist (NAVA) [3]. During noninvasive ventilation, synchronization with the baby's breaths is challenging, requiring enough sensitivity to detect weak breathing efforts, while avoiding auto-triggering with nasal or oral leaks. Another concern is if the ventilator is triggered by the opening/closing of the glottis, leading to triggered breaths which ventilate the pharynx rather than the lungs.

Electrical impedance tomography (EIT) uses body-surface electrodes to image the ventilation distribution. We propose that the EIT signal may be particularly useful to improve patient-ventilator synchrony in the neonatal population.

## 2 Methods & Results

EIT data were recorded during spontaneous tidal ven- tilation in a five-week-old preterm infant (26 weeks gestational age at birth) as part of a larger study (ACTRN12616001516471). During regular spontaneous tidal ventilation, EIT could detect the start of inspiration (Fig 1A). EIT could detect the absence of spontaneous ventilation during apnea (Fig 1B) and may distinguish an opened vs. closed glottis. If the glottis is opened, the ventilator would provide a normal unsynchronized positive pressure support. If the glottis is closed, a sensory stimulation together with a back-up rate would be provided.

EIT also provides useful information on the expiratory lung impedance. The EIT signal could be used in a closed-loop configuration to trigger an increase in positive end expiratory pressure. It would sustain functional residual capacity (FRC) and be a clear clinical benefit for neonates.

We identify the following advantages & challenges:

| Advantages | Challenges |
|---|---|
| - Regional information and therefore more sensitive | - EIT measures cardiac and ventilation related changes |
| - Non-invasive lung measure without physiological delay | - EIT is sensitive to movement artefacts |
| - No time delay e.g. compared to pressure signal | - EIT has lower sampling frequency |
| - Works in NIV & invasive modes | |

## 3 Discussion

We propose that EIT has the potential to improve patient-ventilator synchrony and may be used as a close-loop system to optimize ventilator settings such as PEEP.

## References

[1] Greenough A, Rossor TE, Sundaresan A, Murthy V, Milner AD (2016) "Synchronized mechanical ventilation for respiratory support in newborn infants." Cochrane Database of Systematic Reviews 9:CD000456

[2] Lemyre B, Davis PG, De Paoli AG, Kirpalani H (2014) "Nasal intermittent positive pressure ventilation (NIPPV) versus nasal continuous positive airway pressure (NCPAP) for preterm neonates after extubation." Cochrane Database of Systematic Reviews 9:CD003212

[3] LS Owen, BJ Manley (2016) "Nasal intermittent positive pressure ventilation in preterm infants: Equipment, evidence, and synchronization" Seminars in Fetal & Neonatal Medicine 21:146e153

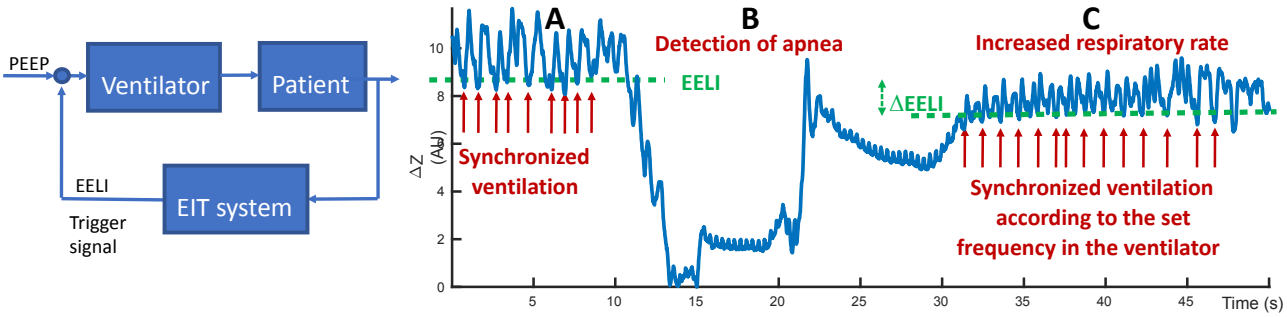


Figure 1: (left) Interaction between ventilator, patient and EIT system, (right) global EIT (arbitrary units) vs. time. A: Patient triggered ventilation, EIT detects the start of inspiration, triggers the ventilation, which then supports the patient, red arrows show the synchronized breath, B: Patient without regular spontaneous breathing, and decreasing end expiratory lung impedance (EELI) decreases, EIT would detect the apnea sequence and support the patient and if needed trigger an alarm, C: the patient starts to breath again and EIT recognize the spontaneous breathing again, EIT triggers the ventilator according to the maximal set breath rate. The EELI drops during the depicted sequence (green part); EIT recognizes the drop of the EELI, send a signal to the ventilator and the ventilator adjusts e.g. PEEP according to the measured EELI. The closed loop system may result in improved support.

# EIT Measurement of Regional Ventilation Distribution in Premature Neonatal Patients with Apnoea

Joseph Omisanya[1], Song Wen[1], Rebecca Yerworth[2] and Richard Bayford[1]
[1]Middlesex University, London, UK, [2]University College London, UK, jo717@live.mdx.ac.uk

**Abstract:** Capability of Electrical impedance tomography (EIT) in measuring changes in end-expiratory lung impedance (ΔEELI) globally and in regions of interest is applied for Apnoea detection in premature neonates.

## 1 Introduction

Electrical impedance tomography (EIT) is a non-invasive technique that utilizes surface voltage measurements obtained from low-intensity alternating current injection to create continuous images of regional ventilation in the lungs [1], [2]. This study aims to develop an automated method to detect apnoea episodes in neonates using EIT measurements. Apnoea is a common respiratory disorder in premature neonates due to their immature lungs [3] therefore, requiring prompt detection and management. Current methods lack direct breathing measurement and accuracy in assessing lung air volume. A more precise and reliable technique is needed to monitor neonatal respiratory function.

## 2 Methods

Data used in this study is obtained from subjects in centre01, being part of an observational clinical study of the larger multicentre observatory continuous regional analysis device for neonate lung (CRADL) project and assessed from cradlproject.org. The raw data were acquired from continuous impedance measurement recorded over 72 hours using the 32 electrodes Swisstom, AG, EIT device at 48 frame per second. The EIT measurement of change in End expiratory lung impedance (ΔEELI), in patients with apnoea, was analysed in the four quadrants of the lung. Fifteen neonates with apnoea episodes (manually confirmed by a physician) were included in the study, ten male and five female neonates with a median gestational age of 31 (range 28-37) weeks. The global EELI among the periods (before, during, and after apnoea) was compared, and the regional distribution of EELI in four regions (LA, RA, LP, RP; where L=left, R=right, A=anterior & P=posterior) was examined. Statistical analysis was performed using Analysis of Variance (ANOVA) in Minitab version 19.0.

A total of 203 apnoea episodes were identified. EELI was highest before apnoea (pre: 25.448 ± 0.846) compared to during (23.28 ± 1.59) and after (22.88 ± 1.99) represented in figure 1. In the anterior region, EELI was lower in both sides of the lung (LA: 4.825, RA: 4.6687) compared to the posterior region (LP: 6.7881, RP: 6.5552) as shown in figure 2. No significant difference in mean impedance was observed before, during, and after apnoea. However, a significant difference in regional impedance distribution was found between anterior and posterior regions during apnoea (p=0.001 at 95% confidence) but not at other times.

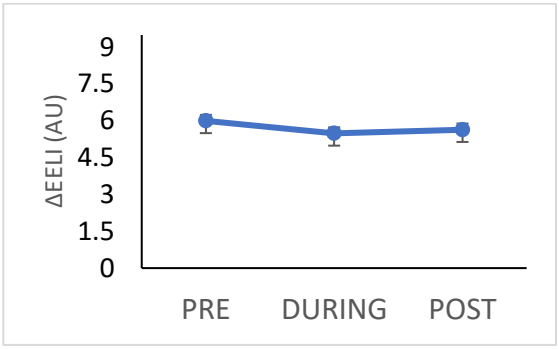


Figure 1. Global ventilation changes before, during and after Apnoea

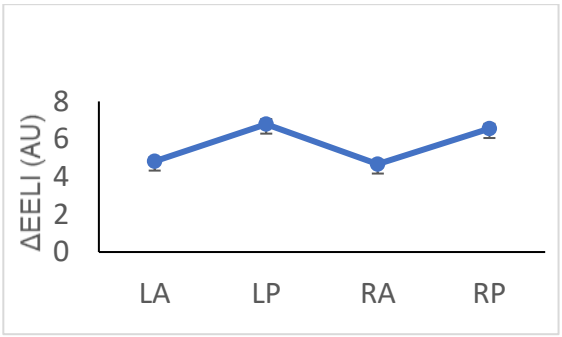


Figure 2. Regional ventilation changes during apnoea

## 3 Conclusion

These findings highlight the potential of EIT as a valuable tool for assessing regional ventilation and detecting apnoea episodes in premature neonates.

## 4 Acknowledgement

The authors would like to express their gratitude to Miedema, M. (Martijn).

## References

[1] S. Leonhardt and B. Lachmann *Intensive Care Medicine*. 38(12):1917-29, 2012
[2] C. Putensen, B. Hentze, S. Muenster, and T. Muders, *Journal of Clinical Medicine*, 8(8), 2019
[3] G. Erickson, N. R. Dobson, and C. E. Hunt, *J Perinatol.* 41(9):2111-2123, 2021

## Session 2: Applications

# Electrical Impedance Mapping For Precision Pedestrian Navigation

Shubhanshu Sharma, Kazi Jabed Akram, Boby George

Department of Electrical Engineering, Indian Institute of Technology Madras, Chennai, India
ee20d413@smail.iitm.ac.in, jakram1612@gmail.com, boby@ee.iitm.ac.in

**Abstract:** An electrical impedance mapping has been used to support the visually impaired person for safe navigation by helping the person to maintain the pedestrian pathway without getting into the asphalt road or the soil. A simulation of the same has been performed to test the feasibility of the proposed technique.

## 1 Introduction

Terrain differentiation is an important feature to support the visually/physically impaired person for their safe navigation. Camera-based technique[1], global positioning system (GPS) based technique [2] etc., are frequently used by researchers in this aspect. But the accuracy of the camera-based technique depends on the ambient light condition and the GPS has a low resolution. In our earlier work, [3] a smart shoe was developed to measure the ground impedance. In this work, an attempt is made to extend our previous method to detect the transitioning of the visually /physically impaired person from one terrain type to another, e.g., from the footpath to the main asphalt road or to the soil.

## 2 Finite Element Based Analysis

Finite Element Analysis (FEA) to differentiate different types of pedestrian pathways was done using COMSOL. The simulation diagram is shown in Fig. 1. In this simulation, a ground structure was formed using three different types of pathways consisting of soil, footpath and road. Two copper electrodes were placed on the ground surface to measure the ground impedance values for various locations on the ground surface. To measure the ground impedance values, one of the copper electrodes was kept at $V_s = 1V$ and the other electrode at ground potential. A boundary probe was used at the grounded electrode to measure the current received by it and the value of ground impedance was calculated.

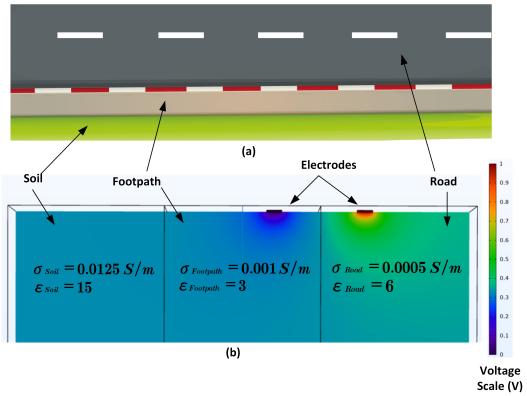


**Figure 1:** (a) Pedestrian pathway with soil, footpath and road. (b) FEA-based simulation study showing the potential gradient in the ground.

For soil, footpath and road pathways the conductivity and permittivity values were kept at $\sigma$ = 0.0125, 0.001, and 0.0005 S/m and $\epsilon$ = 15, 3 and 6 respectively [4]. Frequencies ranging from $50\ Hz\ to\ 20\ kHz$ were taken and the effect observed due to changing frequency was 0.001% of the measured value. Thus the frequency of $f = 10kHz$ was taken considering the effect of low-frequency noise and sensitivity for the simulation study. The equations involved in the FEA simulation were $\nabla.D = \rho_v$, $\nabla \times H = J + \frac{\partial D}{\partial t}$, where $\rho_v$ = Volume Charge Density, D = Electric Flux Density, H = Magnetic Field Intensity and J = Current Density.

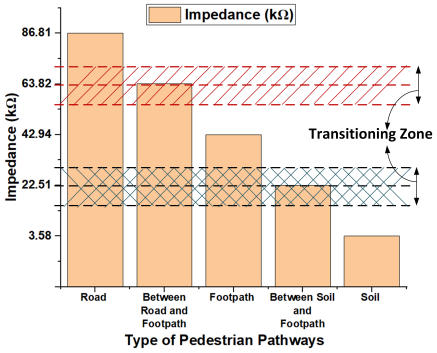


**Figure 2:** Bar plot showing the value of impedance for different pedestrian pathways. Zones detecting the transitioning from one pathway to another are shown in the shaded part of the plot.

### 2.1 Results

The impedance values between the footpath to road or footpath to soil were sufficiently different from the footpath impedance value as shown in Fig. 2. If the impedance value lies in the red or black shaded area as shown in Fig. 2, then it indicates the transitioning from the footpath to the road or from the footpath to the soil respectively. Here, only one set of $\sigma$ and $\epsilon$ values were taken, but in a real scenario, there will be variations in their values. Thus the width of these shaded areas is taken as $\pm 20\%$ of the corresponding impedance values for transitioning.

## 3 Conclusions

In this paper, an FEA-based simulation has been performed to detect the possible transition from one pathway type to another type. It was observed that the difference in the obtained impedance values was sufficient to detect this transition. This technique can be used along with GPS to improve the reliability and precision for the safe navigation of visually impaired persons.

## References

[1] S Tobias, M Lauer, M Schwaab, M Romanovas, S Böhm, and T Jürgensohn *KI-Künstliche Intelligenz*, 30: 29-36, Feb. 2016
[2] R. Velázquez, E. Pissaloux, P. Rodrigo, M. Carrasco, N. I. Giannoccaro, and A. Lay-Ekuakille *Appl. Sci.*, 8(4):578, Apr. 2018
[3] S Sharma and B George *Conf 48th IEEE IECON*, p.1, Brussels, Belgium, Oct 2022
[4] GV Keller and FC Frischknecht *Electrical methods in geophysical prospecting*. 1966

# Peripheral vascular impedance imaging of palmar digital arteries

Gia-Bao Ha[1], Fernando Guevara Vasquez[2], Benjamin Sanchez[1]

[1]Department of Electrical and Computer Engineering, University of Utah, Salt Lake City, USA
[2]Department of Mathematics, University of Utah, Salt Lake City, USA

**Abstract:** Monitoring circulation is critical to guide clinical interventions. Here, we explored peripheral vascular impedance imaging capabilities of finger circulation.

## 1 Introduction

Vascular diseases and disorders of the hand are usually a sign of atherosclerosis and can be serious and have long-lasting health effects. Noninvasive imaging approaches such as ultrasound, micro-CT, or MRI are the benchmark to image hand and finger circulation, however, their use is questionable due to important limitations including cost, portability, and safety concerns associated with the use of ionizing radiation. Here, we perform a study to explore the potential of peripheral vascular impedance (PVI) imaging of finger circulation.

## 2 Methods

Experimental ultrasound imaging of the index finger was performed in B-mode and Doppler flowmetry modes, shown in Figure 1 A and B, respectively, and used to create a two-dimensional finger model shown in Figure 2 A. Finger PVI imaging was simulated with tissues and fluids electrical conductivities at 50 kHz [1, 2]. To complete our forward problem description, we used 16 electrodes and defined an opposite stimulating pattern and adjacent measurement pattern. The forward problem was simulated twice, once with an increased conductivity of 0.08 S/m assigned to the digital arteries to represent change in blood flow. Finger PVI imaging was performed in differential mode, using measurements from both forward simulations.

## 3 Results

Figure 2 B and C show ground truth against finger PVI images. Considering a signal-to-noise ratio of 30 dB, PVI reveals high contrast regions corresponding to conductivity changes of the palmar digital arteries.

## 4 Conclusions

This study aimed to do the groundwork for identification of the experimental parameters required for continuous and wearable visualization of hand and finger circulation using PVI imaging.

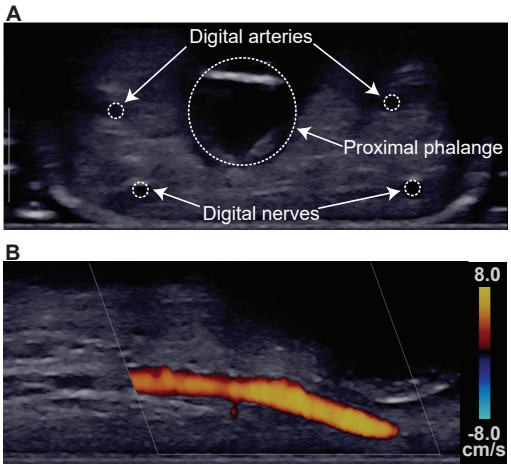


**Figure 1:** Representative ultrasound B-mode (A) and Doppler flowmetry (B) images of the right index finger.

## 5 Conflict of Interest

Dr. Sanchez holds equity in Haystack Dx, Ioniq Sciences, and B-Secur. Dr. Sanchez also serves as Scientific Advisor Board Member to Ioniq and B-Secur. Email: benjamin.sanchez@utah.edu.

## References

[1] A Adler, W R Lionheart *Physiol Meas*, 27:25–42, 2006
[2] P A Hasgall et al. *IT'IS*, doi:10.13099/VIP21000-04-1. Retrieved 01/2023.

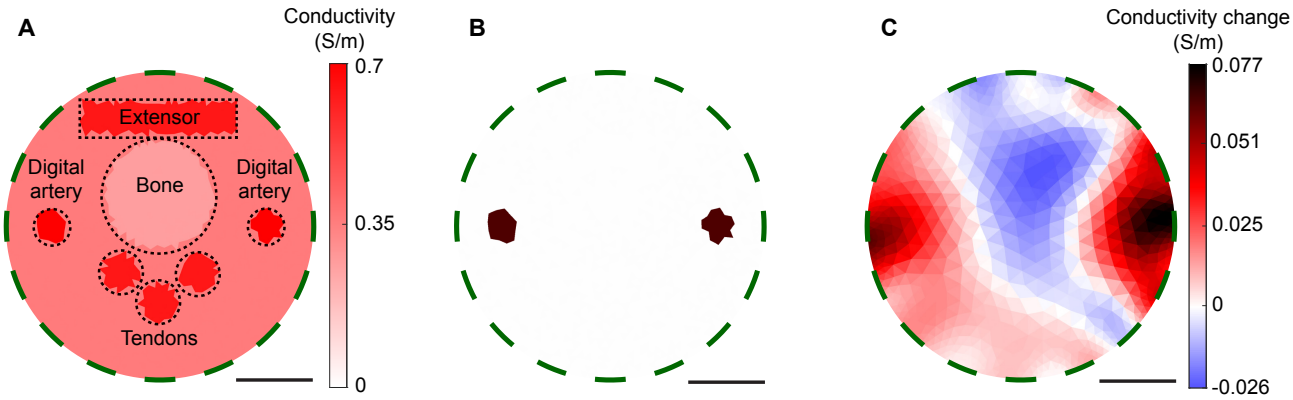


**Figure 2:** (A) Finger model with 16 evenly spaced electrodes on the boundary. The dotted black lines show the intrusions used to define finger internal tissues and fluids. (B) Ground truth and (C) peripheral vascular impedance image considering a signal-to-noise ratio of 30 dB. Scale bar: 5 mm.

# Variational in-silico tissue modelling using two-path impedance spectroscopy and normalizing flows

Benjamin Schindler[1], Dorothee Günzel[2], Thomas Schmid[3,4,1]

[1]Machine Learning Group, Universität Leipzig, Leipzig, Germany, *bschindler@informatik.uni-leipzig.de*
[2]Clinical Physiology/Nutritional Medicine, Charité - Universitätsmedizin Berlin, Berlin, Germany
[3]Martin-Luther-Universität Halle-Wittenberg, Halle (Saale), Germany
[4]Lancaster University in Leipzig, Leipzig, Germany

**Abstract:** We show that the method of Normalizing Flows (NF) has great potential in characterizing biological tissues and generating high-fidelity synthetic data. Along with two-path impedance spectroscopy, NFs are capable of modelling the physiological properties of epithelial tissue, while being accurate, flexible, and outperforming concurrent methods.

## 1 Introduction

While *Machine Learning* (ML) has made remarkable advances in the analysis of tomographic and spectroscopic impedance data, this has always been accompanied by a strong demand for training data. To meet this demand, the synthesis of high-quality labeled data through generative modelling becomes increasingly important. In the following, we present an approach that combines ML-based impedance spectroscopy with training data synthesis, evaluate different variational models, and reveal their potential.

## 2 Methods

### 2.1 Two-path impedance spectroscopy

Two-path impedance spectroscopy determines the physiological properties of healthy and pathogenic epithelia, incorporating their polar nature (with unequal apical and basolateral membrane properties) and the tight junction regulating the paracellular pathway. Corresponding electric circuit model parameters can be derived from spectral impedance measurements using supervised ML and subsequent nonlinear least-squares fitting, as described in [1].

### 2.2 Normalizing Flows

NF is an emerging generative model that maps complex data distributions to simple parametric base distributions, allowing sampling and density estimations [2]. Here, we implement more recent *Neural Spline Flows* (NSF) using the *nflows* python package, with rational quadratic splines as fast, invertible transformations [3]. The NSF consists of five Layers, each incorporating variable mixing through coupling and a spline transformation with five bins. Additionally, each transformation is controlled by a *ResNet* consisting of two Blocks with 32 hidden Neurons.

### 2.3 Evaluation metrics

Trained variational models are evaluated using the *SDmetrics* and *Scikit-learn* packages. *Kolmogorov-Smirnof statistics (KS)* for single parameters (1-dim) and parameter pairs (2-dim), *Pearson Correlation Similarity (CS)*, and *Continuous Kullback-Leibler Divergence (KL)* are recorded. Also, a *Supervised-Learning Performance (SLP)* is derived from the *Mean Average Percentage Error* (MAPE) in predicting all circuit model parameters with *Random Forests* trained on the impedance spectra simulated in this work.

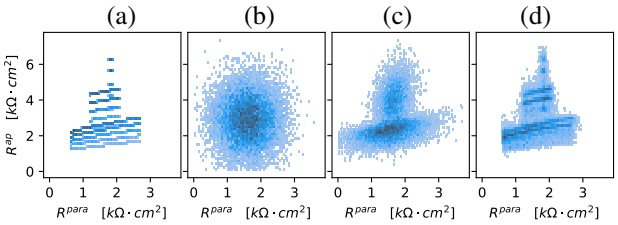


**Figure 1:** Paracellular resistance $R^{para}$ plotted against apical cell membrane resistance $R^{ap}$ for original and modeled data. (a) original data with unwanted blank spaces derived from discretization steps (b) Multivariate Normal Distribution (MVN) (c) Gaussian Mixture Model (GMM) (d) Neuronal Spline Flows (NSF)

## 3 Computational Study

We compare *Neural Spline Flows* (NSF) for variational in-silico modelling of epithelia with two concurrent methods, namely a *Multivariate Normal Distribution* (MND) and a *Gaussian Mixture Model (GMM)* with five components. We used a public data set of impedance spectra modeled after the HT29/B6 cell line [1]. Applying two-path impedance spectroscopy yielded $50,000$ circuit model parameters, whereas $\frac{2}{3}$ have been used for training and $\frac{1}{3}$ for validating according to section 2.3. Table 1 shows evaluation results for the baseline methods and an NSF trained for $40$ epochs with a batch size of $64$.

**Table 1:** Method evaluation including baselines. All metrics were scaled to $[0, 1]$, with 1 being the best possible result.

| method | evaluation metric | | | | |
|---|---|---|---|---|---|
| | *1D-KS* | *2D-KS* | *CS* | *KL* | *SLP* |
| MVN | 0.880 | 0.817 | 0.925 | 0.699 | 0.710 |
| GMM | 0.918 | 0.872 | 0.986 | 0.793 | 0.734 |
| NSF | **0.959** | **0.943** | **0.987** | **0.898** | **0.788** |

## 4 Discussion and Conclusion

Among the generative models tested, NF has by far the best variational modeling accuracy of epithelial physiology and provides the best training data for supervised learning (see Table 1). In this regard, NFs exhibit good data space coverage and high capabilities in modelling cross-relationships of tissue properties (see Figure 1). Since NF design and training are highly adaptable, broader applications in impedance analysis and imaging are promising.

## References

[1] B Schindler, D Günzel, T Schmid *International Journal on Advances in Life Sciences*, 13no.1&2:134–148, 2021
[2] D Rezende, S Mohamed *Conf 32nd ICML*, pp. 1530–1538, Lille, France, Jul 2015
[3] C Durkan,A Bekasov, I Murray, G Papamakarios, *Conf 33rd NeurIPS*, 2019, Vancouver, Canada, December 2019,

# Modelling uterine geometry via electrical impedance tomography

Simon Ghionea[1], Barry Belmont[1], Anjali Sehrawat[1], Michael Barbour[1,2], Zichao Wen[3], Yong Wang[3], and Matthew D Keller[1]

[1]Global Health Labs, Inc, Bellevue, Washington, United States of America, simon.ghionea@ghlabs.org
[2]University of Washington, Seattle, Washington, United States of America (current affiliation)
[3]Washington University School of Medicine in St. Louis, St. Louis, Missouri, United States of America

**Abstract:** The feasibility of using EIT to obtain uterine geometries was demonstrated by comparing EIT-derived surfaces to MRI-derived surfaces for anatomical accuracy.

## 1 Introduction

The intrapartum period of pregnancy remains among the riskiest times for both mothers and their new-borns [1]. Detection and identification of risk factors during labour and delivery can aid in decision making to mitigate adverse outcomes. Electromyometrial imaging (EMMI) is a recently developed approach for assessing risk factors by spatially and temporally monitoring uterine contractions and labour progression [2]. EMMI measures uterine electromyography at the body surface but requires *a priori* knowledge of uterine geometry to yield location-specific activation patterns, currently found by magnetic resonance imaging (MRI), which can be expensive, time consuming, and difficult for some patients. To assess alternatives, we evaluated electrical impedance tomography (EIT) as a non-invasive method for determining uterine geometry.

## 2 Methods

MRI images were obtained for 19 term-pregnant patients. To create virtual volumetric patient-specific phantoms, the MRI images were manually segmented to include the torso and uterus, and each was assigned conductivity values (torso set to a range from 0.05 to 0.5 S/m; uterus set to 1.27 S/m). Simulated electrodes were positioned on the body surface of the virtual phantoms corresponding to their physical locations during clinical EMMI experiments. Two belts of 16 stimulating electrodes each were added superior and inferior to the experimental EMMI electrodes. Since the electrode layouts do not follow conventional symmetric, regularly spaced arrangements, a stimulation and measurement pattern optimized to image the uterus was derived using a patient model.

A forward model for each virtual phantom was created using EIDORS (version 3.10) to generate predicted surface potentials. An inverse model was solved with the surface potentials to calculate an internal conductivity distribution (Gauss-Newton with NOSER prior), which in turn was used to demarcate uterine surface geometries via two methods: (1) contours made with a single conductivity value and (2) contours made along maximal spatial gradients of the reconstructed conductivity distribution. Spherical harmonics were then fit to these surfaces to smooth them.

Geometric accuracy of the final EIT-derived surfaces was measured by comparison to the original MRI segmented uteri via a modified Hausdorff distance (MHD) [3]. Functional accuracy of uterine surfaces generated by EIT for each patient was assessed by comparing outcomes of clinical EMMI using uterine potential maps created from EIT- or MRI-derived uterine geometries for the same torso geometry and surface recordings. Correlation coefficients (CC) were calculated by comparing time series potential at 320 corresponding points on the two uterine surfaces.

## 3 Results and Conclusions

The 38 EIT-derived surfaces are shown in Figure 1(c) comparing functional accuracy to geometric accuracy. One gradient-based surface was excluded from analysis. All other surfaces provided sufficiently high accuracy for the application (MHD < 20 mm and median CC > 0.95), suggesting that EIT may provide an adequate estimation of 3D uterine geometry, and merits further investigation.

## 4 Acknowledgements

Work was supported by grants to PI Wang from the March of Dimes Center (22-FY14-486), NIH/National Institute of Child Health and Human Development (R01HD094381 and R01HD104822), and Bill & Melinda Gates Foundation (INV-005417, INV-035476, and INV-037302).

## References

[1] S Saigal, LW Doyle, *The Lancet*. 371(9608):261-269, 2008.
[2] H Wang, et al. *Nature Communication*, 2023.
[3] M-P Dubuisson and AK Jain, *Proceedings of 12th Int. Conf. on Pattern Recognition*, p. 566-568, 1994.

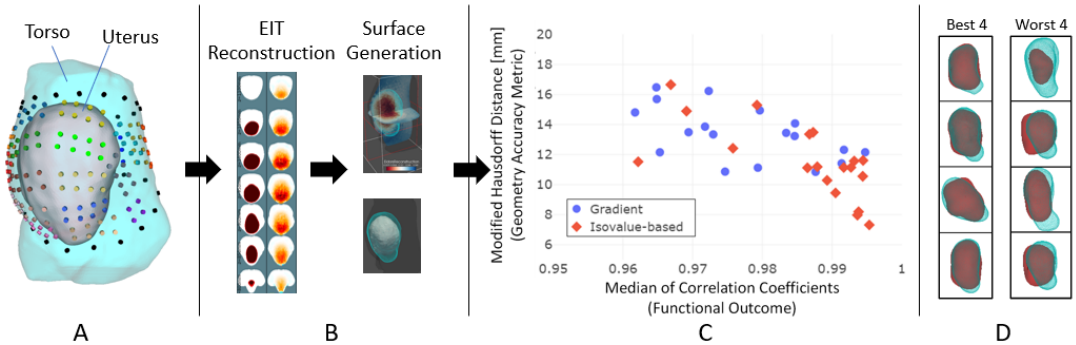


**Figure 1:** Procedure to model EIT performance. (A) Example geometry and electrode layout for one patient. (B) EIT reconstruction and surface extraction. (C) Results from 19 patients (38 surfaces) based on EIT reconstruction (one outlier excluded). Most surfaces have median CC > 0.95 and MHD < 20 mm. (D) Best and worst surfaces (cyan = 'true' MRI surface; red = EIT surface).

# The feasibility to track the inhaled drugs delivery with electrical impedance tomography

Zhe Li[1], Yibo Zhu[1], Zhangjun Tan[1],Yuan Gao[1] and Zhanqi Zhao[2]

[1]Shanghai Jiao Tong University School of Medicine Affiliated Renji Hospital, Shanghai, China. rj_gaoyuan@163.com

[2]Furtwangen University, VS-Schwenningen, Germany.

**Abstract:** In the present study, we explored the feasibility of tracking the inhaled drug delivery with electrical impedance tomography (EIT).

## 1 Introduction

Aerosol inhalation is a well-known method of delivering drugs to the lungs. Delivering drugs via the pulmonary route has several advantages, including increased local concentration of the drug in the lungs, improved lung receptor occupancy, increased absorption due to the large surface area, reduced local and systemic drug delivery, and reduced systemic adverse reactions (1).

The target area for inhalation therapy varies by disease. Asthma patients need drugs delivered to airways, whereas pneumonia patients may benefit from the delivery of drugs to the alveolar region. Hence, not only the total pulmonary drug dose but also the regional distribution or aerosol deposition distribution is a key factor in the clinical success of inhalation therapy. Radionuclide imaging is the primary method of visually evaluating drug deposition in the human airway and plays a role in the development of new inhaled medications and delivery devices (2). However, it has the disadvantage of exposing subjects and operators to health risks due to ionizing radiation (3).

Since hypertonic saline is conductive, it has been used as contrast agent for lung perfusion measurement with EIT (4). We hypothesized that with hypertonic saline, air inhaled drug delivery might be captured with EIT measurement.

## 2 Methods

The prospective observational study was approved by the ethics committee of the Renji Hospital (KY2021-057-B). Informed consent was obtained from all subjects prior to the study. A total of 30 healthy volunteers were included. The EIT (Dräger Medical, Lübeck, Germany) examinations were performed while the subjects breathed quietly in supine position and instructed not to speak or to move during the data acquisition. Data were recorded and the following substances were provided through mask inhaler (EM06-001B, Emedical, Guangdong, China) in a random order (1) water; (2) 5% NaCl; (3) 10% NaCl. Before admitting the substances and between two different substances, inhalation with ambient air were conducted as baseline and washout periods. Each period lasted 5 minutes. In order to reduce the bias in the volunteers' subjective responses, the volunteers were blinded to the inhaled substances.

To evaluate the influence of hypertonic saline, the end-expiratory lung impedance (EELI) was evaluated in two ways: the changes compared to the baseline (ΔEELI), the trend of EELI within one period, which was assessed as regression of the EELI (EELItrend).

## 3 Results

Both ΔEELI and EELItrend showed significant differences among different inhaled substances (Fig. 1). For the absolute differences of EELI, it seemed that 5% NaCl was already sufficient. However, in order to show a decreasing trend during the nebulization, 10% NaCl might be necessary. Only a few subjects reported uncomfortable feelings with hypertonic saline.

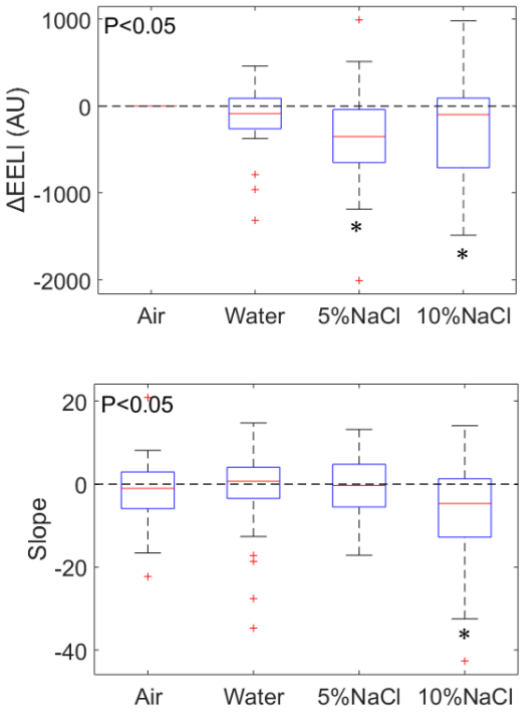


Figure 1. Change of end-expiratory lung impedance (EELI) during nebulization of various substances. AU, arbitrary unit,*$P$<0.05 compared with the Air inhaled period.

## 4 Discussion and Conclusions

We conducted for the first time a proof-of-concept study on healthy volunteers, which showed that hypertonic saline as contrast agent could be captured by EIT. As limitation, this study did not confirm whether the regional distribution of the inhaled substances was corrected located. Besides, the washout period might not be long enough for the lung impedance to return to normal. Individual respiratory efforts might introduce undetectable error. In future studies, subjects under controlled ventilation might be included to further validate the concept.

## References

[1] HM Mansour et al., *Int J Nanomedicine*, 4:299-319,2009
[2] S Newman et al., *Expert Opin Drug Deliv*, 8:841-55,2011.
[3] R Fazel et al., *J Nucl Cardiol*, 18:562-5,2011.
[4] H He et al. Crit Care, 24:586,2

# 3D Gastric Content Visualization (GCV) by Gastric Electrical Impedance Tomography (*g*EIT) with Dual-Step Fuzzy Clustering

P.N. Darma and M.Takei

Graduate School of Science and Engineering, Chiba University, Japan.
panji.nursetia@chiba-u.jp

**Abstract:** Dual-step fuzzy clustering is proposed in gastric visualization to mitigate the noise from gastric-surrounded organs inside the abdomen.The results show that the proposed method has better quality *in-vitro* as compared with conventional EIT and it has a good agreement in *in-vivo* with ultrasound and $^{3}$C Isotope breath test.

## 1 Introduction

Monitoring gastric content volume (GCV) is a critical parameter for functional dyspepsia diseases. Proper daily monitoring of GCV is necessary to improve the patient's quality of life. In the case of gastric visualization, 2D EIT has been proposed with one layer of electrodes on the subject's abdomen during gastric processes. However in 3D EIT is extremely difficult to apply EIT for gastric volume visualization, since the human gastric is located near multiple layers of organs such as the kidney, liver, skin, spinal cord, and spleen which makes blurry 3D EIT images. This paper proposed GCV by Gastric Electrical Impedance Tomography (gEIT) with Dual-Step Fuzzy Clustering to reduce the noise from gastric-surrounded organs inside the abdomen.

## 2 Methods

The objective of the first step of fuzzy clustering is to eliminate noise conductivity from abdomen organs can be summarized using the following equations [1]:

$$ {}^{k}\mathbf{r}_{\mathrm{c}}^{\mathrm{j}} = \frac{\sum_{nk=1}^{nk=Nk} {}^{k}\sigma_n \boldsymbol{r}_n}{\sum_{nk=1}^{nk=Nk} {}^{k}\sigma_n} \quad (1) $$

$$ {}^{k}\mathbf{f}_{\mathrm{c}}^{\mathrm{j}} = \frac{\sum_{n=1}^{n_k} ({}^{k}\mu_n^{j})^2 \, {}^{k}\sigma_n \boldsymbol{r}_n}{\sum_{n=1}^{n_k} ({}^{k}\mu_n^{j})^2} \quad (2) $$

$$ {}^{k}\mu_n^{j} = 1 \Big/ \sum_{l=1}^{l=k} \left( \frac{\left\| \mathbf{r}_{\mathrm{n}} - {}^{k}\mathbf{r}_c^{j} \right\|}{\left\| \mathbf{r}_{\mathrm{n}} - {}^{l}\mathbf{r}_c^{j} \right\|} \right)^2 \quad (3) $$

$$ {}^{k}\boldsymbol{\sigma} = \arg\min \sum_{k=1}^{k=K} \sum_{n=1}^{N} ({}^{k}\mu_n^{j})^2 \left\| \mathbf{r}_n - {}^{k}\mathbf{f}_c^{j} \right\|^2 \quad (4) $$

$$ {}^{k}\mathbf{f}_c^{j+1} - {}^{k}\mathbf{f}_c^{j} = 0 \quad (5) $$

$$ {}^{*}\sigma_n = \begin{cases} 0, \sigma_n \in {}^{3}\boldsymbol{\sigma} \\ \sigma_n, \sigma_n \notin {}^{3}\boldsymbol{\sigma} \end{cases} \quad (6) $$

where ${}^{k}\mathbf{r}_c^{j}$ in eq (1) is *k*-th clustered centroid position at *j*-th iteration number, ${}^{k}\sigma_n$ is *k*-th clustered conductivity distribution at *n*-th elements, $\mathbf{r}_n = [x_{\mathrm{n}}, y_{\mathrm{n}}, z_{\mathrm{n}}]$ is *n*-th mesh element position vector, $n_{\mathrm{k}}$ ($1 \le n_{\mathrm{k}} \le N_{\mathrm{k}}$) is the *n*-th mesh. Fuzzy centroid position of *k*-th cluster ${}^{k}\mathbf{f}_{\mathrm{c}}$ from the *n*-th mesh element ${}^{k}\mathbf{r}_n$ is calculated by (2) and (3). Then, the elements of ${}^{k}\boldsymbol{\sigma}_n$ are relocated into a new clustered conductivity distribution by calculating Euclidean distance between the position of $\mathbf{r}_n$ and ${}^{k}\mathbf{f}_c$ by (4). The final clustered conductivity distribution is achieved while the difference between ${}^{k}\mathbf{r}_n^{j}$ and ${}^{k}\mathbf{r}_n^{j+1}$ equal to 0 as shown in equation (5). Finally, the second dual-step fuzzy clustering is started by extracting only gastric conductivity distribution $^{*}\boldsymbol{\sigma}$ by eliminating the conductivity noise from abdomen organs $^{3}\boldsymbol{\sigma}$ using eq (6).

## 3 Results

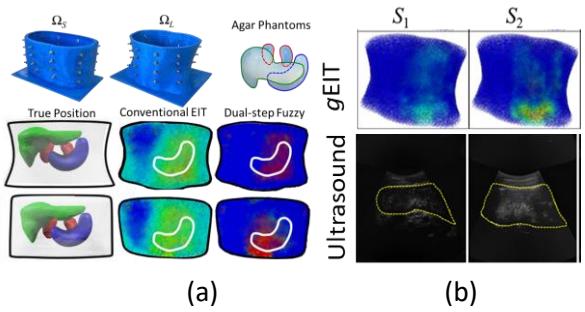


**Figure 1: (a)** Experimental results *in-vitro* using agar phantoms[1]. **(b)** Comparison between *g*EIT and Ultrasound *in-vivo* by drinking 600 mL of a liquid meal[2].

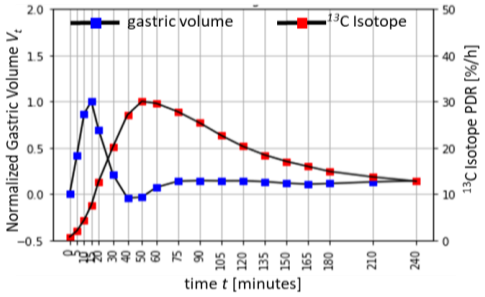


**Figure 2:** Comparison between *g*EIT Volume and $^{13}$C Isotope breath test in 240 Minutes gastric emptying process.

Based on Fig 1(a), the visualization of the gastric volume is qualitatively better based on the proposed dual-step fuzzy compared to the conventional EIT. Furthermore according to Fig 1(b), 3D GCV were successfully reconstructed as compared with ultrasound with Pearson correlation *R*=0.88 [2]. Furthemore based on Fig 2, in 240 minutes gastric emptying test, the gastric volume from gEIT has a good agreement with $^{13}$C Isotope breath test.

## 4 Acknowledgements

This work was supported through JSPS KAKENHI Grant Number: 21F21356.

## References

[1] P. N. Darma, D. Kawashima, and M. Takei, *IEEE Sens. J.*, vol. 22, no. 14, pp. 14336–14346, Jul. 2022,
[2] K. Sakai, P. N. Darma, P. A. Sejati, R. Wicaksono, H. Hayashi, and M. Takei, *Sci. Rep.*, vol. 13, no. 1, p. 514, 2023.

# Assessment of Physiological Oedema on Human Calf by Sparse Bayesian Learning Electrical Impedance Tomography (SBL-EIT)

Ryoma Ogawa[1], Shinsuke Akita[2], and Masahiro Takei[1]

[1]Department of Mechanical Engineering, Graduate School of Science and Engineering, Chiba University, Japan, masa2@chiba-u.jp
[2]Department of Plastic, Reconstructive, and Aesthetic Surgery, Graduate School of Medicine, Chiba University, Japan

**Abstract:** To assess physiological oedema, local spatiotemporal changes in extracellular fluid (ECF) have been extracted by SBL-EIT. The proposed method identifies the subcutaneous adipose tissue (SAT) as the region of interest (ROI) and optimises the sparsity and the slowly-varying correlation structure in the identified SAT.

## 1 Introduction

EIT is a promising diagnostic tool for diseases that cause local spatiotemporal changes of SAT, such as lymphoedema. As a basic physiological phenomenon of the disease, "global" spatiotemporal changes in ECF were assessed by Gauss-Newton-based EIT [1]. Then, "local" spatiotemporal changes were assessed by SBL-EIT using time-variation-constraint to understand physiological oedema better [2]. However, there are still challenges in the biological application of SBL-EIT, i.e., the further correlation verification of SBL-EIT with other modalities is needed. Thus, this study aims to investigate SBL-EIT applied during prolonged standing, morphologically by ultrasound (US) and physiologically by bioelectrical impedance analysis (BIA), respectively.

## 2 Methods

The SBL-EIT has three steps which are Step 1: formulation of blocked column vector (BCV), Step 2: SAT identification based on *a priori* information of each biological tissue, and Step 3: temporal correlation utilization by hyperparameter learning. In Step 1, EIT formula in the manner of multiple measurement vector (MMV) are transformed to the BCV by column-vectorization for utilizing the slowly-varying temporal correlation, i.e., $\Delta\mathbf{Z}^*$, $\Delta\boldsymbol{\sigma}^*$, and $\boldsymbol{\varepsilon}^*$, which represents respectively impedance, conductivity distribution, and noise vector. Note that the prior distribution $p(\Delta\boldsymbol{\sigma}^*; \boldsymbol{\Sigma}^{pre})$ is assumed as a zero-mean multivariate Gaussian distribution in which a prior covariance matrix $\boldsymbol{\Sigma}^{pre}$ consists of a variance vector $\boldsymbol{\gamma} = [\gamma_1,\ldots, \gamma_n,\ldots, \gamma_N]^T$ related to the sparsity, and a positive definite matrix $\mathbf{B}$ related to the temporal correlation

$$p(\Delta\boldsymbol{\sigma}^*;\boldsymbol{\Sigma}^{pre}) \sim N(\mathbf{0},\boldsymbol{\Sigma}^{pre}) \quad (1)$$

where covariance matrix $\boldsymbol{\Sigma}^{pre}=diag(\boldsymbol{\gamma})\otimes\mathbf{B}$. Here $diag(\cdot)$ and $\otimes$ are the symbol of a diagonal matrix and a Kronecker product, respectively. Similar to the $p(\Delta\boldsymbol{\sigma}^*; \boldsymbol{\Sigma}^{pre})$, a multivariate Gaussian distribution is assumed for the noise distribution $p(\boldsymbol{\varepsilon}^*)$, the likelihood $p(\Delta\mathbf{Z}^* \,|\Delta\boldsymbol{\sigma}^*; \boldsymbol{\varepsilon}^*)$ and the posterior distribution $p(\Delta\boldsymbol{\sigma}^*|\Delta\mathbf{Z}^*; \boldsymbol{\Sigma}^{post})$.

### 2.1 Experiments

The SBL-EIT was applied to the assessment of 15 subjects' calves along with an experimental protocol of prolonged standing ($k$ = 1-8: $t_k$ = 5/10/15/20/25/30/35/40 mins) and leg elevation ($k$ = 8-11: $t_k$ = 50/60/70 mins) (Fig. 1(a)). In order to obtain morphological information, US image is acquired by LOGIQ e Premium (GE Healthcare, Japan) with respect to the EIT electrode position and to obtain physiological information, BIA measurement is conducted by InBody S10 (InBody Japan Inc.).

### 2.2 Experimental results

Fig. 1(b) shows $\Delta\boldsymbol{\sigma}^*$ of subject No.1 as a representative, and Fig. 1(c) shows the US image of the subject below the EIT electrode No.(4), which indicate, local spatiotemporal changes are extracted in the identified SAT, not in the muscle compartments or bones, which is qualitatively similar to the US image considering the position of great saphenous vein (GSV). Moreover, the spatial-mean of $\Delta\boldsymbol{\sigma}^*$ in the identified SAT shows a strong positive correlation with conventional impedance $z^{BIA}$ by BIA, which scored correlation coefficient $0.825 < R$ ($n = 15$, $p < 0.05$).

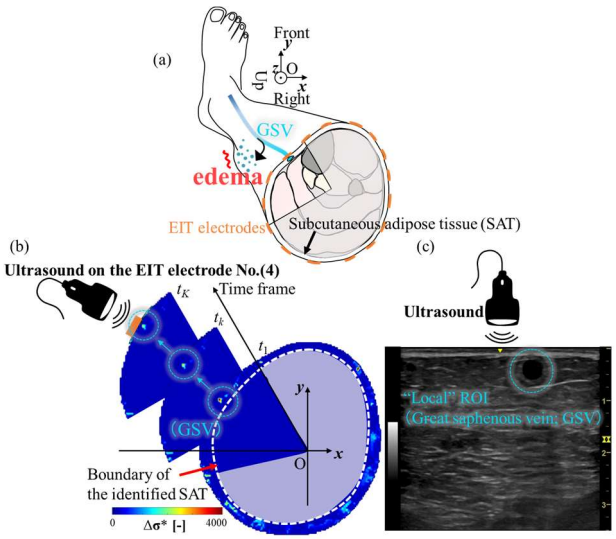


**Figure 1:** (a) Cross-section of a typical human calf during physiological oedema, (b) $\Delta\boldsymbol{\sigma}^*$ of subject No.1 at $t_1$ = 5 mins as a representative, and (c) its US image below EIT electrode No.(4).

## 3 Conclusions

The SBL-EIT applied during prolonged standing was correlated morphologically by US and physiologically by BIA. Further morphological validation by fusion imaging with CT/MRI images is desirable in the future.

## References

[1] R Ogawa, MR Baidillah, S Akita, M Takei, *Journal of Electrical Bioimpedance*, 11(1):19–25,2020
[2] R Ogawa, S Akita, M Takei, *IEEE Trans. Inst. Meas.*,2020, doi: 10.1109/TIM.2022.3220282.

# HDF5-based data format for EIT data

Lucas Possner[1], Martin Bulst[1], Andy Adler[2]

[1]Sciospec Scientific Instruments GmbH, Leipzig, Germany
[2]Carleton University, Ottawa, Canada

**Abstract:** Many devices, both research and commercial, have been made for EIT and bioimpedance applications. We propose a new, flexible data format which can allow data interchange, based on the HDF5 data standard.

## 1 Introduction

EIT and bioimpedance applications are growing. For research applications, there is an increasing complexity of configurations in which complex configurations and multi data streams are used. We have previously proposed an openEIT data format[1], which received little traction because of the difficulties of using XML as a data container. For a new data format, our requirements are:

- Simplicity: writing data in $< 50$ code lines.
- Self-documenting: core data element is the "frame".
- Streaming: suitable for large and online data sets.
- Extensibility: easy to add additional data and elements.

Here, we propose a data format based on HDF5 [4], a hierarchical format designed for numerical data.

## 2 Format

The format (Version 2023.4) is illustrated in Fig 1; updated versions will be documented at [3]. Data sets are stored as frames of data, where each is a sequence of measurements, which are repeated over time. For complex data, `Meas.V.Real` and `Meas.V.Imag` data sets are stored. Multiple data sets can be stored in one file, and each measurement configuration is documented in a `/data/{Data set name}/protocol` field. Electrodes can be numbered or named. In the protocol, the field `Stim.I.01(A)` indicates the excitation current into electrode `01` in Amps; the $4^{\text{th}}$ element shows 10 mA=0.01 A is injected during the $4^{\text{th}}$ measurement in each frame. Excitation (stimulation) information is stored into fields that start with `Stim` and specify the kind of excitation after a dot. Similary, measurement information are stored into fields that start with `Meas`. Measurements normally correspond to stimulations, but this is not required e.g. for biopotential measurements, where `Meas.V.freq(Hz)`=0. Measurement data are stored as a matrix $N_{\text{frames}} \times L_{\text{frame}}$, with an extension indicating the type (`.Abs`, `.Real`, `.Imag`). Times (if known) can be stored as shown. Optional / vendor-specific information (e.g. `/instrument`, or `/data/initialize`) can be stored. Additional recordings with their own protocols are stored with different `/data/{Data set name}`.

## 3 Discussion

We describe an HDF5-based data format for EIT data. It documented with code examples at [3]. The data format is supported in EIDORS [2] and will be part of the next software release.

## References

[1] C Jones *et al*, p.20, Conf EIT 2014
[2] A Adler, WRB Lionheart, Physiol Meas 27:S25–42, 2006
[3] A Adler *et al*, sf.net/p/eidors3d/code/HEAD/tree/trunk/dev/HDF5_tools/ "HDF5 tools", 2023
[4] The HDF Group, 1997–2023, hdfgroup.org/HDF5

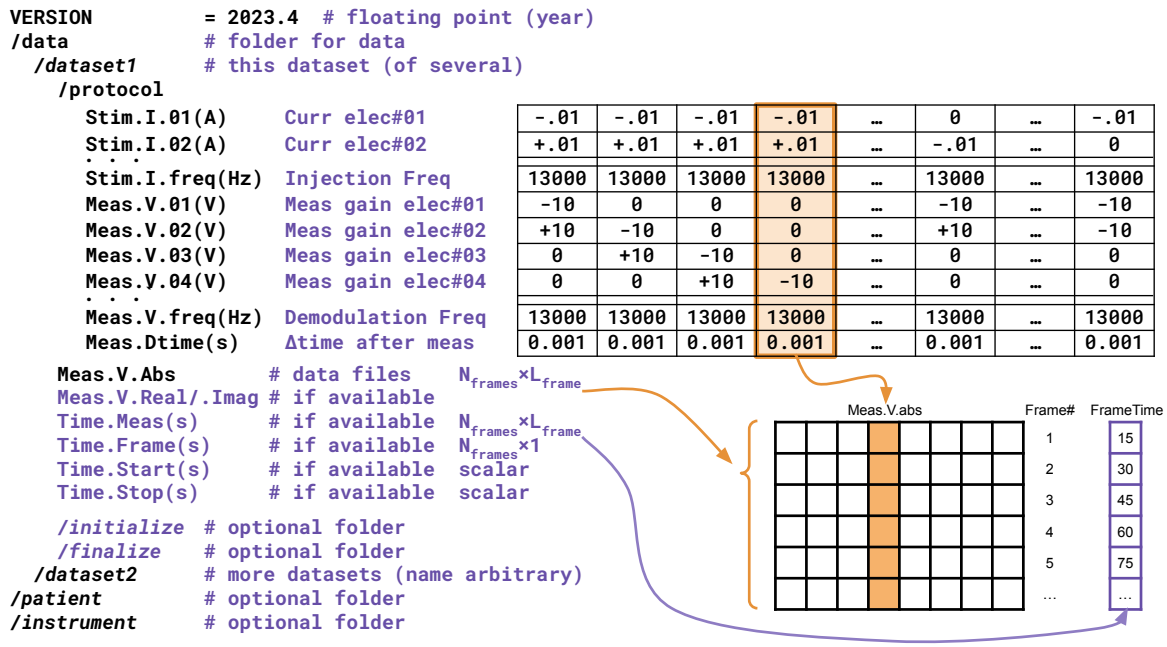


**Figure 1:** Structure of the proposed HDF5 file (Version 2023.4). All data sets must contain a `protocol` defining the configuration for each measurement in a frame. Frame data is a single file (e.g. `Meas.V.abs`). Times for measurements or frames are provided if available. Items in *italics* have example names (can be named differently).

# Rapid Patient-Specific FEM Meshes from 3D iPhone Scans

Ethan Murphy[1], Ryan Halter[1], and Seward Rutkove[2]

[1]Thayer School of Engineering, Dartmouth College, Hanover, NH, USA, ethan.k.murphy@dartmouth.edu

[2]Department of Neurology, Beth Israel Deaconess Medical Center, Boston, MA, USA

**Abstract:** A conventional approach to electrical impedance tomography (EIT) is pulmonary or perfusion imaging using a 32-electrode belt. Numerous studies have found that artefacts are reduced by using accurate modelling of the domain. Here we describe a process that takes 3D scans from an iPhone and rapidly localizes electrodes and produces patient specific meshes in 6.2 minutes on average.

## 1 Introduction

Electrical impedance tomography (EIT) is a novel technology exhibiting promise in numerous clinical applications including cancer, stroke, and haemorrhage detection, but its predominant use has been in pulmonary and perfusion imaging. EIT is safe, low-cost, portable, and capable of providing real-time, long-term monitoring of patients, making it a potentially valuable tool to optimally adjust settings for ventilated patients [1]. Although difference imaging can significantly reduce system noise, improper domain model can yield artifacts [2], which could reduce the utility of the images. Here we use an iPhone to collect a 3D scan of each subject's thorax with an electrode belt and rapidly construct each patient specific mesh.

## 2 Methods

As part of a study investigating EIT for a surrogate measure of pulmonary function tests (PFT) on Amyotrophic Lateral Sclerosis (ALS) patients, we are recording 3D scans of their thorax while wearing a 32-electrode belt. The 3D scans are captured using the FaceID sensor on an iPhone 12 Pro running the Heges application. In principle the software should work with any 3D scan of the thorax. It assumes scans in the form of PLY files consisting of surface triangulation with RGB color information at each node (Fig. 1A). We developed two custom Matlab functions, available on GitHub [3] and [4]. The first quickly 1) loads and crops the surface, and 2) identifies the electrodes via user input. The second, takes the processed 3D scans, constructs a 2D surface triangulation of the outer boundary with encoded electrodes via distmesh (a free meshing software), and then constructs the 3D finite element method (FEM) mesh using gmsh (another free meshing software) (see Fig. 1C). An important part of this process is setting up the belt so that electrodes and their number can be easily determined (Fig. 1B). The software displays six simultaneous scan orientations (Fig. 1D) to give the user a full view of the thorax and belt while identifying electrodes.

## 3 Results

The approach has been evaluated for both quality and speed. The speed analysis utilized the GitHub codes and 3D scans from six subjects. The average total time (loading scan to FEM mesh construction) was 6.2 minutes, where the loading and cropping took 41.0 seconds, the user-involved electrode identification took 141.2 seconds, and the surface and 3D meshing took 148.6 and 42.4 seconds, respectively. Thus, with only 141.2 seconds on average of user interaction, subject-specific patient meshes are constructed. Repeatable tests (comparing electrode locations from three repeated scans) resulted in root mean square differences of 3.8 to 4.2 mm.

## 4 Conclusions

The Matlab functions developed are available on GitHub ([3],[4]), and may be found to be useful for others in the EIT community performing pulmonary or perfusion studies. Further validation analysis on the scan accuracy is ongoing, and comparisons between EIT image generated from generic and patient-specific meshes are planned for our ongoing ALS study.

## References

[1] Leonhardt, S. and Lachman, B., Intensive Care Medicine, vol. 38, no. 12, pp. 1917-1929, 2012.

[2] Murphy, E.K and Mueller, J. IEEE Trans. on Medical Imaging, vol. 28, no. 10, pp. 1576-1584, 2009.

[3] https://github.com/ethankmurphy/EIT_3D_thorax_scans

[4] https://github.com/ethankmurphy/thorax_iphone_to_FEMmesh

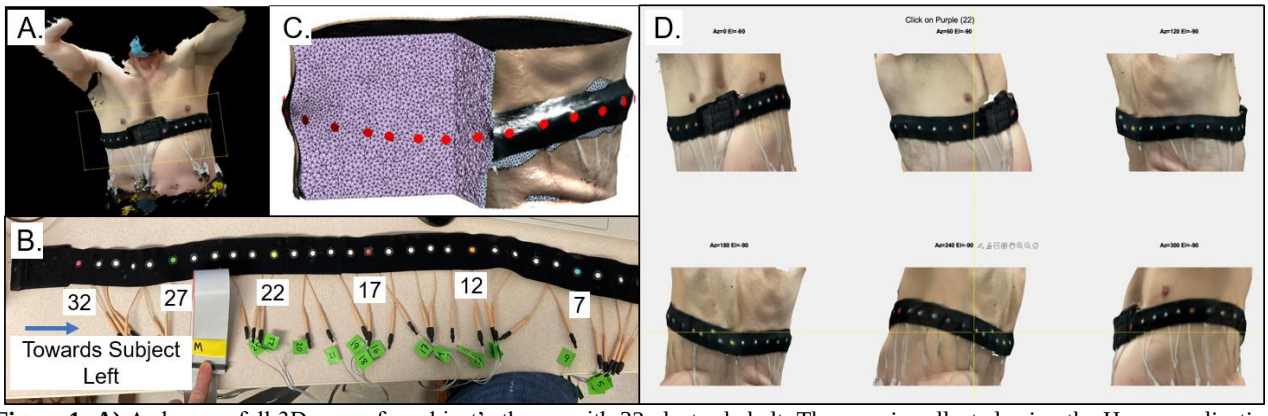


**Figure 1: A)** A shows a full 3D scan of a subject's thorax with 32-electrode belt. The scan is collected using the Heges application with an iPhone. The software is dependent on the electrode belt-design, **B)** i.e. the arrangement of colored stickers. **C)** shows the resulting 3D FEM mesh that is constructed via the scans and processing, and **D)** shows 6 scan views during the electrode segmentation.

# Integrated Ultrasound and EIT for Improved Kidney Stone Detection

Kendall Farnham[1], Ethan Murphy[1], and Ryan Halter[1,2]

[1]Thayer School of Engineering, [2]Geisel School of Medicine, Dartmouth College, Hanover, NH USA,
kendall.farnham@dartmouth.edu

**Abstract:** We are integrating ultrasound and EIT to increase sensitivity to kidney stones with high-contrast, dual-modality imaging. Early detection of kidney stones will be vital for improving treatment outcomes of astronauts on deep space and long-duration missions.

## 1 Introduction

Nephrolithiasis poses a significant threat to astronaut health and wellbeing as a result of dehydration, stasis, and bone demineralization that occur with prolonged microgravity exposure [1]. Detecting kidney stone formation early on is beneficial, as smaller stones (< 5 mm) are easier to pass and non-invasive treatments, such as lithotripsy, depend on localizing the stone with high-contrast imaging (e.g., fluoroscopy, x-ray) first. Ultrasound is the current imaging system used in space, but detecting small stones with ultrasound alone is challenging. Astronauts on deep space missions will need to image and treat medical conditions such as nephrolithiasis without relying on additional large imaging systems or telemedical support, as spacecraft limitations and distance make these solutions unfeasible [2]. Significantly higher contrast can be obtained by imaging the bioelectric properties, as these are sensitive to cellular content, tissue type, and pathology, allowing for stone detection within soft tissue. Electrical impedance tomography (EIT) is a low resource, non-invasive, non-ionizing technology that produces images of these electrical properties and can detect a range of space-related medical conditions (e.g., nephrolithiasis, tissue injury, muscle atrophy, thoracic function, cancer presence) [3]. By combining ultrasound and EIT (US-EIT), we can construct high contrast images without the need for additional equipment or expertise, providing astronauts an easy-to-use tool for effectively monitoring health on long-duration missions.

## 2 Methods

An integrated US-EIT probe was developed using a 16-channel flexible electrode array and C1-6 transducer for dual-modality imaging with the Vivid E95 Flexible Ultrasound System (FUS). To ensure sensitivity to the kidney region, distal electrodes are placed opposite the probe, forcing current to flow through deeper tissues (Fig 1). A phantom imaging setup has been developed for deep tissue sensing: 16 ECG electrodes are fixed on the perimeter of an abdomen-shaped tank to simulate an electrode belt, and gel phantoms simulating abdominal structures are suspended in saline between the probe and distal ECG electrodes (Fig 1). Software developed in MATLAB uses tracking data to register the probe electrode locations to the tank FEM mesh for EIT reconstruction and overlay the 3D EIT image on the registered 2D FUS image plane to provide higher contrast for localizing kidney stones. Preliminary phantom imaging of agar kidney phantoms has been completed to validate the deep tissue sensing setup and determine the region of sensitivity within the domain (Fig 1). Impedance measurements of the saline-filled tank were acquired prior to adding the inclusion and used as the reference dataset for difference EIT reconstruction. Further phantom studies will combine data from multiple probe positions to increase the region of sensitivity using fused-data absolute EIT reconstruction [4], and insulative inclusions of various sizes will be embedded in the gel to simulate kidney stone presence. Analysis will be performed in MATLAB to determine image accuracy and sensitivity to stone inclusions, with the goal to validate US-EIT for non-invasive early kidney stone detection.

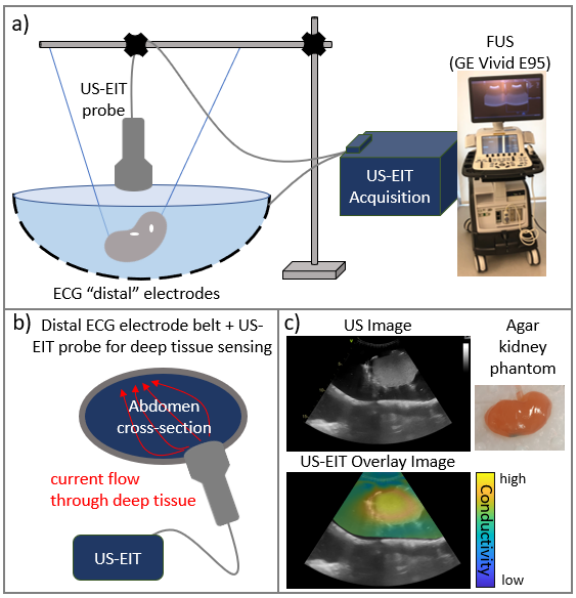


**Figure 1. a)** diagram of kidney stone phantom imaging setup, **b)** diagram of deep tissue sensing showing current flow between US-EIT probe and distal electrodes, **c)** US-EIT reconstruction of an agar kidney phantom (0.6 S/m) in saline (0.2 S/m) where the yellow region localizes the higher conductivity inclusion.

## 3 Conclusions

Integrating EIT with ultrasound will provide a space-compatible medical imaging system that will enable astronauts to detect kidney stones early on for improved treatment outcomes and quality of life on deep space missions.

## 4 Acknowledgements

This work was supported by a NASA Space Technology Graduate Research Fellowship.

## References

[1] Simon J et al, *Journal of Space Safety Engineering*, 3.2, 50-57, 2016
[2] Antonsen, E et al, *NASA HRP Evidence Report*, 16-51, 2017
[3] Paulsen K et al, *Radiation Research*, 152(1), 41-50, 1999
[4] Murphy E et al, *IEEE Trans Med Img*, 39(11):3367-3378, 2020

# Feasibility Study of Monitoring Swallowing with Electrical Impedance Tomography (EIT)

Ardra Venugopal[1], Marcin J. Kraśny[1,2], Ross, Creaven[2], Eoghan Dunne[2], Niall Colgan[1]

[1] Advanced Biological Imaging Lab, Physics, School of Natural Sciences, College of Science and Engineering, University of Galway, Ireland, m.j.krasny@universityofgalway.ie; [2] Translational Medical Device Lab, School of Medicine, College of Medicine, Nursing and Health Sciences, University of Galway, Ireland

**Abstract:** Dysphagia (difficulty swallowing) affects over 50% of stroke survivors, impacting health and quality of life. Dysphagia can often lead to severe consequences such as aspiration pneumonia. This study investigates the feasibility of an EIT-based modality as a diagnostic tool to assess bolus swallowing. The swallowing process was imaged with EIT and then, the resulting conductivity changes were visualised.

## 1 Introduction

More than half of stroke survivors exhibit varying degrees of dysphagia [1]. The current gold standard for diagnosis is the Video Fluoroscopic Swallow Study (VFSS), which uses X-ray radiation and barium contrast agents [2]. However, VFSS is expensive, requires specialised equipment, and exposes patients to radiation. Other alternatives like Fibreoptic Endoscopic Evaluation of swallowing and manometry are invasive and can potentially cause infection as well as affect the swallowing process [3]. In this medical area, the feasibility of non-ionizing and non-invasive techniques like ultrasound and EIT are being studied as alternatives to monitoring swallowing [4, 5]. EIT is a particularly promising technology. The technology is radiation-free, portable, and relatively low-cost, making EIT a potential first-line screening and follow-up diagnostic tool. This study aims to explore the feasibility of using an EIT-based system as a bedside diagnostic tool for assessing swallowing to be an alternative to current modalities.

## 2 Methods

In this study, swallowing was captured in an adult volunteer using the SenTec EIT Pioneer system with a 32-electrode neonatal EIT belt at 100 kHz. The belt was positioned transversely around the neck; above the thyroid cartilage from the front and C3/C4 spine vertebrae at the back. A volume of 25-30 ml of tap water was used as a bolus. A cylindrical finite element mesh (generated with Netgen v5.3.0) was used to create images using EIDORS (v3.10) [6]. Images were reconstructed using the Graz consensus Reconstruction algorithm for EIT (GREIT) difference imaging algorithm [7]. To match previous work by Hughes *et al.,* [5], five EIT frames were averaged to form the baseline reference and the following image snapshots. This processing resulted in an overall interval of 100 ms between the processed images.

## 3 Results

EIT is a functional imaging technique that detects changes in bio-impedance and can display them as colour intensities. Both our study and prior research by Hughes *et al.,* [5] demonstrate significant impedance changes during swallowing that can be visualized with EIT. Fig.1 presents an example sequence of EIT images during a one swallow, with red areas indicating increased conductivity variance and blue areas indicating a decrease in conductivity compared to the baseline recorded prior to the swallow.

## 4 Conclusions

Our findings demonstrate that the EIT system can detect and record swallowing actions, providing adequate data to confirm the occurrence of a swallow. Although real-time imaging may not be available at the moment, the consistency and repetition of the different stages of swallowing are apparent in the reconstructed images. Based on our preliminary analysis, EIT has the potential to complement video-fluoroscopic swallowing studies as a non-invasive, portable, and radiation-free modality.

## 5 Limitations

The project investigated the feasibility of EIT for assessing swallowing. More analysis is needed for a suitable algorithm, including real-time swallow visualisation and quantification. Further investigation is needed on bolus selection, electrode positioning, and larger sample size.

## 6 Acknowledgements

The work presented in this abstract was submitted to the University of Galway, Physics, School of Natural Sciences in 2022 as part of a CAMPEP accredited MSc thesis in Medical Physics. The project was co-financed by the Disruptive Technologies Innovation Fund; Grant agreement: DT20200189.

## References

[1] Hsiao, M.-Y., *et al.*, 2021, DOI: 10.3389/fresc.2021.708102
[2] Chen, Y.-C., *et al.*, 2017, DOI: 10.1016/j.jmu.2017.01.002
[3] Nacci, A., *et al.*, 2022, DOI: 10.1159/000521145
[4] Allen, J. E., *et al.*, 2021, DOI: 10.1097/MOO.0000000000000708
[5] Hughes, T. A. T., *et al.*, 1996, DOI: 10.1088/0967-3334/17/2/00
[6] Adler, A., et al., 2006, DOI: 10.1088/0967-3334/27/5/S03
[7] Adler, A., et al., 2009, DOI: 10.1088/0967-3334/30/6/S03

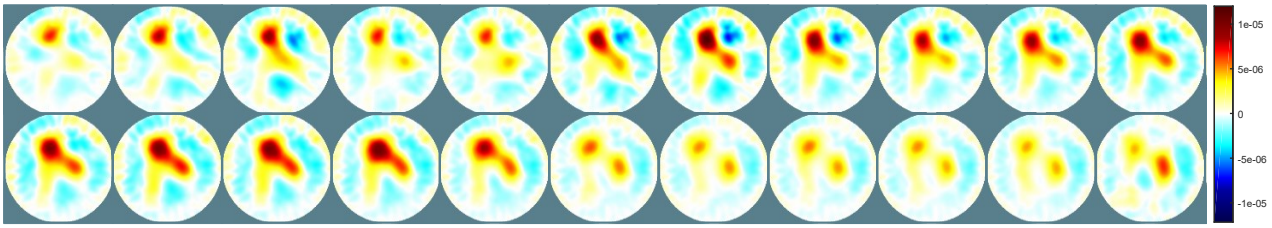


**Figure 1:** EIT imaging capturing frames at 100 ms intervals, highlighting the swallowing action during a single bolus swallow. The images are read from left to right; top row first and then bottom row. Impedance changes are detected as variations in colour intensity during the passage of the bolus. Images are oriented to radiological standards (anterior at the top, right neck on the left, left neck on the right, and posterior at the bottom).

## Session 3: Bioimpedance

# Determining the accuracy of the smart brace measuring knee swelling using bioimpedance analysis (BIA)

Rebecca Gilsing[1], Maartje Hoogeveen[1], Heleen Boers[1] and Walter van der Weegen[2]
[1]Researcher Health Department, Stichting Imec/Holst centre, Eindhoven, Netherlands. Correspondence: maartje.hoogeveen@imec.nl
[2]Sports and Orthopaedics Research Center, Anna hospital, Geldrop, Netherlands

**Abstract:** A previous developed *smart brace* using multi-frequency bioelectrical impedance analysis (BIA) is evaluated for measuring the fluid volume in the knee using a 5mL Lidocaïne + DepoMedrol (1:4) injection. The relative resistance increased (2%) as result of the injection. This indicates that the *smart brace* is a feasible method for objective measurements of knee swelling.

## 1 Introduction

After knee surgery, swelling can negatively influence the patients' perception of recovery. It contributes to decline in range of motion and has been associated with higher pain levels. It is important to improve post-surgical follow up methods to optimize rehabilitation. Current methods to measure swelling, by knee circumference or dynamically sensing the fluid, have shown to be imprecise and subjective [1,2]. Therefore, BIA has been suggested as a method for quantification of swelling. It has been shown that a novel electrode setup with conductive textile integrated into a knee brace, *the smart brace*, is able to distinguish a swollen knee from a not swollen knee [2]. In this research we aim to evaluate the accuracy of BIA in measuring fluid volume in the knee.

## 2 Methods

During osteoarthritis consultations at the Anna hospital in Geldrop, 53 patients were enrolled for this study. The medical ethical committee of the MMC Veldhoven granted exemption for this study (N22.036).
Both the healthy and the 'injected' knee (5mL Lidocaïne + DepoMedrol (1:4) injection) of each patient were measured using the Maltron Bioscan 920-II. All patients were measured with both gel-electrodes, and the brace. The brace as described in Boers 2022 [2] was adjusted to allow it to be worn during the injection and ensure a tight fit of the straps around the leg (figure 1). Prior to measuring with BIA the circumference of both knees was measured at the superior pole of the patella using a standard medical tape measure.

The resistance (R) measured by the Maltron was normalized for the circumference (C) of the corresponding knee using equation (1) [3]. The relative resistance at 5, 50 and 200 kHz is calculated before ($relR_{before}$) and after ($relR_{after}$) the injection using equation (2) [2,4].

**Figure 2**: Left: the smart brace worn by a patient. Right: the inside of the smart brace.

To correct for time-dependent changes, the effect of the injection (relR3) is calculated using equation (3).

$$R = \frac{R_{Maltron}}{C} \quad (1)$$

$$relR_{before/after} = \left(1 - \frac{R_{injected\ before/after}}{R_{healthy\ before/after}}\right) * 100 \quad (2)$$

$$relR3 = relR_{after} - relR_{before} \quad (3)$$

## 3 Results & Discussion

Of the 53 measurements performed, 25 measurements were deemed useful (mean ± SD, age: 64.4 ± 8.1 years, Body Mass Index: 30.1 ± 6.1, $C_{healthy}$: 43.5 ± 5cm, $C_{injected}$: 44 ± 5cm). 28 patients were excluded due to strong outliers, especially at the 5kHz measurements. The reason for this is still under investigation.

An increase of fluid inside the knee joint is expected to decrease the resistance [2]. A 2% decrease in relative resistance at 5 and 50 kHz can be measured by the brace as effect of the 5mL injection (fig. 2, *p<0.01). This indicates that BIA is able to detect a change in knee swelling of 5mL. This difference is detected by the brace and not by the gel electrodes.

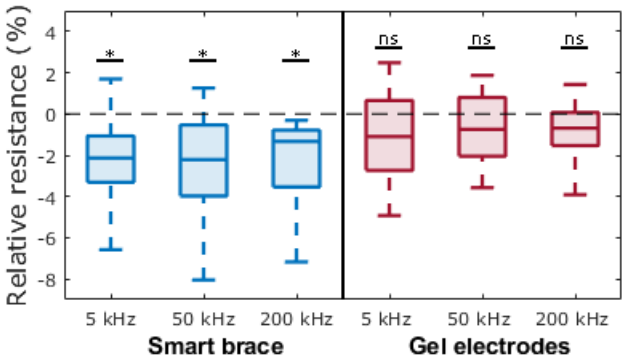


**Figure 1:** Boxplots of the relative resistance at 5-50-200kHz, measured with both the brace and the gel electrodes, *p<0.01.

## 4 Conclusion

This research shows that a wearable BIA device is a feasible method to monitor postoperative knee swelling in an objective manner. Further research and development is needed to better understand the low frequencies outliers and the time dependent properties, as well as creating a device for clinical use.

## References

[1] Pichonazz C, et al., *BMC Musculoskeletal Disorders*, 1:8, 2015
[2] Boers H, et al., *Conf ICEBI & EIT*, Seoul, Korea, Jun 2022
[3] Denneman N, et al., *European Journal of Clinical Nutrition*, 74:1410-1419, 2020
[4] Loyd B, et al.,*Physiotherapy Theory and Practice*, 37:197-203, 2020

# Characterizing novel phantom materials for biomedical applications of electrical impedance tomography

Anjali Sehrawat[1], Barry Belmont[1], Simon Ghionea[1], and Matthew D Keller[1]

[1]Global Health Labs, Inc, Bellevue, Washington, United States of America, anjali.sehrawat@ghlabs.org

**Abstract:** EIT phantom materials with tuned conductivity were developed using several base resins, carbon black, and graphite. Material conductivity was characterized with a tetrapolar probe across a frequency range of 1-200 kHz. Measured conductivities ranged from 5.28 mS/m to 3.29 S/m at 100kHz, matching a range of biological tissues.

## 1 Introduction

Critical to successful biomedical electrical impedance tomography (EIT) implementation is experimental verification using phantom models that reflect real-life cases, both in terms of passive electrical properties (e.g., conductivity) and accurate geometric representation. Unique geometries can be achieved by using solid materials that are mechanically and electrically stable, castable and/or machinable. Various studies have explored developing novel materials [1, 2], where the reported conductivity is limited to the study's EIT requirements.

The objective of this study is to create materials with tuneable conductivity that match various biological tissues, while primarily focusing on amniotic fluid conductivity, reported to be approximately 1.27 S/m for frequencies <1 MHz [3]. This study is part of a larger effort to develop a geometrically accurate pregnant patient torso with a uterine phantom model to assess EIT-based reconstruction of the uterine volume.

## 2 Methods

### 2.1 Material composition

Two-part castable epoxy and polyurethane were selected as base resins for phantom materials—Smooth-On EpoxAcast™ 690 and VytaFlex™ 20, respectively. Various conductivities were achieved by adjusting the percent by weight carbon black (Alfa Aesar, acetylene, 50% compressed, 99.9+%) and graphite (Fischer Chemical), summarized in Table 1. Samples were created by slowly adding carbon black and/or graphite powders into the resin mixture while manually stirring until a homogenous mixture was achieved. For more viscous mixtures, a paint drill mixer was used at a low speed. After the material was cast and cured, two-inch diameter samples were cut, roughly one inch in thickness for measurement.

**Table 1.** Phantom material composition summary.

| Base Resin | Carbon Black (% w/w) | Graphite (% w/w) |
|---|---|---|
| EpoxAcast / VytaFlex 20 | 3 | - |
| EpoxAcast / VytaFlex 20 | 5 | - |
| EpoxAcast | 10 | - |
| EpoxAcast / VytaFlex 20 | 5 | 30 |
| EpoxAcast / VytaFlex 20 | 3 | 40 |

### 2.2 Tetrapolar probe construction

A custom tetrapolar probe was designed and built to characterize material conductivity, shown in Figure 1. The probe consists of four 0.02" diameter platinum wires spaced 5mm apart, housed in a PEEK block. Sample measurements were taken using a LCR meter (Hioki IM3536). Contact between samples and probe was facilitated using a small droplet of ionic solution (1 M KCl, ~11 S/m) at each platinum wire tip. The probe was randomly oriented on the surface of a sample for five individual measurements, each comprising of 10 frequency sweeps (1-200 kHz).

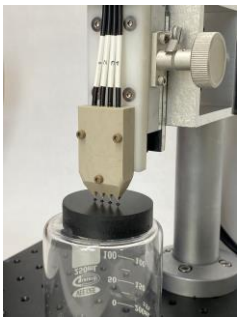

**Figure 1:** Platinum wire tetrapolar probe testing a sample.

## 3 Results and Conclusions

This study demonstrates the development of phantom materials that can be used for various biomedical EIT applications. Figure 2 displays the mean conductivity of each material investigated across the 1-200 kHz range. EpoxAcast with 5% carbon black (1.25 S/m at 100kHz) best matched the target amniotic fluid conductivity. Follow-on work will aim to increase material methods-related homogeneity before using it to cast realistic anatomical models for EIT experimentation.

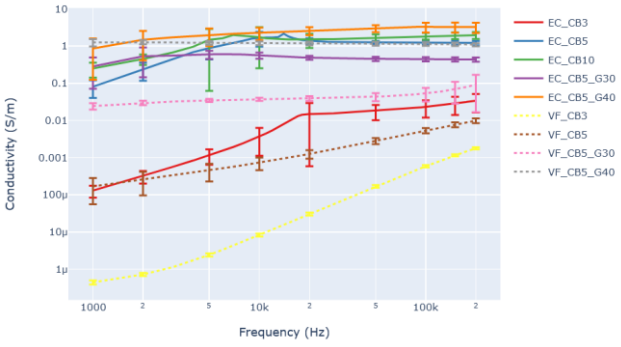


**Figure 2:** Mean material conductivity and standard deviation over 1-200 kHz for EpoxAcast (EC) and VytaFlex (VC) compositions listed in Table 1.

## References

[1] B McDermott, et al. *Biomed. Phys. Eng. Express*, 4:1 015003, 2018
[2] E Dunne, et al. *Physiol Meas*, 39:3 034001, 2018
[3] F De Luca, et al. *Phys. Med. Biol*. 41:1863-1869, 1996

# In-Vivo Characterization of Oral Lesion Using Electrical Impedance

Sophie Lloyd[1], Torri Lee[2], Allaire Doussan[1], Ethan Murphy[1], Joseph Paydarfar[2], Ryan Halter[1,2]

[1]Thayer School of Engineering, Dartmouth College, Hanover, NH, USA. [2]Geisel School of Medicine, Dartmouth College
Correspondence: Sophie Lloyd, e-mail: Sophie.lloyd.TH@dartmouth.edu

**Abstract:** There is a paucity of real-time, quantitative tools available for assessing oral lesions in the clinic. We have developed a hand-held impedance-sensing probe that scans suspicious tissue over a broad spectrum. Preliminary in vivo results suggest that oral tissue impedance can be used to differentiate healthy from cancerous lesions.

## 1 Introduction

No real-time, quantitative devices currently exist for assessing and longitudinally monitoring oral lesions. Instead, clinicians rely on visual inspection and histopathological analysis from biopsy of the lesion site. Identifying premalignant and malignant tissue early is critical for ensuring effective treatment is provided to patients with malignancies. Most oral cancers are diagnosed at later stages, leading to five-year survival rates for oral squamous cell carcinoma patients of only ~50% [1]. Since bioelectrical properties are dependent on tissue architecture and morphology, we hypothesize that sensing and imaging these properties in the context of oral lesions will enable us to accurately characterize different benign, premalignant, and malignant oral lesions in real-time.

## 2 Methods

### 2.1 EIT Hardware

A hand-held probe with a 1 cm diameter circular electrode array was designed for use during oral biopsy and resection procedures. The electrode array is composed of 8 larger electrodes, used for current injection, surrounding a 5x5 square grid of 0.4 mm voltage pickup electrodes. Prior simulations demonstrated the probe's sensitivity to small cancerous inclusions embedded in an adipose tissue background [2]. The probe was interfaced to a Sciospec EIT data acquisition system (Sciospec GmbH, Bennewitz, Germany) to record data at a framerate of 0.5 Hz, with 0.1 mA injection, for 28 different current injection patterns.

### 2.2 Subject Population

A total of 11 patients undergoing biopsy or resection for confirmed or suspected oral cancer lesions were enrolled at Dartmouth Health Medical Center under an Institutional Review Board approved protocol. During resection surgeries, Cohort 1 (n=10), the lesion and benign contralateral side tissue were scanned in-situ; immediately following resection, the lesion and a benign margin were again scanned. In Cohort 2, patients undergoing biopsy (n=1) were probed on the suspicious lesion and healthy contralateral side. Lesion pathology was confirmed following histological assessment for both cohorts. Three repeated impedance spectra were acquired in-vivo and ex-vivo from the lesion center and normal appearing tissue margin, with the probe held to the surface of the tissue. All measurements were calibrated with a saline solution and then averaged to reduce motion artifacts.

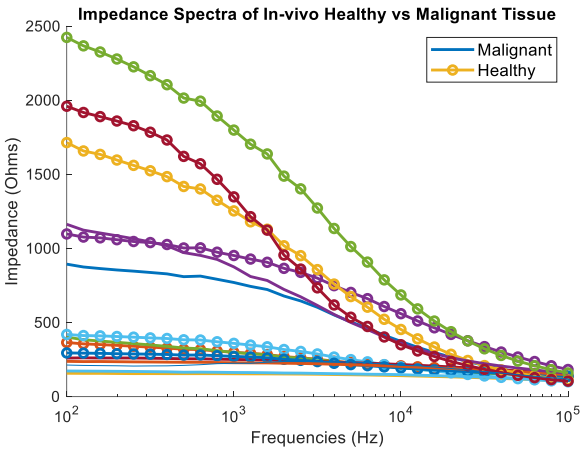


**Figure 1:** Impedance spectrum of in-vivo healthy vs malignant tissues for n = 11 subjects.

## 3 Results

Impedance magnitude differences between malignant lesion and matched healthy control tissues were assessed (Figure 1). Average impedance magnitudes of in-vivo malignant tissues at 500 Hz and 15 kHz were 478±436 and 216±75.7 Ω, respectively, as compared to the average impedances of in-vivo healthy tissue of 1226±945 and 303±137 Ω at respective frequencies. Significant per-frequency impedance difference were identified between malignant lesions and control-matched benign tissue for both in-vivo and ex-vivo tissue at frequencies 100-631 Hz and 15.8 – 80 kHz ($p<0.05$).

## 4 Conclusions

Electrical impedance sensing is a non-invasive, real-time, and non-ionizing modality for differentiating malignant from benign tissue based on their dielectric properties. The hand-held device developed in this study has the potential to be used both in surgery for margin detection and in clinic for lesion characterization pre-biopsy. Preliminary results demonstrate the capabilities of this technique to differentiate malignant from benign tissues in-vivo (Figure 1). This suggests the potential for real-time feedback on margin status in the operating room and for clinicians to reduce the number of unnecessary and painful biopsies. Patient trials are ongoing.

## 5 Acknowledgements

This work was supported by NIH grant 5R21DE031095-02.

## References

[1] Chhabra N, Chhabra. *J Maxillofac Oral Surg*.10.1007/s12663-014-0660-6, 2015

[2] S Kossmann, S Lloyd, R Halter, EIT-based Surgical Margin Probe Development, ICBEM-ICEBI-EIT-2022

# Simple Steps to Characterise a Conductivity Measurement Probe for Bio-impedance Applications

Marcin J. Kraśny[1,2,3], Hamza Benchakroun[1,4], Niko Istuk[1], Declan O'Loughlin[5], Adnan Elahi[1,4], Atif Shahzad[2,6], Martin O'Halloran[1,4] and Eoghan Dunne[1]

[1]Translational Medical Device Lab, University of Galway, Ireland, m.j.krasny@universityofgalway.ie [2]Smart Sensors Lab, University of Galway, [3]Advanced Biological Imaging Lab, University of Galway, [4]Electrical and Electronic Engineering, University of Galway, [5]Electronic and Electrical Engineering, Trinity College Dublin, Ireland, [6]Centre for Systems Modelling and Quantitative Biomedicine, University of Birmingham, UK

**Abstract:** Bio-impedance measurements require properly designed and characterised probes. Particular attention must be paid to the excitation signals and temperature compensation to meet the requirements of the linear sample response and the measurement accuracy. Here, we propose a reliable method to characterise probe performance for conductivity measurements of biological samples.

## 1 Introduction

The design and characterization of a bio-impedance probe requires consideration of several core parameters, i.e., the geometric configuration of the electrodes (size and spacing), operating frequency, excitation signal used for measurements, target conductivity range and finally the determination of probe (cell) constant. Several designs of bio-impedance probes have been proposed, as reported in [1-11]. Each of these probe variants is designed for a specific purpose. However, determination of the cell constant from the probe geometry is not trivial. Thus, determination of the cell constant must be done experimentally. Detailed probe characterisation methods are described in [9, 12, 13] and in our previous works [5-8, 11]. Since little information is given into the correct choice of excitation signal, we focus here on the signal in terms of the specific conductance and the frequency range of interest. We also acknowledge the necessity of temperature compensation to ensure accurate conductivity measurements [14].

## 2 Methods

Results shown in this work were acquired with an LCR-meter (Keysight E4980AL) and a Metrohm PGSTAT204. A miniaturised 4-electrode, colinear probe was used and is described in [5] and the manufacturing is explained in [7].

### 2.1 Ranges of interest of frequency & conductivity

The typical frequency range of applications using Electrical Impedance Tomography is from 0.1 to 250 kHz [15]. However, measurements made with 4-electrode probes above 100 kHz can be affected by parasitic capacitances and inductances [4, 9, 12]. Therefore, in this work, we specify test frequencies to 0.1-100 kHz. The conductivity range of interest is defined by tissue conductivities, which for many soft tissues vary from 1 mS/cm (i.e., heart, kidney) through ~6 mS/cm (blood) to 10 mS/cm (cerebellar fluid) [12, 16, 17]. These conductivities correspond to saline concentrations of 0.01 to 0.1 M [5].

### 2.2 Excitation signal range

Lissajous curve, Kronig-Kramers and wave resolution plots can be used to analyse signals for fulfilling the demand of linear system response [18, 19]. However, they require equipment that allows registration of raw signals (i.e., PGSTAT204). Here, we propose an alternative method that can be used with a standard LCR meter using an excitation signal sweep option. As shown in Fig.1a, saline solutions were measured with set voltage from 1 $mV_{RMS}$ to 350 $mV_{RMS}$. From the current (I) vs voltage (V) plot, one can identify maximum applicable excitation signals within the region of linearity. In this case, the max is 350 $\mu A_{RMS}$ for current and 140 $mV_{RMS}$ for excitation potential modes, respectively, as marked with the orange rectangle in Fig. 1a. Excitation signals beyond this range lead to an exaggerated linear system response.

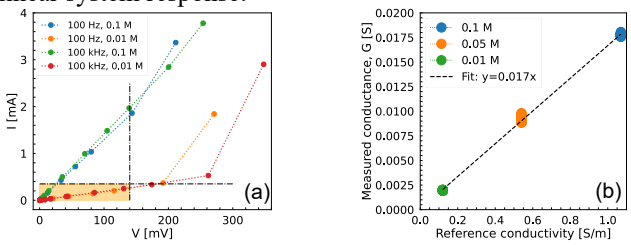


**Figure 1: (a)** Excitation signal determination for the targeted frequency and conductivity ranges. **(b)** Probe constant estimation – linear fit for the conductance vs known reference saline as described in [5], using a 100 $\mu A_{RMS}$ excitation signal (the reference values adjusted to 25°C).

#### 2.2.1 Cell constant determination

For determination of the cell constant, we use measurements of conductance using saline concentrations of known conductivities (values confirmed with a conductivity meter, Hana HI-99301) as described in [5]. Temperature compensation follows the equation from the standard [14] with a temperature coefficient, $\alpha = 2$. The linear fit coefficient is 0.017 m, which results in a probe constant (K) of 58.824 $m^{-1}$ (see Fig.1b).

## 3 Results & Conclusions

Such a calibrated probe was used to determine the conductivity of 0.05 M KCL solution, which resulted in $\sigma_{25} = 6.79 \pm 0.1$ mS/cm over the 0.1-100 kHz range. This measurement is in good agreement with the expected values (6.70 mS/cm) reported in literature [14, 17].

### Acknowledgements

The project was co-financed by the Disruptive Technologies Innovation Fund; Grant agreement: DT20180031A/B & DT20200189.

## References

[1] C. Thirstrup, L. Deleebeeck, DOI: 10.1109/TIM.2021.3083562
[2] M. Mizuhata, DOI: 10.5796/electrochemistry.22-66111
[3] B. Sanchez, J, *et al.*, DOI: 10.1088/0031-9155/59/10/2369
[4] A. Ruiz-Vargas, *et al.*, DOI: 10.1038/s41598-018-33221-4
[5] H. Benchakroun, *et al.*, DOI: 10.1109/JSEN.2022.3218534
[6] H. Benchakroun, *et al.*, DOI: 10.23919/EuCAP51087.2021.9410978
[7] S. Burke, *et al.*, DOI: 10.23919/EuCAP53622.2022.9769600
[8] H. Benchakroun, *et al.*, DOI: 10.3390/s22197171
[9] H. Ma, *et al.*, DOI: 10.1016/j.snb.2015.07.089
[10] A. Dizon, M. E. Orazem, DOI: 10.1016/j.electacta.2020.135732
[11] N. Ištuk, *et al.*, DOI: 10.23919/URSIGASS51995.2021.9560424
[12] C. Gabriel, *et al.*, DOI: 10.1088/0031-9155/54/16/002
[13] Metrohm, Application Note: AN-EC-020
[14] ISO 7888:1985
[15] A. Adler and D. Holder, DOI: 10.1201/9780429399886.
[16] IT'IS Foundation, 'Tissue Properties Database V4.0', DOI: 10.13099/VIP21000-04-0
[17] C. Gabriel, DOI: 10.21236/ADA303903
[18] Metrohm, Application Note: AN-EIS-001
[19] Metrohm, Application Note: AN-EIS-006

## Session 4: Algorithms

# Precision of Data-Driven Methods for Image Reconstruction of Experimental EIT Measurements

Jacob Peter Thönes[1], Lisa Krukewitt[1], Sascha Spors[1]

[1]Institut for Cummunications Engineering, University of Rostock, Rostock, Germany, jacob.thoenes@uni-rostock.de

**Abstract:** Data-driven methods (aka. machine learning, artificial intelligence) for reconstruction of the absolute impedance are recently used more frequently in electrical impedance tomography (EIT). In this contribution we investigate the reconstruction quality of a data-driven method.

## 1 Introduction

The application of deep learning (DL) methods for absolute EIT image reconstruction has increased significantly. The limits and accuracy of different model architectures and reconstruction parameters have not been evaluated extensively so far.

## 2 Method

To reconstruct the conductance distribution $\gamma$ from measured voltage data $\mathbf{V}$, the ill-posed nonlinear inverse EIT reconstruction problem is solved by mapping $\Lambda : \mathbf{V} \to \gamma$ [1]. To this end a deep neural network (DNN) is designed and trained.

### 2.1 Data Acquisition

For a set of experimental measurement data, recorded with the SpectraEIT-Kit [3], a 3D-printed PETG cylinder is placed on different positions inside a phantom tank. The final augmented data set consists of 20 440 voltage samples $\mathbf{V} \in \mathbb{R}^{192}$ and their true conductance distribution $\sigma \in \mathbb{R}^{2807}$. For conductivity representation a FEM mesh is generated using the Python package `pyeit` [2]. The object space is defined with a permittivity of 10 and the empty space with a permittivity of 1. For the training 18 000 samples are used and for the test the remaining 2 440 samples.

### 2.2 Reconstruction Model

The final DL model consists of a mapper and a variational autoencoder (VAE). The VAE is a popular approach for unsupervised learning. It consists of a decoder $\Phi$ and an encoder $\Psi$. Between these components a lower dimensional representation of the input image, called latent space $\mathbf{h} \in \mathbb{R}^8$, is learned. This latent representation contains a compact depiction of the features of the high dimensional input image $\sigma$. During the training, the VAE aims to learn the reconstruction $\gamma$ that approximates the input $\sigma$. The mapper $f_{\text{MAP}}$ interprets the voltage data $\mathbf{V}$ as a nonlinear regression map to the lower dimensional latent representation $\mathbf{h}$ during supervised learning. The reference data is provided by the decoder part of the VAE as $\Phi(\sigma) = \mathbf{h}$. The final model architecture can be described by equation (1).

$$\Lambda := f_{\text{MAP}} \circ \Psi : \mathbf{V} \mapsto \mathbf{h} \mapsto \gamma \tag{1}$$

## 3 Result

In figure 1 three randomly chosen exemplary reconstructions of the test data set are visualized. There is good agreement between the true conductivity distribution and the reconstructed conductivity. This can be seen particularly well in the reconstructed object size, structure, position, and impedance. Figure 2 shows the statistical evaluation of the position error and the deviating mesh elements. A discernible difference is in the noise of detected objects.

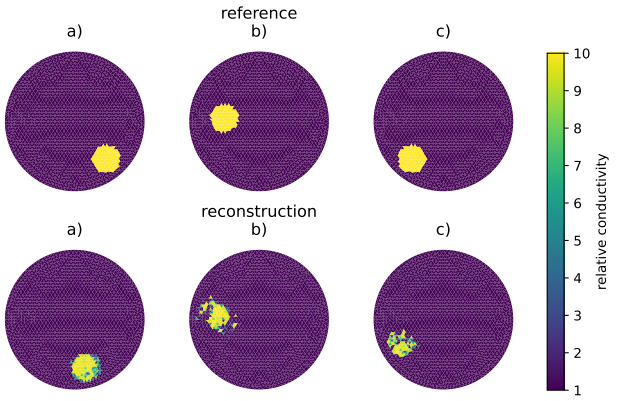


**Figure 1:** Exemplary reconstruction results for unseen samples.

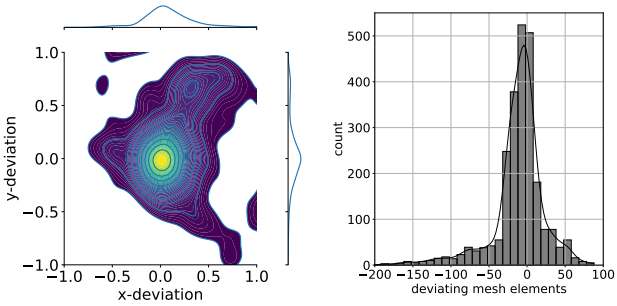


**(a)** Position error **(b)** Surface deviation

**Figure 2:** Deviation plots of the position and surface error between $\sigma$ and $\gamma$ of all test samples using `seaborn`.

## 4 Conclusion

The provided results agrees with the assertion that DL methods appear to overcome limitations of existing numerical model-based methods in impedance reconstruction using EIT.

## 5 Acknowledgements

Funded by the Deutsche Forschungsgemeinschaft (DFG, German Research Foundation) – SFB 1270/2 - 299150580.

## References

[1] Seo, Jin Keun, et al. A learning-based method for solving ill-posed nonlinear inverse problems: a simulation study of lung EIT, *SIAM journal on Imaging Sciences* 12.3 :1275-1295, 2019

[2] B. Liu, B. Yang, C. Xu, J. Xia, M. Dai, Z. Ji, F. You, X. Dong, X. Shi, and F. Fu, "pyeit: A python based framework for electrical impedance tomography," *SoftwareX*, vol. 7, pp. 304-308, 2018

[3] Thoenes, Jacob Peter, et al. Experimental Electrical Impedance Tomography data set using the Spectra Bioimpedance and EIT Complete Kit, 10.5281/zenodo.7192883, 2023

# Neural Networks for Classification of Breast Tissue Using EIT Voltage Data

Emily Corcoran and Sarah Hamilton

Marquette University Department of Mathematical and Statistical Sciences, Milwaukee, WI, USA emily.corcoran@marquette.edu

**Abstract:** This research explores the use of fully connected neural networks to classify breast tumors as malignant or benign from electrical impedance tomography (EIT) voltage data generated from simulated breast phantoms. Initial findings suggest promising accuracy and generalizability.

## 1 Introduction

Current medical practices in breast imaging have low specificity; mammograms cannot generally detect whether a breast tumor is malignant or benign [1]. Consequently, a high proportion of women with positive mammograms must undergo unnecessary biopsies.

The goal in this study was to take advantage of the fact that cancerous breast tumors often have much higher conductivities than their benign counterparts [2]. Motivated by the success of Candiani and Santacesaria [3] in using neural networks for stroke classification from simulated brain scans, we use a fully connected neural network (FCNN) with one hidden layer to take in EIT voltage data from simulated breast phantoms containing tumors and classify said tumors as malignant or benign.

## 2 Methods

Hemispherical breast phantoms were designed in EIDORS [4] with sixteen 1cm diameter electrodes (Figure 1). All were assigned values mimicking possible contrast of conductivities between breast tissues; phantoms were given background conductivities of 0.1 S/m representing fatty breast tissue, and single spherical inclusions of varying radii were added with fixed conductivities either representing malignant (0.9 S/m) or benign (0.2 S/m) tumors. The radii ranged between 0.25cm (the smallest that can generally be detected via mammography) and 2.00cm in increments of 0.25cm.

EIT voltage data was generated via solving the forward problem on each phantom with Walsh-like current patterns, and relative noise was added to the voltage data. Five thousand training samples were generated (2,500 malignant, 2,500 benign) per tumor radius, and the voltages were grounded and normalized before inputting into the network.

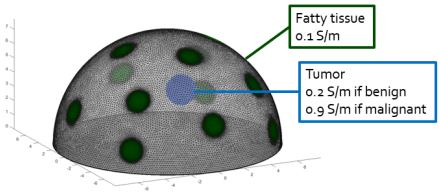


**Figure 1:** Hemispherical breast phantom with sixteen electrodes used to generate the EIT voltage data.

The FCNN was designed with an input layer of 240 nodes (16 electrodes × 15 current patterns), one hidden layer consisting of 7 nodes, and an output layer with one node to classify tumors binarily as malignant or benign (Figure 2). Sigmoid activation functions, Adam optimizers, and cross entropy loss were used in training the network.

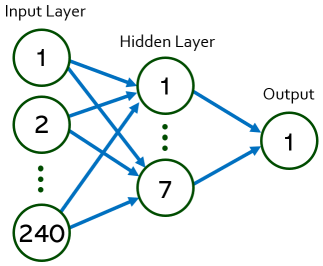


**Figure 2:** Illustration of the FCNN with 240 input nodes, a hidden layer with 7 nodes, and a solitary output node.

As illustrated in Figure 3, when the network was trained on data with 1cm tumors with 0.1% noise and tested on tumors of varying sizes and noise levels, larger tumors were correctly classified a high percentage of the time. Tumors of radii less than 1cm begin to see lower accuracy, especially with increased noise. It should be noted that the ACT EIT systems collect measurement data with much less noise, around 0.01% or 96dB SNR.

The network was also evaluated for generalizability on additional unseen data; it did well in tests including different breast hemisphere sizes, varied electrode locations, and altered domain shapes (hemi-ellipsoids), though struggled in cases with multiple inclusions.

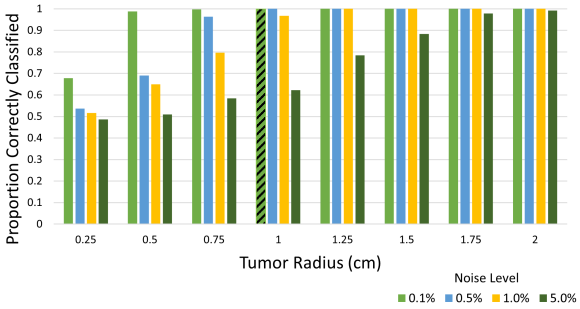


**Figure 3:** Accuracy on test sets of varying tumor radii and noise levels. The diagonal lines indicate the type of training data.

## 3 Conclusions

Though the phantoms simulated for this study were over-simplifications of breast anatomy, the high accuracy achieved in this proof of concept study suggest using FCNNs to classify breast tumors from EIT voltage data is an area ripe for further study. More realistic phantoms should be designed before eventually using data from physical breast scans. Alternative network architectures should also be explored, prioritizing the avoidance of a false negative result.

## 4 Acknowledgements

We would like to thank the National Institutes of Health NIBIB division grant 1R211EB028064.

## References

[1] T Kerner, K Paulsen *IEEE*, 21:638–45, 2002
[2] Y Cheng, M Fu *Thorac Cancer*, 9:459–465, 2018
[3] V Candiani, M Santacesaria *Mathematics in Engineering*, 4:1–22, 2022
[4] A Adler, W Lionheart *Physiological Measurement*, 27:S25–42, 2006

# Chest EIT Based on Lagrange Multipliers Method

Nima Seifnaraghi[1], Andreas Demosthenous[2] and Richard Bayford[1]

[1]Middlesex University, London, UK, [2]University College London, London, UK n.seifnaraghi@mdx.ac.uk

**Abstract:** The resistivity image reconstruction through solving an optimization problem via application of Lagrange multipliers has been adopted to chest EIT. This method generates a smooth image consistent with resistivity changes amid physiological lung activities. The initial results from a human subject have been encouraging.

## 1 Introduction

The application of Lagrange multipliers to improve reconstruction was originally proposed for CT imaging [1] and later adopted to head EIT [2]. The approach was robust, enabling images to be reconstructed when boundary voltage measurements were missing due to the loss of electrode connections. Recently there has been new interest in the use of Lagrange multipliers method for EIT [3]. In this work we explored the possibility of its application in chest EIT on an adult male. Results were verified against the 3D model created from MRI of the same subject. The computational limitations at the time of method proposal in EIT, constrained its application in irregular shapes and required certain relation between the number of projections and measurements, however, with recent advances in computational power, presently, these are not of concern.

## 2 Methods

A system matrix is constructed based on the equipotential paths. These paths map to curvilinear transform. Here, each considered path starts mid-distance of the projection electrode pair and finishing at the sides of each measurement electrode pair as shown in Fig 1(a)..

Hence the measured voltage at the i[th] boundary electrode from the k[th] projection can be written as:

$$g_{ki} = \int_{A(p_{ki})}^{B(p_{ki})} \int_{\mu_{i-\frac{gap}{2}}}^{\mu_{i+\frac{gap}{2}}} \rho(x,y) J_k(x,y) d\mu_{ki} dp_{ki} \quad (1)$$

where $g_{ki}$ denotes the normalised voltage of the i[th] electrode during the k[th] injection, $J_k$ is the current density distribution of the k[th] projection, $\rho(x,y)$ stands for the unknown resistivity distribution whereas $p_{ki}$ and $\mu_{ki}$ represent the curvilinear strip path ki[th] and width of this strip, respectively. This can be introduced as a constraint to an optimization problem using Lagrange multipliers as:

$$g_{ki} = \int_{A(p_{ki})}^{B(p_{ki})} \rho(p_{ki}) J(p_{ki}) dp_{ki} \quad (2)$$

A cost function should be chosen to match the characteristic of the desired solution (the resistivity image) when minimized. One example of such functions is:

$$C(x,y) = \frac{1}{2}\rho(x,y)^2 \quad (3)$$

also known as variational model as minimizing it minimizes the variance. Inserting the constraints into the problem, the functional to be optimized can be written as:

$$\mathbb{C} = \iint C(x,y) dx dy + \sum_{k,i=1}^{N,I} \lambda(p_{ki}) \left( g_{ki} - \int_{A(p_{ki})}^{B(p_{ki})} \rho(p_{ki}) J(p_{ki}) dp_{ki} \right) \quad (4)$$

where $\sum$ is used for brevity to replace double summation over k = 1, 2, ..., N and i = 1, 2, …, I and $\lambda(p_{ki})$ are assumed to be constant over each path $p_{ki}$.

The lambdas in (4) indicate the shares of all other possible projection/measurement paths involved in the present projection path. After few mathematical steps and setting the derivative of the functional $\frac{\partial \mathbb{C}}{\partial \rho}$ to zero, the relation of the solution image and Lagrange multipliers can be found as:

$$\rho(p_{ki}) = \sum_{k',i'=1}^{N,I} \lambda(p_{k'i'}) \; J(p_{k'i'}) \quad (6)$$

Replacing (6), in (1) the linear relation between Lagrange multipliers and boundary voltages can be written as:

$$g_{ki} = \sum_{k',i'=1}^{N,I} \lambda(p_{k'i'}) \left( \int_{A(p_{ki})}^{B(p_{ki})} \int_{\mu_{i-\frac{gap}{2}}}^{\mu_{i+\frac{gap}{2}}} J(p_{k'i'}) J(p_{ki}) d\mu_{ki} dp_{ki} \right) \quad (7)$$

And can be represented in matrix form:

$$\mathbf{g} = \mathbf{B}\boldsymbol{\lambda} \quad (8)$$

where **B** is the system matrix with its elements proportional to the area of intersection of path combinations weighted by their corresponding current densities. Since **B** isn't well-posed an iterative algorithm used in [4] should be applied to yield the Lagrange multipliers. Substituting these, back in (6) the resistivity image can be achieved. The data was collected using 16 electrodes equally spaced on the chest of a 39 yrs male adult. A reconstructed frame using this method is shown in Fig. 1(b) as an example.

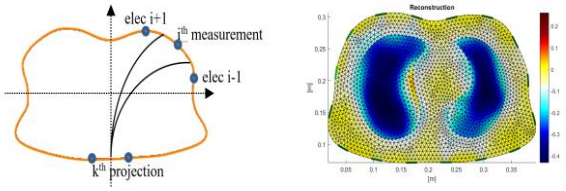


(a) (b)

**Figure 1:** (a) Projection path ki[th], (b) reconstruction example.

## 3 Conclusions

The main virtue of this method in addition to robustness is having few tuning hyper-parameters during inversion with a straightforward relation to the noise level.

## 4 Acknowledgements

This work was funded by EPSRC under grants no. EP/V044036/1 and EP/T001240/1.

## References

[1] T S Durrani, C E Goutis, IEEProc, 127: 161-169, 1980
[2] R Bayford, Y Hanquan, K Boone, D Holder PhysiolMeas, 16:237-247 1995.
[3] Y Shi, Y Wu, M Wang, Z Tian, X Kong, X He, JMedImag, 8: 014501, 2021.
[4] C E Goutis, S N Drossos, IEEPmc, 131: 89-96, 1984

# A novel combination of pre-processing methods for electrical impedance tomography data

J. Wisse-Smit[1, 2], T. Goos[2, 3], A. Jonkman[1], H. Endeman[1], I. Reiss[2], D. Gommers[1]

[1]Department of Adult Intensive Care, Erasmus Medical Centre, the Netherlands, j.j.smit@erasmusmc.nl

[2]Department of Paediatrics, Division of Neonatology, Erasmus Medical Centre – Sophia Children's Hospital, Rotterdam, The Netherlands

[3]Department of Biomechanical Engineering, Faculty of Mechanical, Maritime and Materials Engineering, Delft University of Technology, Delft, The Netherlands

**Abstract:** We present a novel combination of EIT pre-processing methods to detect stable tidal breathing sequences and to separate the respiration signal from the cardiac activity. This algorithm can be used to effectively select stable and artefact-free EIT signals.

## 1 Introduction

The accuracy of electrical impedance tomography (EIT) derived parameters can be compromised by artefacts and noise influences in the EIT signal. Removal of noise and artefacts is challenging due to overlapping and variable frequency spectra. Our aim was to design an EIT pre-processing method for removal of outliers and artefacts and including an automated selection of periods with stable tidal breathing.

## 2 Methods

Data were part of a prospective study in which observational measurements were performed in 25 adult intubated mechanically ventilated patients during a three day period surrounding the weaning including spontaneous breathing trials and after extubation. All signal processing and analyses were programmed in Matlab R2021a (Mathworks, Natick, USA).

1.) Artefacts due the recalibration of the EIT signal (figure 1A) were identified as data points below zero and were removed from the signal.

2.) Filtering of cardiac artefacts was applied using a maximal overlap discrete wavelet transform (MODWT) filter. The purpose of this filter is to remove impedance changes in the global and regional impedance distribution that are not caused by ventilation. By using the wavelet transform the EIT signal was decomposed into details and approximation parts in multiple levels, figure 1B. The upper levels correspond to high frequencies that predominantly consists of noise and cardiac components, whereas the bottom levels are associated with low-frequency components and contain ventilation information. Characteristics for the wavelet transform is its capability to extract localized information. It has a very good trade-off between frequency and time information. As the heart rate is not fixed at a set frequency, the potential to extract localized information makes this MODWT filter encouraging. [1] We reconstructed the EIT signal with information from a subset of the wavelets: we used the symlet (sym4) wavelet with 5 levels of reconstruction. Only level 5 was used for reconstruction of the EIT signal.

3.) For EIT feature extraction it is important that the features are extracted from stable tidal breathing periods, figure 1D. A method proposed by Haris et al. was used for identification and analysis of stable period in EIT recordings. Three criteria were used for identification of stable tidal breathing periods, namely the coefficient of variation of tidal volume, breath duration, and the end-expiratory impedance. [2]

## 3 Conclusion

Visual inspection of our data showed that our proposed combination of pre-processing methods is effective to remove the cardiac activity from the respiratory activity and to select stable tidal breathing EIT signals.

## 4 Acknowledgements

This project was funded by Sentec AG.

## References

[1] P.S. Addison, *Physiol. Meas*. 26 (5), R155, 2005

[2] K. Haris, *Physiol. Meas.* 42 (6), 64003, 2021

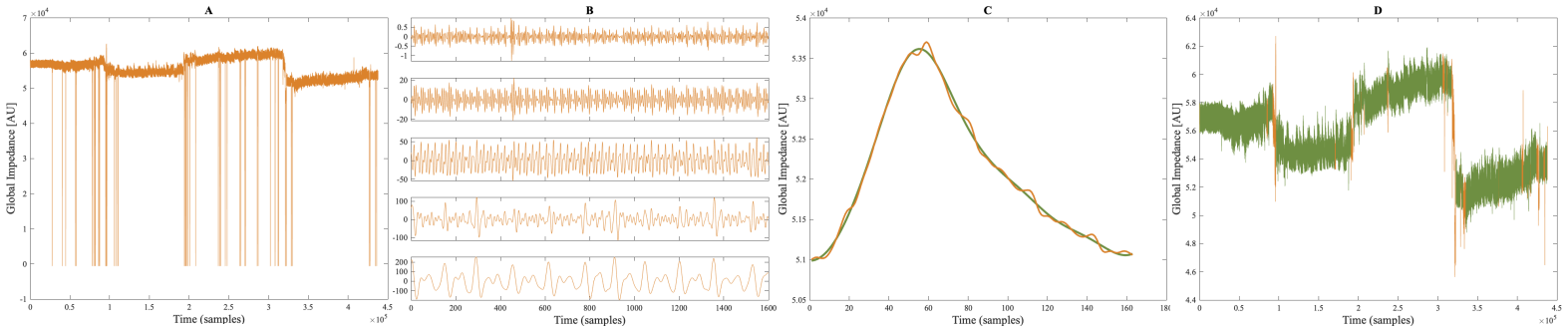


**Figure 1 A.** Raw global impedance signal of a three hour long EIT recording surround the spontaneous breathing trial and extubation from the mechanical ventilator. **B.** Reconstruction levels of the MODWT filter. The first upper levels contains the high frequencies and the bottom level contains the low frequency. **C.** Raw EIT signal (Orange) of one breath containing cardiac noise components. Filtered EIT signal (Green), noise components are removed without loss of ventilation information. **D.** Filtered EIT signal of the full three hour recording were the STBPs are identified and marked green.

# Total Cardiac Vector Reconstruction Using EIT and ECG Data

Christopher Wilcox[1], Nilton Barbosa da Rosa Junior[2], Jennifer Mueller[3], Jonathan Newell[1], Gary Saulnier[4], Omid Rajabi Shishvan[4], David Isaacson[1]

[1]Mathematical Sciences,Rensselaer Polytechnic Institute *wilcoc4@rpi.edu*
[2]School of Biomedical Engineering, Colorado State University, [3]Department of Mathematics, Colorado State University
[4]Electrical and Computer Engineering Department, University at Albany - State University of New York

**Abstract:**

The ACT5 system simultaneously measures EIT and ECG data on all electrodes. This data is used to reconstruct heart current source vectors during a cardiac cycle, yielding an approximate solution to the inverse problem of ECG [3].

## 1 Introduction

During the cardiac cycle, cells in the heart polarize and depolarize causing the chambers to contract/relax and push blood throughout the heart and out to surrounding regions. This electrical activity is described by the heart's current source density vector, $J^H(\vec{x},t)$. This current density gives rise to the ECG voltages measured on the body's surface. We use a single point source of current [3], $J^H(\vec{x},t) = \vec{m}(t)\delta(\vec{x})$ centered at the origin whose strength, $\vec{m}$, approximates the total current source of the heart. That is, $\vec{m} \approx \int_H J^H(\vec{x})\, d\vec{x}$ where $H$ is the heart region for which $J^H$ is defined. Using both the EIT and ECG data taken from the ACT5 system [1], we reconstruct the heart's total current density vectors, $\vec{m}(t)$.

## 2 Methods

The data collection is set up so that a patient has two rows of 16 electrodes all equally spaced and placed slightly above and below the nipple line:

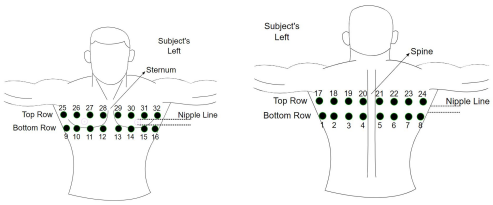


The conductivity is reconstructed using the Todler algorithm, which is a 3-D linearized reconstruction algorithm [2]. Let $\sigma(\vec{x})$ denote the conductivity, and $u(\vec{x})$ denote the voltage inside the body; they satisfy:

$$\nabla \cdot [\sigma(\vec{x})\nabla u(\vec{x})] = \nabla \cdot J^H(\vec{x}) \tag{1}$$

If we make the simplest approximation that in all of $\mathbb{R}^3$, $\sigma(\vec{x}) \approx \sigma_0$, where $\sigma_0$ is the best constant conductivity fit to the EIT data and $J^H = \vec{m}\delta(\vec{x})$, then the above problem has an analytic solution:

$$u(\vec{x}) = \frac{1}{4\pi\sigma_0}\frac{\vec{x}}{||\vec{x}||_2^3} \cdot \vec{m} \tag{2}$$

In general, if we let $G(\sigma)$ denote the forward map that takes $\vec{m}$ to the ECG voltages that would result on the surface electrodes, and let $\vec{V}$ denote the measured ECG voltages on the surface electrodes, then we can solve for the cardiac vector by minimizing the mean square error norm:

$$E(\vec{m}) = ||\vec{V} - G\vec{m}||_2 \tag{3}$$

### 2.1 Results

Shown are results from a healthy adult male using the ACT5 EIT system with a tensor product of discrete trigonometric current patterns applied at 100 kHz with a sampling frequency of 864 Hz. Using both the ECG and EIT data, the total cardiac vectors were reconstructed over six cardiac cycles. We are able to identify cluster regions where the red cluster corresponds to the P-waves, black corresponds to the T-waves and magenta corresponds to the QRS waves.

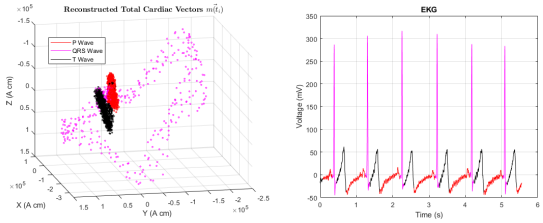


**Figure 1:** Left: The vectors $\vec{m}(t_i)$ where $t_{i+1} = t_i + \Delta t$ for $\Delta t = \frac{1}{864}s$ during 6 cardiac cycles . The red points correspond to atrial depolarization, magenta to ventricular depolarization, and black to ventricular repolarization. Right: The corresponding ECG computed from the voltage difference between electrode 16 and electrode 9

## 3 Conclusions

Using the simultaneous EIT and ECG measurements taken from the ACT5 system, reconstructions of the total cardiac current sources were performed over six cardiac cycles. The reconstructions reveal three distinct regions corresponding to the three main phases of the ECG. Reconstructions were also performed using multiple point sources inside the heart. A discussion of how accurately the voltages measured on the 32 surface electrodes can be reproduced by the reconstructed point sources will be given.

## 4 Acknowledgements

This project was supported by Award Number 5R01EB026710 from the National Institute Of Biomedical Imaging And Bioengineering. The content is solely the responsibility of the authors and does not necessarily represent the official view of the National Institute Of Biomedical Imaging And Bioengineering or the National Institutes of Health.

Human data collection is in accordance with the amended Declaration of Helsinki–Ethical Principles for Medical Research Involving Human Subjects under the approval of the Colorado State University Institutional Review Board (approval number 2943) with informed written consent.

## References

[1] Ahmed Abdelwahab, Omid Rajabi Shishvan, and Gary J. Saulnier. A new method for simultaneous eit/ecg data acquisition. In *21st International Conference on Biomedical Applications of Electrical Impedance (EIT2021)*, 2021.

[2] R.S. Blue, D. Isaacson, and J.C. Newell. Real-time three-dimensional electrical impedance imaging. *Physiological measurement*, 21, 2000.

[3] Jaakko Malmivuo and Robert Plonsey. *Bioelectromagnetism-Principles and Applications of Bioelectric and Biomagnetic Fields*. Oxford University Press, 1995.

# Planar Signal Flow as Metric for EIT Perfusion Analysis

Diogo Silva[1] and Steffen Leonhardt[1]

[1]Chair for Medical Information Technology, RWTH Aachen University, Aachen, Germany, silva@hia.rwth-aachen.de

**Abstract:** Functional imaging in Electrical Impedance Tomography rarely describes structural changes over time. We applied optical flow approaches to pulsatile and bolus signals to estimate vectors of planar movement. These features were represented as standalone HSV images and in complement to functional images of the systole and diastole.

## 1 Introduction

In clinical practice, functional Electrical Impedance Tomography (EIT) images are pixel-wise metrics which summarize the amplitude-related information of the signal over a predefined time window. However, they do not provide information about structural movement over time. In computer vision, a pixel $p$ moving a $\Delta\phi_p = [\Delta x_p, \Delta y_p]^T$ amount in space in consecutive frames may be assumed to maintain its intensity $I(x_p, y_p, t) = I(x_p + \Delta x_p, y_p + \Delta y_p, t + \Delta t)$. This change can be linearized to

$$\frac{\partial_p I}{\partial_p x}\frac{\Delta x_p}{\Delta t} + \frac{\partial_p I}{\partial_p y}\frac{\Delta y_p}{\Delta t} + \frac{\partial_p I}{\partial_p t} = 0. \quad (1)$$

Well-known optical flow techniques can be employed to arrive at the directions and magnitudes of the flow vectors $\Delta\phi$ [2]. This work introduces the methodology to obtain such features from EIT images.

## 2 Materials & Methods

A 30-second cardiac-related signal (CRS) and a 1-minute indicator bolus signal (IBS) were obtained from a mechanically ventilated pig using a Dräger Pulmovista 500 ®, a 16-electrode EIT system with a framerate of 50 Hz, operating with an 80 kHz adjacent-adjacent injection pattern. For the IBS, a 0.9% NaCl solution was administered. The measurements were firstly reconstructed using GREIT [1]. The CRS and IBS videos were then low-pass filtered with cutoff frequencies of 10 and 0.5 Hz, respectively, with the CRS also being high-pass filtered at 0.8 Hz. The CRS pulse train was then segmented into cycles, which were averaged into a single cardiac cycle signal, as Fig. 1 shows.

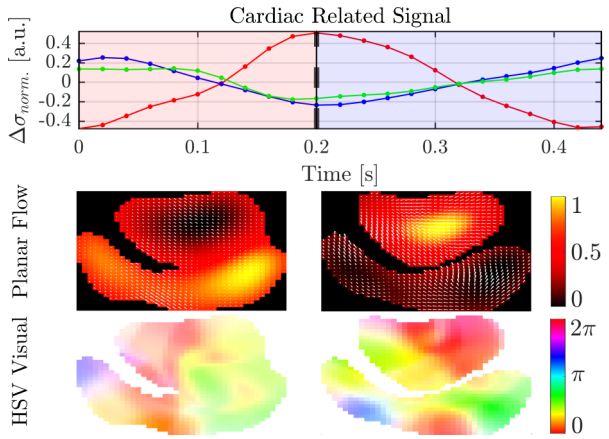


**Figure 1:** Top: heart (red), right (blue) and left lung (green) CRS, red- and blue-shaded systole and diastole; Middle: Planar flow arrows from $\Delta\phi$; Bottom: HSV polar coordinate representation.

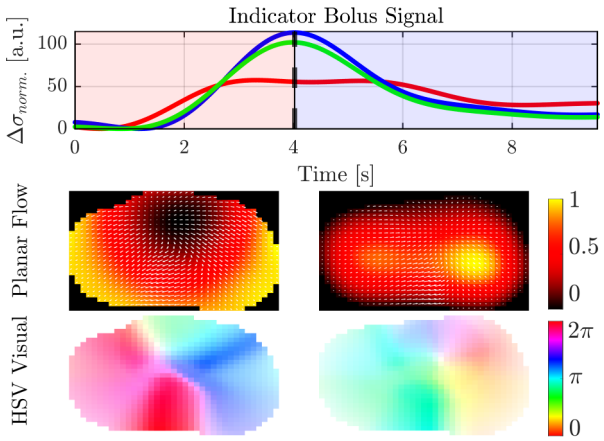


**Figure 2:** Top: heart (red), right (blue) and left lung (green) IBS, red- and blue-shaded systole and diastole; Middle: Planar flow arrows from $\Delta\phi$; Bottom: HSV polar coordinate representation.

The IBS was trimmed at the onset and plateau of the bolus curve, as depicted by Fig. 2. The signals were normalized, and the IBS' baseline was removed. They were then subjected to thresholding using $\frac{1}{3}$ as cutoff. Finally, a multi-resolution version of the basic Lucas-Kanade [2] algorithm was used to estimate $\Delta\phi$ for all $P$ pixels from pairs of consecutive frames: knowing $\Delta t$, and the image gradients $\frac{\partial I}{\partial x}$, $\frac{\partial I}{\partial y}$ and $\frac{\partial I}{\partial t}$ from Eq. 1, is estimated in the least-squares sense as $\Delta\phi = (A^T A)^{-1} A^T b$, where

$$A = \begin{bmatrix} \frac{\partial_1 I}{\partial_1 x} & \frac{\partial_1 I}{\partial_1 y} \\ \vdots & \vdots \\ \frac{\partial_P I}{\partial_P x} & \frac{\partial_P I}{\partial_P y} \end{bmatrix}, b = \begin{bmatrix} -\frac{\partial_1 I}{\partial_1 t}\Delta t \\ \vdots \\ -\frac{\partial_P I}{\partial_P t}\Delta t \end{bmatrix}.$$

The motion vectors $\overline{\Delta\phi}$ are then averaged over the systolic diastolic portions of the CRS and IBS, color-shaded in Figs. 1 and 2, obtaining two flow maps $\overline{\Delta\phi}_{sys}$ and $\overline{\Delta\phi}_{dia}$ per modality cycle.

## 3 Results

The average flow maps $\overline{\Delta\phi}_{sys}$ and $\overline{\Delta\phi}_{dia}$ were superimposed over the first frame of the systolic and diastolic portions of each modality, and their polar magnitudes $\overline{r} = \sqrt{\overline{\Delta x}^2 + \overline{\Delta y}^2}$ and angles $\overline{\theta} = \tan^{-1}\left(\frac{\Delta x}{\Delta y}\right)$ were represented in a single colormap as saturation and hue, respectively, of the HSV color space. Both visualizations are showcased in Figs. 1 and 2.

## 4 Conclusion

The showcased framework allows extracting physiological flow patterns and magnitudes in the CRS and IBS signals, suitable to augment traditional functional imaging, and feed models and algorithms for more sophisticated analyses.

## References

[1] A Adler, John Arnold, R Bayford *Physiol Meas*, 2009
[2] Jean-Yves Bouguet *Intel corporation*, 2001

# Computational Uncertainty Quantification for parametrized Magnetic Resonance Electrical Impedance Tomography

Kenneth Scheel[1,2], Babak Maboudi Afkham[1], Kim Knudsen[1]

[1]Technical University of Denmark, Department of Applied Mathematics and Computer Science, Kgs. Lyngby, Denmark.
[2]University of Eastern Finland, Department of Applied Physics, Kuopio, Finland. kenneth.scheel@uef.fi

**Abstract:** We apply Uncertainty Quantification to characterize the noise in the solution to the inverse problem in Magnetic Resonance Electrical Impedance Tomography. Using Bayesian inversion and MCMC methods we infer the parameters of a known inclusion embedded in a background medium from measurements of its emitted magnetic field.

## 1 MREIT

In MREIT, an MRI machine is used to measure the interior magnetic flux density induced by the injection current from the EIT technique. Having access to interior magnetic field data instead of boundary current-voltage measurements overcomes the severe ill-posedness of EIT [1].

## 2 The forward problem

Let $\Omega$ be an isotropic volume conductor with conductivity $\sigma$. The forward problem is the map from $\sigma$ to the interior magnetic field $\mathbf{B}$. A voltage is applied to the boundary $\partial\Omega$. The electric potential $u$ is governed by the Poisson equation

$$\begin{aligned} -\nabla \cdot \sigma \nabla u &= 0 \quad \text{in } \Omega, \\ u(x,y,z) &= x \quad \text{on } \partial\Omega. \end{aligned}$$

In a practical setup, an alternating 1 mA current with a frequency of 6 Hz may be used as injection current [2]. The current field can be computed via the vector form of Ohm's law $\mathcal{F}(\sigma) = \mathbf{J} = -\sigma\nabla u$. The current field $\mathbf{J}$ induces a magnetic field $\mathbf{B}$ which is given by the Biot-Savart law [3]

$$\mathcal{G}(\mathcal{F}(\sigma)) = \mathbf{B} = \frac{1}{4\pi}\int_\Omega \mathbf{J}(x') \times \frac{x-x'}{|x-x'|^3}\mathrm{d}x'.$$

The MRI machine measures only the $z$-component of $\mathbf{B}$.

## 3 The inverse problem

We seek to estimate $\sigma$ from noisy magnetic field measurements assuming i.i.d. Gaussian noise

$$B_z = \mathcal{G}(\mathcal{F}(\sigma)) + E, \quad E \sim N(0, \epsilon^2 I).$$

We use an $8 \times 8 \times 8$ grid and use FEniCS for the forward computations [4]. We add 10% relative noise to the discrete magnetic field data. We define $\sigma$ as an ellipsoidal inclusion rotated of constant conductivity in the $xy$-plane, embedded in a 1 cm$^3$ cube with a constant conductivity of 1 S/cm. The inclusion is defined by the following eight parameters

| | |
|---|---|
| Semi-axes $(r_x, r_y, r_z)$ | $(0.15, 0.3, 0.2)$ cm |
| Center coordinates $(c_x, c_y, c_z)$ | $(0.43, 0.48, 0.41)$ cm |
| Conductivity of inclusion $\kappa$ | 2 S/cm |
| Rotation angle $\delta$ | $45° \approx 0.785$ rad |

We pose the inverse problem as one of Bayesian inference. The idea is to infer the parameters given magnetic field data by using the *posterior* probability density via Bayes' rule

$$\pi_{\text{post}}(r,c,\kappa,\delta|B_z) \propto \pi_{\text{like}}(B_z|r,c,\kappa,\delta)\pi_{\text{pr}}(r,c,\kappa,\delta),$$

where $\pi_{\text{like}}$ quantifies the data fidelity and $\pi_{\text{pr}}$ quantifies the prior knowledge. The posterior is the solution to the Bayesian inverse problem. By having a probability density we can reason about the uncertainty. The challenge is to explore the posterior by estimating its moments and statistics.

## 4 Numerical results

We use a Metropolis-within-Gibbs method to sample the posterior [5]. We draw 5000 samples $(r_k, c_k, \kappa_k, \delta_k)$ and discard the first 1000 as burn-in. The CPU time was 35.1 hours and 136 MB of memory was used on a High Performance Computing cluster. The code is publicly available on https://github.com/KennethScheel/MSc_UQ_ in_MREIT.

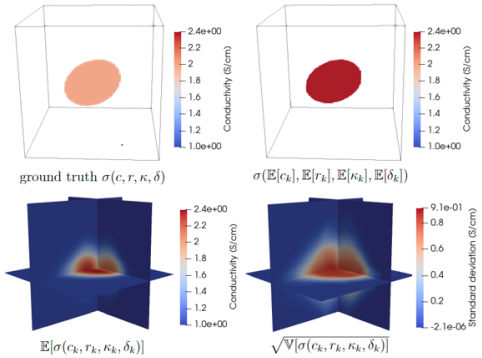


**Figure 1:** Top: Ground truth conductivity and mapped sample means. Bottom: Mean and standard deviation of mapped samples.

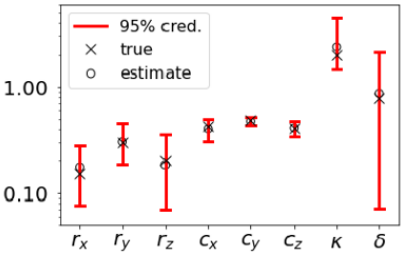


**Figure 2:** Parameter UQ for $\sigma$ with 95% credibility intervals.

## 5 Conclusion

We pose a Bayesian version of the conductivity reconstruction problem in MREIT and solve it using MCMC methods. Our findings indicate that uncertainty is concentrated around the edges of the inclusion. The parameter-wise UQ reveals less uncertainty when estimating the location of an inclusion compared with its shape. A finer meshing of the domain reduces discretization errors and uncertainty but is impractical due to time concerns.

## References

[1] J. K. Seo, E. J. Woo *SIAM Review*, 53(1), 2011.
[2] A. Thielscher et. al. *NeuroImage*, 243, 2021.
[3] H. Yazdanian et. al. *Journal of Comp. Phys.*, 411, 2020.
[4] A. Logg et. al. *Springer*, 2012.
[5] K. Scheel *DTU Compute*, MSc thesis, 2023.

# Low-rank and sparse recovery of lung EIT signals corrupted by motion artifacts using robust PCA

Lin Yang[1], Meng Dai[2], Yifan Liu[2], Feng Fu[2] and Zhanqi Zhao[2]

[1]Department of Aerospace Medicine, The Fourth Military Medical University, Xi'an, China; [2]Department of Biomedical Engineering, The Fourth Military Medical University, Xi'an, China. daimeng@fmmu.edu.cn

**Abstract:** In this study, we attempted to recover lung electrical impedance tomography signals corrupted by motion artifacts using the robust principle component analysis (RPCA) technique. Results showed RPCA was able to restore the faulty EIT data and then give the correct EIT image sequences.

## 1 Introduction

In clinical settings, lung EIT measurements are often interfered with or corrupted by many factors, especially motion facts. This issue is one of the main reasons hindering EIT from being a routine diagnostic tool.

However, as of now, few studies have proposed an effective method to address it. Andy and his colleagues seek to detect erroneous EIT electrodes and compensate for the data measured by those electrodes [1-2]. Nevertheless, for EIT measurements, even if all the electrodes were well connected to the body, the movement from the patient himself, the medical treatments, etc., would also contaminate data.

Therefore, in this study, we, for the first time, attempted to recover the corrupted EIT signal data using the RPCA technique.

## 2 Methods

Theoretically[3], if a matrix is of low rank (many linearly correlated rows) and has a few outlier data, RPCA can decompose the matrix into a low-rank matrix and a sparse matrix. The technique has been widely used in computer vision, radar signal processing, etc.

As for lung EIT, it usually has 192 (or 208) channels of measurement. From Figure 1a, it is noteworthy that each channel has a resemble shape, namely that we can consider it row linearly correlated and then of low rank. Similarly, because the data of motion artifacts rarely happened, it can be considered to be sparse.

Thus, according to the RPCA model, we assume that the measured EIT data $\mathbf{X} \in \mathbb{R}^{m \times n}$ (m is the number of channels, n is the number of data points) could be considered as a sum of a low-rank matrix $\mathbf{L}$ and a sparse matrix $\mathbf{S}$. The problem of finding $\mathbf{L}$ could be formulated as,

$$\min_{\mathbf{L},\mathbf{S}} rank(\mathbf{L}) + \|\mathbf{S}\|_0 \quad s.t. \ \mathbf{L}+\mathbf{S}=\mathbf{X} \tag{1}$$

$\|\bullet\|_0$ is 0-norm. Mathematically, Problem (1) is often transformed into a convex optimization problem as follows,

$$\min_{\mathbf{L},\mathbf{S}} \|\mathbf{L}\|_* + \lambda \|\mathbf{S}\|_1 \quad s.t. \ \mathbf{L}+\mathbf{S}=\mathbf{X} \tag{2}$$

$\|\bullet\|_*$ is nuclear-norm and $\|\bullet\|_1$ is 1-norm. Afterward, we can solve Problem (2) using the Alternating Direction Method of Multipliers (ADMM).

## 3 Results and Conclusions

In the study, we performed lung EIT measurements (20 frames/s)(VenTom-100, Medias Medicals, Suzhou, China) for a male volunteer and One deliberate movement was introduced. Results showed that the original measured EIT data $\mathbf{X}$ was decomposed into the low-rank part $\mathbf{L}$ (Figure 1b) and the sparse part $\mathbf{S}$ (Figure 1c). As for EIT images, Figure 2a demonstrated the obvious motion artifact and it also suppressed other cycles of breathing. Figure 2b showed the EIT images reconstructed using $\mathbf{L}$.

Our preliminary data showed that RPCA effectively recoveredEIT signal corrupted due to motion artifacts.

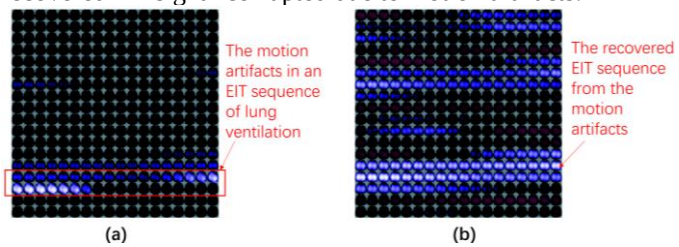


**Figure 2:** EIT image sequences of lung ventilation before (a) and after (b) RPCA.

## 4 Acknowledgments

The work was partially supported by NSFC (52277235).

## References

[1] A Adler, *Physiol Meas*, 25:227–238,2004
[2] AE Hartinger, R Guardo, A Adler, H Gagnon, *IEEE Trans Biomed Eng*, 56:369-377,2009.
[3] SL Brunton *Data-Driven Science and Engineering* Cambridge University Press: London, 2019

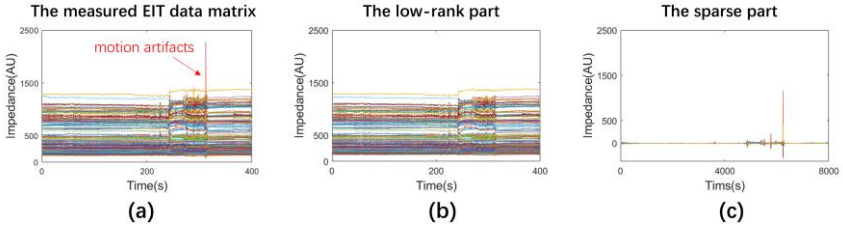


**Figure 1.** RPCA of the measured EIT data matrix. (a) the original data matrix(192×8000).(b) the low-rank matrix of measured EIT data. (c) the sparse matrix of measured EIT data.

# 3D EIT Image Reconstruction Based on Point Cloud Network

Zhou Chen[1], Zhe Liu[1], Yunjie Yang[1]

[1]SMART Group, School of Engineering, The University of Edinburgh, Edinburgh, UK

**Abstract:** Limited work on image reconstruction for Electrical Impedance Tomography (EIT) focuses directly on 3D geometries. This paper proposes an efficient point-cloud-based 3D reconstruction network to tackle the challenging 3D EIT image reconstruction. Results show that this method achieves high-quality 3D representation.

## 1 Introduction

Electrical Impedance Tomography (EIT) is a real-time, non-destructive, label-free imaging modality that visualizes the conductivity distribution within the region of interest [1]. Existing 3D image reconstruction algorithms are based on regular grids (e.g., voxels), which typically results in low image quality and considerable computational cost, and limits their applicability to real-time applications. This paper proposes a learning-based 3D EIT reconstruction algorithm with efficient 3D representations (i.e., point cloud) to achieve higher image accuracy, spatial resolution and computational efficiency.

## 2 Methods

Most existing 3D EIT image reconstruction methods adopt voxel grids for representation. However, voxelization of a 3D space inevitably discards considerable details, and the memory footprint increases cubically with the resolution, indicating that there is always a trade-off between the depth of network architectures and the resolution [2]. In contrast, point clouds are a more efficient format for 3D surfaces. Such representation is simply a collection of unordered points. It thus can naturally handle 3D shapes of arbitrary topologies with fine-grained details. Therefore, we propose to employ limited points (500 points) to represent each 3D object. We adopt a transformer-like [2] point cloud network for image reconstruction (see Fig. 1). This network comprises one encoder and three decoders to simultaneously recover the 3D coordinates of points to adaptively portray the surface of objects and predict the conductivity of each point. The encoder converts EIT measurements into latent code-word and the subsequent decoders respectively take charge of shape reconstruction, object center estimation, and conductivity estimation. The network finally outputs 3D coordinates and conductivity values of the points clouds. To train the network, we generate the 3D EIT dataset by modelling a cylindrical 32-electrode 3D EIT sensor. The 3D EIT dataset has 21,135 samples. This dataset is further partitioned into training set (70%), validation set (15%), and testing set (15%).

## 3 Results and Discussion

We compare the proposed point cloud network with two state-of-the-art image-reconstruction methods for 3D EIT based on the regular volumetric grid of $32\times32\times40$, i.e. 3D-Laplace [1] and the 3D version of FC-UNet [3]. Tab. 1 reports the average Chamfer Distance (CD) [4], Accuracy of classification, Root Mean Square Error (RMSE), and Structural Similarity Index Measure (SSIM) on all the testing data. Two examples of 3D reconstructions are shown in Fig. 2. The Point Cloud Network apparently outperforms the benchmark algorithms with the highest image quality in terms of object number, position, geometry, and conductivity prediction.

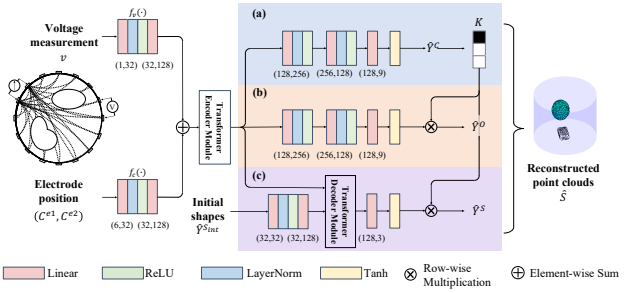


**Figure 1:** The proposed point cloud network for 3D EIT image reconstruction.

**Table 1:** Numerical comparisons averaged over the testing set.

| Metrics | 3D-Laplace[1] | 3D-FC-UNet [3] | Point Cloud Network |
|---|---|---|---|
| CD (m) | - | - | 0.020 |
| Accuracy | - | 80.1% | **98.1%** |
| RMSE | 0.134 | **0.086** | - |
| SSIM | 0.584 | **0.962** | - |

Best results are highlighted in bold.

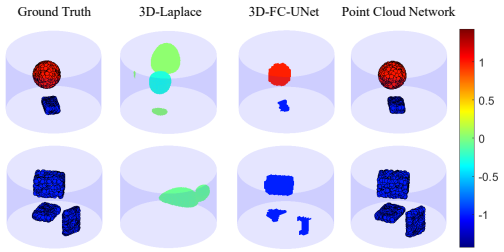


**Figure 2:** 3D reconstruction results. Ground truth and results of the Point Cloud Network are represented by point clouds; the other algorithms are based on the voxel grid.

## 4 Conclusions

We developed a point cloud network for 3D EIT image reconstruction. We demonstrated that point cloud provides more efficient fine-shape descriptions with limited points to alleviate the computational costs. Our point cloud network exhibited superior performance of reconstruction quality over other given 3D image reconstruction methods.

## References

[1] Y Yang et al. *IEEE Sensors J.*, 17(2):514-523, 2017. DOI: 10.1109/JSEN.2016.2631263

[2] L Mescheder et al. *Proc. IEEE CVPR*, 2019. DOI: 10.1109/CVPR.2019.00459

[3] Z Chen et al. *I2MTC 2020*, p.1-6, 2020. DOI: 10.1109/I2MTC43012.2020.9128764

[4] M. A. Butt and P. Maragos *IEEE Trans. Image Process.*, 7(10): 1477-1484, 1998. DOI: 10.1109/83.718487

# High-accuracy impedance tomography enabled by time-of-flight EIT (TOF-EIT): a feasibility study

Florencia Maurino Alperovich, Enrico Ravagli, David Holder, Kirill Aristovich

Department of Medical Physics & Biomedical Engineering, University College London, London, UK,
florencia.alperovich.17@ucl.ac.uk

**Abstract:** The feasibility of using time-of-flight (TOF) to tackle EIT's limitations has been studied in simulation. There was a transient response of $\sim$1.8$\mu$s, enabling an improvement in spatial resolution up to a factor of 30. Appropriate hardware could achieve this with signal-to-noise ratio (SNR) comparable to or larger than that of steady-state EIT.

## 1 Introduction

Imaging stroke and fast neural activity are important potential applications of EIT. In fast neural EIT (fnEIT) in the rat brain using 116 epicortical electrodes, averaging of typically $\sim$7,000 small impedance decreases of $\sim$0.1% over $\sim$30 minutes due to neuronal depolarisation may be imaged accurately[1]. Imaging stroke is challenging as it requires the use of absolute EIT (aEIT), which has been unsuccessful in the past. Both of these modalities are hindered by poor spatial resolution and low SNR[2].

The use of TOF-EIT image construction could confer improved spatial resolution; additional independent measurements arising from different current paths can be obtained by subdividing the transient into multiple time bins.

The aim of this study was to investigate the feasibility of a TOF-EIT system and determine the increase in independent measurements achievable while maintaining the SNR of traditional EIT.

### 1.1 Experimental design

Ideally, TOF would make use of delta functions. However, these are not possible to implement in practice, meaning an alternative with a comparable frequency spectrum, such as a sharp step-function should be evaluated instead. We used a step function with a 250ns rise time, as seen experimentally with a custom-made circuit. The optimum size of the time bins for the system was determined by computing the SNR of different size bins until this matched the steady-state EIT equivalent. Working with a 1 GHz sampling rate, each sample in the bin was averaged together to obtain the SNR value for the complete bin. The stated SNR value was that of the first bin, expected to have the lowest SNR. The noise applied was $0.1\mu V/\sqrt{Hz}$, used to compute the SNR for the expected bandwidth in the fnEIT and aEIT cases.

## 2 Methods

A computational study was carried out within the General Form PDE interface in COMSOL Multiphysics using the wave equation for electric fields in conductive environments (1), as derived from Maxwell's equations.

$$\text{Forward}: \quad \nabla^2 \vec{E} - \mu\sigma\frac{\partial \vec{E}}{\partial t} - \mu\epsilon\frac{\partial^2 \vec{E}}{\partial t^2} = 0 \qquad (1)$$

$$\text{Inverse}: \quad \mathbf{J} = \frac{\delta \mathbf{E}}{\delta \sigma} \qquad (2)$$

$$\widehat{\delta\sigma} = argmin_{\delta\sigma}||\delta\mathbf{E} - \mathbf{J}\delta\sigma||^2 + \alpha||\delta\sigma||^2 \qquad (3)$$

where $\mu$ and $\epsilon$ are the permeability and permittivity, respectively, and $\sigma$ is the conductivity. The geometry modelled was a square saline tank, which mimicked the conductivities of average head tissues ($\sigma$ = 0.3 S/m and $\sigma$ = 3 S/m) with electrodes along one side (Fig. 1a). A 0.75mA step function was injected into the tank and corresponding voltages measured to determine the duration of the transient response. Responses were then divided into varying time-windows to determine the optimum bin size.

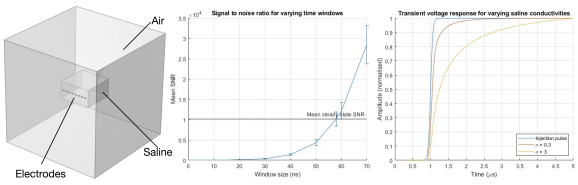


**Figure 1:** a) Modelled geometry. b) SNR values obtained with various time-window sizes. c) Resulting measured voltages for varying saline concentration.

## 3 Results

A transient response with a rise time of $\sim$1.8$\mu$s and $\sim$4$\mu$s was measured with a background conductivity of 0.3S/m and 3S/m, respectively (Fig. 1c).

With a sampling frequency of 1ns, a window size of $\geq$58ns achieved the SNR values for the TOF technique which matched those of steady-state EIT ($>10^4$ for absolute EIT, and $>$10 for fast neural EIT, Fig. 1b). This would enable $>$30 independent measurements per current injection. In a typical 32 electrode EIT system, a total of 15,376 independent TOF measurements would be possible as opposed to just 496 available for standard EIT.

## 4 Conclusions

The framework developed here to study the behaviour of current travelling through tissue showed that TOF-EIT should be feasible with a sampling frequency of 1ns, with 58ns bins enabling a significant improvement in spatial resolution due to the increase in independent measurements. The noise values computed for a single current injection imply SNR could be improved without the need for prolonged acquisition times. This study did not consider the effect of contact impedances on these measurements. Future work includes the validation of the system with proof-of-concept saline tank experiments, and exploring the use of CHIRP current injection to tackle the effects of contact impedance.

## 5 Acknowledgements

This work is supported by the EPSRC-funded UCL Centre for Doctoral Training in Intelligent, Integrated Imaging in Healthcare (i4health) (EP/S021930/1); and EPSRC grant (EP/X018415/1).

## References

[1] K. Aristovich, B.C. Packham, H. Koo, G.S. d. Santos, A. McEvoy, D.S. Holder. *NeuroImage*, 124:204–213, 2016

[2] V. Chitturi, N. Farrukh. *Journal of Electrical Bioimpedance*, 8:66–67, 2017

# Iterative Multi-Layer Perceptron with Smoothing Regularization for Electrical Impedance Tomography Inversion

Zhe Liu[1], Zhou Chen[1] and Yunjie Yang[1]

[1]SMART Group, School of Engineering, The University of Edinburgh, Edinburgh, UK

**Abstract:** We represent the conductivity distribution by a Multi-Layer Perceptron (MLP). We iterate the MLP in the model-based image reconstruction framework for Electrical Impedance Tomography (EIT) inversion. The proposed method is verified by simulation and experiment.

## 1 Introduction

EIT is widely used in various fields, such as industrial processes [1], geoscience [2], and biomedicine [3]. However, the low spatial resolution limits its further development. Advancing image reconstruction algorithms is essential to tackle this problem. Due to the superior capability of nonlinear fitting, Neural networks (NNs) attract considerable attention from the EIT community, and many fine-designed models have been proposed. The main challenges of using NNs are two folds. The first one is the requirement for a large amount of training data. The second one is that the training data quality and diversity limit the performance of the NNs. In other words, machine learning models are usually data-dependent.

This study combines the NNs with the model-based optimization algorithm for Electrical Impedance Tomography (EIT) inversion. We first represent the conductivity distribution by a shallow MLP, which is shown in Fig. 1. Then, we update the MLP's parameters according to the traditional image reconstruction framework. Our method aims to utilize the powerful fitting and regularization ability of the neural networks meanwhile avoiding its data dependency limitation.

## 2 Methods

We denote the unknown conductivity change distribution $\boldsymbol{\sigma} \in \mathbb{R}^N$ by the nonlinear representation:

$$\boldsymbol{\sigma} = \kappa(\boldsymbol{\Theta}; \mathbf{p}), \tag{1}$$

where $\kappa$ represents the shallow MPL in Fig. 1. $\mathbf{p} \in \mathbb{R}^G$ denotes the input of the MLP and $\boldsymbol{\Theta} \in \mathbb{R}^E$ accounts for the neural network parameters. For $\kappa(\boldsymbol{\Theta}; \mathbf{p})$, $\mathbf{p}$ is a random noise vector. The EIT image reconstruction problem can be represented by the below nonlinear optimization problem:

$$\min_{\boldsymbol{\Theta}} \quad \|\mathbf{V} - \mathbf{S}\kappa(\boldsymbol{\Theta}; \mathbf{p})\|_2^2 + \alpha\|\nabla_{TV}(\kappa(\boldsymbol{\Theta}; \mathbf{p}))\|_1 + \beta\|\mathcal{L}(\kappa(\boldsymbol{\Theta}; \mathbf{p}))\|_2^2, \tag{2}$$

where $\mathbf{V} \in \mathbb{R}^M$ denotes the voltage measurements, and $\mathbf{S} \in \mathbb{R}^{M \times N}$ accounts for the sensitivity matrix. $\nabla_{TV}$ stands for the Total Variation (TV) operator, and $\mathcal{L}$ denotes the Laplace operator. $\alpha$ and $\beta$ are parameters for TV and Laplace regularization, respectively.

## 3 Results

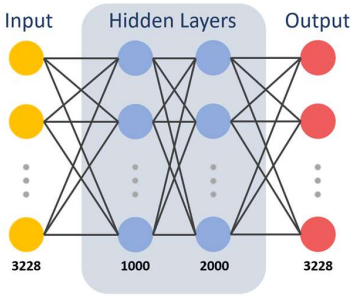


**Figure 1:** Multi-Layer Perceptron (MLP) used in this study. Digits represent the number of neurons in each layer.

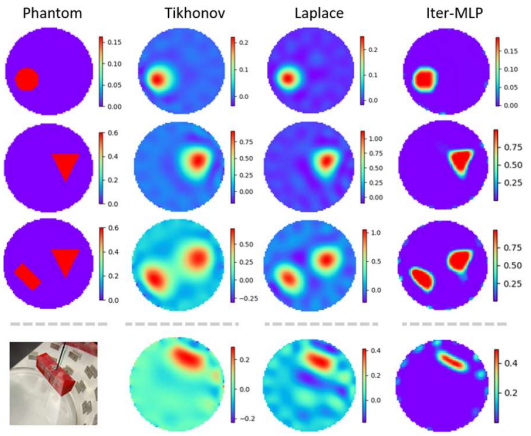


**Figure 2:** Image reconstruction comparison based on simulated and experimental data. Our proposed method is labelled as 'Iter-MLP'.

The proposed method is evaluated by numerical simulation and experiment (see Fig. 2). We compare the performance of the proposed method with Tikhonov regularization and Laplace regularization. Images in the first three rows are results based on simulation data, and those in the last row are results based on experimental data.

## 4 Conclusions

The results show that the proposed method outperforms other given algorithms, especially in background artefact suppression and shape preservation.

## References

[1] C. Dang et al., "Improving EIT-based visualizations of two-phase flows using an eigenvalue correlation method," IEEE Transactions on Instrumentation and Measurement, vol. 70, pp. 1-9, 2021.

[2] S. T. Kidanu et al., "ERT-based investigation of a sinkhole in Greene County, Missouri," AIMS Geosci, vol. 2, no. 2, pp. 99-115, 2016.

[3] Y. Yang et al., "Scaffold-based 3-d cell culture imaging using a miniature electrical impedance tomography sensor," in IEEE Sensors Journal, vol. 19, no. 20, pp. 9071-9080, 2019.

# Introducing an inter-model helps decreasing the degrees of freedom in EIT inverse problem

Rongqing Chen[1,2], Alberto Battistel[1], Sabine Krüger-Ziolek[1], Stefan J. Rupitsch[2], Knut Möller[1]

[1]Institute for Technical Medicine (ITeM), Hochschule Furtwangen, Villingen-Schwenningen, Germany, chr@hs-furtwangen.de

[2]Faculty of Engineering, University of Freiburg, Freiburg, Germany

**Abstract:** EIT reconstruction is characterized with large degrees of freedom. In this contribution, we introduced an 'inter-model', which is the basic function subset derived from Discrete Cosine Transformation (DCT), to cluster the elements of the FEM. This decreases its degrees of freedom. The reconstruction shows more precision and less artefacts.

## 1 Introduction

Electrical Impedance Tomography (EIT) is an imaging modality mainly used to generate two-dimensional cross-sectional images representing impedance change in the thorax. Despite all the benefits, the inverse problem of EIT is ill-posed and characterized with large degrees of freedom. Gong et al. proposed an algorithm to decrease its degrees of freedom. It uses the spectral graph wavelets to downsample the nodes in the Finite Element Model (FEM) used in the reconstruction [1]. However, the downsampling is based on a reconstruction generated from less iterative steps, but this is still characterized with the original degrees of freedom. In this contribution, we introduced a basic function subset derived from Discrete Cosine Transformation (DCT) as an 'inter-model', which modifies the mapping of the Jacobian matrix $\mathbf{J}$. Hence, the degrees of freedom in the inverse problem are decreased. We conducted numerical simulations to generate the voltage data for the reconstruction purpose. Figures of merit are used to compare the EIT images from two different EIT algorithms, which are the Gauss-Newton linear one-step solver (GN approach) and our DCT approach.

## 2 Methods

The estimation of the changes in conductivity $\hat{\mathbf{x}}$ within the thorax from a set of changes in boundary voltages $\mathbf{y}$ is described in EIT as a simplified linearized form:

$$\hat{\mathbf{x}} = (\mathbf{J}^T\mathbf{J} + \lambda^2\mathbf{R})^{-1}\mathbf{J}^T\mathbf{y} = \mathbf{B}\mathbf{y}\,. \qquad (1)$$

An 'inter-model' $\mathbf{D}$, which is a subset of basic cosine functions at varying frequencies derived from DCT, is introduced as

$$D(p,q)_{m,n} = \alpha_p\alpha_q \cos\frac{(2m+1)p\pi}{2M}\cos\frac{(2n+1)q\pi}{2N}\,, \qquad (2)$$

where $p$ and $q$ are the frequencies of the cosine functions, which were chosen as 15 for both axis here. The desired image size is $M \times N$, and $(m,n)$ is the position of a pixel.

The columns of the basic function subset are calculated from $\mathbf{D}(p,q)$ as $\mathbf{K}_j = T(\mathbf{D}(p,q))$. $T$ is a map to assign every pixel in $\mathbf{D}(p,q)$ to the FEM element, which covers the pixel. and $j$ is the column index of $\mathbf{K}$. It is calculated as $j = q \cdot \sqrt{N_{DCT}} + p + 1$, e.g., $\mathbf{K}_3 = T(C(1,1))$.

The Jacobian matrix $\mathbf{J}$ is modified by the subset $\mathbf{K}$ as $\mathbf{J}_{DCT} = \mathbf{J}\mathbf{K}$. Hence, $\mathbf{J}_{DCT}$ maps the voltage variations to the DCT coefficients change. $\mathbf{J}_{DCT}$ contains only $n_{meas} \times n_{DCT}$ elements which are far less than the number of FEM elements. Then, the solution of the inverse problem is represented by the change of DCT coefficients $\hat{\mathbf{x}}_{DCT}$. The change of the DCT coefficients $\hat{\mathbf{x}}_{DCT}$ is used to restore the EIT image $\mathbf{H}$ through inverse DCT calculation.

In this contribution, we chose the Tikhonov regularization as $\mathbf{R} = \mathbf{I}$ for all algorithms. The optimal $\lambda$ is chosen when the noise figure (NF) reaches 0.5. The simulations were conducted with MATLAB R2019a (Mathworks, MA, USA) using the EIDORS toolbox [2]. 1% of the white noise was added to the voltages from the simulation.

## 3 Results

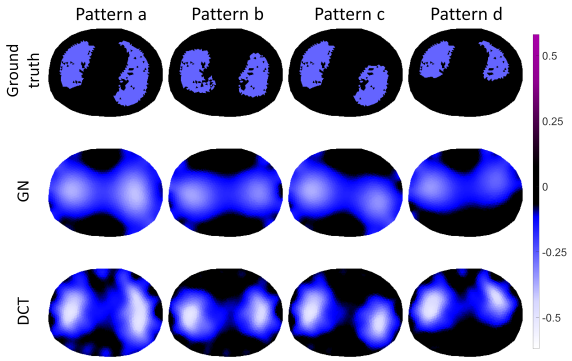


**Figure 1:** Ground truth and the EIT reconstructions. First row: different patterns of conductivity change for simulation (ground truth); second row: reconstructions using the GN approach; third row: reconstructions using DCT approach.

**Table 1:** The figures of merit of the reconstructions using GN approach and DCT approach.

| Figures of merit | Dislocation | | Shape deformation | | Ring effect | | Amplitude response | |
|---|---|---|---|---|---|---|---|---|
| Algorithm | GN | DCT | GN | DCT | GN | DCT | GN | DCT |
| Pattern a | 0.092 | 0.054 | 1.850 | 1.063 | 1.224 | 0.485 | 2.283 | 1.413 |
| Pattern b | 0.074 | 0.052 | 1.942 | 0.954 | 1.216 | 0.495 | 1.998 | 1.310 |
| Pattern c | 0.098 | 0.062 | 1.964 | 0.978 | 1.264 | 0.455 | 2.133 | 1.330 |
| Pattern d | 0.101 | 0.075 | 2.265 | 1.200 | 1.262 | 0.585 | 2.264 | 1.344 |

## 4 Conclusions

With the introduction of the 'inter-model' into the EIT reconstruction, the degrees of freedom in the inverse problem are reduced. According to the EIT images and the corresponding quantitative analysis, the DCT approach leads to the better results with more precision.

## References

[1] B. Gong, B. Schullcke, S. Krueger-Ziolek, M. Vauhkonen, G. Wolf, U. Mueller-Lisse, and K. Moeller, "EIT imaging regularization based on spectral graph wavelets," *IEEE transactions on medical imaging*, vol. 36, no. 9, pp. 1832–1844, 2017.

[2] A. Adler and W. R. B. Lionheart, "Uses and abuses of EIDORS: An extensible software base for EIT," *Physiological Measurement*, vol. 27, no. 5, pp. S25–S42, 2006.

# Data Compensation for Poor Electrode Contact in Electrical Impedance Tomography Based on CNN-LSTM Model

Jialun Li[12], Meng Dai[1], Shuhong Wang[2], Feng Fu[1]

[1]Department of Biomedical Engineering, Air Force Medical University, 710032 Xi'an, China
[2]School of Software Engineering, Xi'an Jiaotong University, Xi'an, China, fengfu@fmmu.edu.cn

**Abstract:** During the acquisition of electrical impedance tomography (EIT) data, the problem of electrode disconnection or poor connection often happens, resulting in artifacts in the final imaging results. This paper applies the CNN-LSTM algorithm to predict the acquired lung EIT data and thus interpolate the contaminated data.

## 1 Introduction

In many clinical applications of electrical impedance tomography, EIT electrodes accidentally have a poor connection with the patient's skin. These phenomena can result in the loss of measurement data and affect image reconstruction.

The current solutions to the faulty electrode include Adler's use of maximum posterior (MAP) to correct the data error caused by the change of electrode position during breathing [3], and Hartinger's simulation method proposed on the basis of MAP to obtain prior information of compensating electrode data [1]. In this study, we attempted the ability of convolutional neural network to extract features to achieve more accurate prediction of missing data.

## 2 Methods

We used PyTorch(3.8) to build a Convolutional Neural Network(CNN), and Long Short-Term Memory Network(LSTM) hybrid model to implement the prediction. The model consists of two main parts; the first part, CNN is used to extract features and act as a feature extractor; the second part, LSTM[2] is used to learn the temporal features extracted by the CNN. We used a one-dimensional convolutional neural network with three kernels, each followed by a batch normalization layer and then by a maximum pooling layer (1x3 kernel), improving generalisability and reduces dimensionality. A dropout is used after the fully connected layer to prevent overfitting during training. A fully con- nected layer reduces the feature size and performs dimen- sionality swapping before passing to the LSTM layer.

Lung ventilation EIT data from healthy adults provided by Dräger were used, with relative excitation between electrodes and measured adjacent to each other. The study simulated the disconnection of electrode No.1 at a particular moment in time. Before the electrode falls off, the EIT data is used as the training set in a CNN-LSTM model to obtain the predicted values. We used the R-Square to evaluate the regression prediction algorithm. If the result is 1, the model is error-free. If the result is 0, the model fits poorly.

## 3 Result

Before interpolating the data, we analyzed the correlation between the predicted data and the actual data, as shown in Figure 1. This regression model was evaluated with R-Square = 0.8446 after 30 epochs of training.

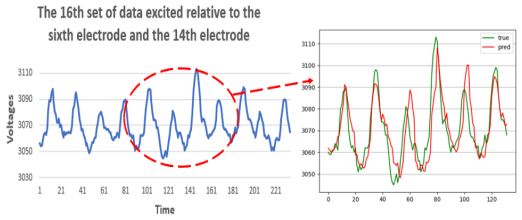


**Figure 1:** Data trend analysis: Predicted results(red) vs. True values(green) in Original data(blue)

As shown in Figure 2, (a) is the original lung ventilation imaging with actual value data; (b) is the imaging with missing data after the simulated electrode falls off; and (c) is the imaging after filling in the predicted values to completion. The comparison shows that relatively complete and continuous lung ventilation images can be obtained after prediction by the model.

## 4 Conclusions

This paper proposes a CNN-LSTM-based framework to address the problem of data loss due to poor electrode connectivity in clinical Settings. It is an effective supplementary method for this problem.

## 5 Acknowledgements

This work was supported by NFSC(52277235).

## References

[1] Hartinger AE, Guardo R, Adler A, Gagnon H. *IEEE transactions on bio-medical engineering.*, 56(2), 369–377,2008
[2] Hochreiter S, Schmidhuber J. *Neural Comput.*, 9(8):1735-1780, 1997
[3] Adler, Andy. *Physiological Measurement vol.*, 25(1), 227–238, 2004

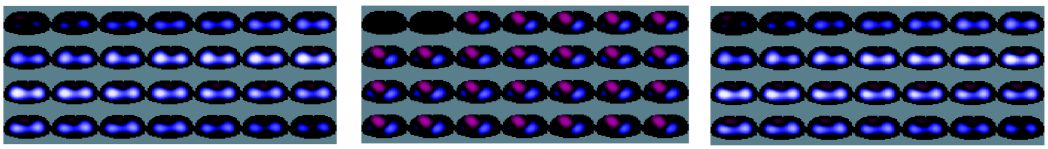

(a) Original image (b) Electrode No.1 disconnected (c) Predicted results image

**Figure 2:** Predicted results imaging comparison

# Separation of ventilation and cardiac activity on recorded voltages before EIT image reconstruction

Alberto Battistel[1], Erik Stein[1], Rongqing Chen[1], Knut Möller[1]

[1]Institute of Technical Medicine (ITeM), Furtwangen University (HFU), Jakob-Kienzle-Strasse 17, 78054 Villingen-Schwenningen, Germany

**Abstract:** Electrical impedance tomography is mostly employed to monitor the patients ventilation. However, it contains also their cardiac activity. Here we separate the ventilation and the cardiac activity signals through an harmonic analysis directly from the EIT voltages and reconstruct ventilation and cardiac-related independent images.

## 1 Introduction

Electrical Impedance Tomography (EIT) is used to monitor the variation of impedance. It is usually employed to observe the ventilation of a patient at the bedside as the inhalation and exhalation of air has a large influence on the lungs' conductivity.

Nevertheless, the heart deformation and blood flow produced by the cardiac activity also produces a change on the local conductivity [1]. However, these changes are order of magnitude smaller than those induced by the patient's ventilation [1]. Nevertheless, we showed that through an harmonic analysis it is possible to separate the signals belonging to the ventilation from those belonging to the cardiac dynamics [2, 3]. This was achieved working on the pixels of the EIT frames after the EIT images were already reconstructed from the raw data.

However, EIT image reconstruction is an ill-posed nonlinear inverse problem which inevitably add artifacts to the images. Separating the cardiac-related signals from the reconstructed images may exacerbate these artifacts. Here, we show that it is possible to apply the harmonic analysis on the raw voltages directly as displayed in Fig. 1. The first row shows the model and the trend of the voltages measurements. From these two sets of raw data are then obtained: one containing only the ventilation signals and one with only the cardiac activity (second raw of Fig. 1). Then finally two series of EIT images can be reconstructed (third row of Fig. 1). These images contain information pertinent to only the cardiac activity and to only the ventilation.

## 2 Methods

Simulated data and clinical data were used. The separation of ventilation and cardiac-related signals was applied on the EIT voltages as well as directly on the EIT images.

## 3 Results

The harmonic analysis performs well on to the raw data of the EIT consisting of voltage measurements. It generates two sets of voltages measurements, one with only the conductivity changes given by the ventilation and one with the changes given by the cardiac-related signals. These can be successfully used to reconstruct two sets of EIT images which independently display the ventilation and the cardiac activity.

Moreover, some noise from the voltage measurements can be rejected, which we expect it may increase the stability and reliability of the EIT image reconstruction.

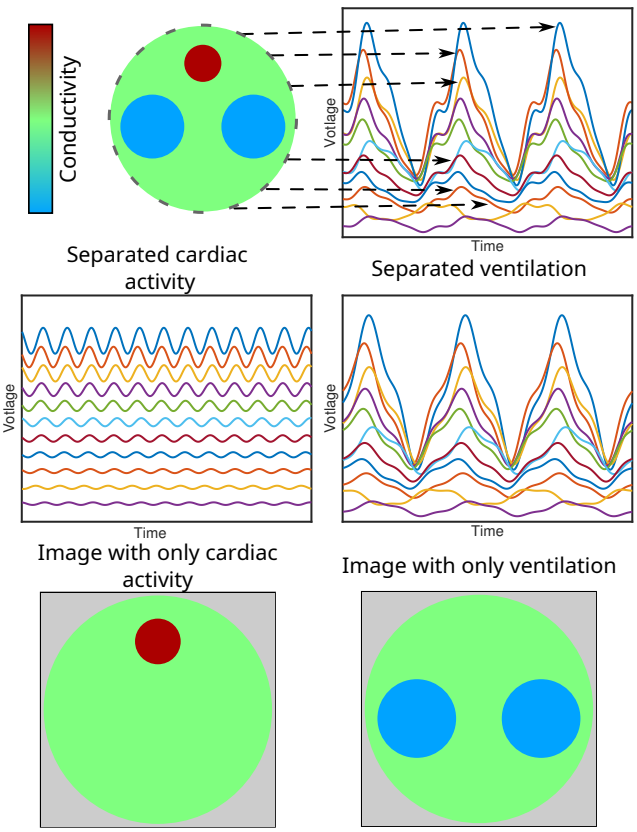


**Figure 1:** Schematic to represent the procedure to construct EIT images containing only the ventilation and only the cardiac activity from the EIT raw voltage measurements.

However, the quality of the independent reconstructed images is affected by the specific reconstruction algorithm employed.

## 4 Conclusions

It is possible to separate ventilation and cardiac-related signals in EIT directly from the raw voltage measurements and use the separated signals to reconstruct EIT images which display separately the activity of the ventilation and of the cardiac dynamics.

## 5 Acknowledgments

This research was partially funded by the BMBF (MOVE, Grant 13FH628IX6), H2020 MSCA Rise (#872488 DCPM), and AIRLobe (32-7545.220/42/1).

## References

[1] JM Deibele, H Luepschen, S Leonhardt *Physiol. Meas.*, 29: S1–S14, 2008

[2] A Battistel, C Rongqing, N Hallemans, R Pintelon, J Lataire, K Möller, *IFAC-PapersOnLine*, 54: 281–286, 2021

[3] A Battistel, C Rongqing, N Hallemans, R Pintelon, J Lataire, J Lovas, K Möller, *AUTOMED 2021*, Basel, Switzerland, 2021

# Sensitivity-Volume Figure of Merit for EIT Measurement Selection

Claire Onsager[1], Chulin Wang[1], Charles Costakis[1], Can Aygen[1], Lauren Lang[1], Suzan van der Lee[2], Matthew A Grayson[1]

[1]Department of Electrical and Computer Engineering, Northwestern University, Evanston, IL, USA, m-grayson@northwestern.edu

[2]Department of Earth and Planetary Sciences, Northwestern University, Evanston, IL, USA

**Abstract:** Optimizing the electrical impedance tomography (EIT) problem requires selection of noise-robust measurements that are highly sensitive to model changes. In this work we propose a mathematically rigorous figure of merit to select optimal measurements derived from the sensitivity, or Jacobian, matrix in the linearized forward problem.

## 1 Introduction

The large contact number $C$ needed for high resolution EIT imaging presents a measurement optimization problem, particularly in 3D. Four-point resistance measurements that use two current and two voltage probes are typically chosen in an *ad hoc* manner whereby sets are compared after solving. We propose a metric in Ref. [1] for derivation of optimally noise-robust measurements for any EIT problem, by utilizing the sensitivity information in the Jacobian of the linearized EIT problem that maps a given finite element model of sample conductivity to a chosen measurement set.

## 2 Methods

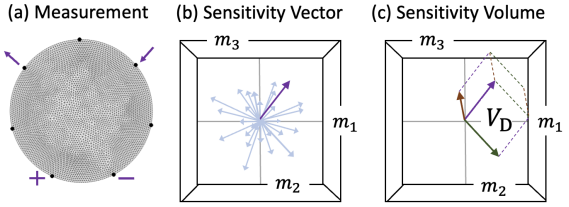


**Figure 1:** (a) An individual 4-point measurement. (b) A sensitivity vector in model-space corresponding to that data measurement (purple) surrounded by sensitivity vectors of other measurements (light blue). (c) Parallelotope with sensitivity-volume $V_D$ in model-space projected from a data-space consisting of three sensitivity vectors corresponding to three measurements.

With a large number of contacts $C$, it becomes impractical to take every possible independent measurement, requiring a new figure of merit to determine which measurement subsets are superior. Consider each row of the Jacobian as a *sensitivity vector* in model-space representing how sensitive each measurement is to conductivity changes in each finite element mesh piece. The highest sensitivity measurements have both a strong signal and a dissimilarity from other measurements, corresponding to sensitivity vectors of large magnitude and high mutual orthogonality. Therefore, the *sensitivity-volume* of the parallelotope defined by a set of sensitivity vectors represents the overall sensitivity of that measurement-set. The sensitivity-volume can be calculated from the mutually perpendicular components of the individual sensitivity vectors. Equivalently, the squared sensitivity-volume $V_{\mathrm{D}}^2$ equals the determinant of the Jacobian times its transpose. This method uses every element in the Jacobian rows to define sensitivity, as opposed to the use of Jacobian columns in the EIT literature to define a sensitivity map [2] or a sum of Jacobian elements related to a region of interest [3].

Measurement-sets were optimized using sensitivity-volume as a figure of merit. By increasing contact number $C$ by a factor of three larger than that strictly needed for the desired amount of independent information, the search space broadens [3] to allow selection of the same number of measurements $D$ with much larger sensitivity-volumes. Finite element modeling and Jacobian calculations were performed using EIDORS version 3.10 with Netgen [4].

## 3 Results

Measurement sets with maximal sensitivity-volume figure of merit for the 2D circular problem produce Jacobians with much larger singular values $s_i$ and lower condition numbers when compared with the standard Sheffield measurement-set [5], as seen in Table 1. The $D$-th root of the maximal sensitivity-volume measurement-set compared to that associated with the Sheffield measurement-set gives the relative noise-robustness $n = \sqrt[D]{V_D/V_{\mathrm{sheff}}}$. For the 2D problem, this method demonstrates an order of magnitude improvement in noise-robustness over the typical Sheffield measurements (Table 1). These gains are expected to greatly increase with the larger contact number $C$ of the 3D-problem.

**Table 1:** Sensitivity-volume for optimized measurement-set relative to the Sheffield measurement-set in terms of relative noise-robustness $n$, largest singular value $s_1$, and condition number $s_1/s_{14}$. An order of magnitude improvement in noise-robustness per measurement is observed for the same number of measurements as the Sheffield set.

| | $C$ | $D$ | $n$ | $s_1$ | $s_1/s_{14}$ |
|---|---|---|---|---|---|
| Optimized | 21 | 14 | 9.23 | $9.82\text{x}10^{-5}$ | 4.98 |
| Sheffield | 7 | 14 | 1 | $1.96\text{x}10^{-5}$ | 21.19 |

## 4 Conclusions

The sensitivity-volume figure of merit presented here provides a useful metric for deriving optimally noise-robust measurements. As the EIT problem complexity increases with increasing contact number from 2D to 3D, this metric can robustly optimize the measurement-set for arbitrary contact number and arbitrary contact positioning.

## 5 Acknowledgements

This work was supported by NSF grants ECCS-1912694 and DMR-1720139.

## References

[1] C Onsager, et al. *arXiv PREPRINT:* 2111.01397, 2021,
[2] B Grychtol, B. Müller, A Adler *Physiol. Meas.*, 37:785-800, 2016
[3] C Coxson, et al. *Inverse Problems*, 38:085007, 2022
[4] A Adler, W R B Lionheart *Physiol. Meas.*, 27:S25-S42, 2006
[5] DS Holder *Electrical Impedance Tomography* IOP Publishing: Bristol, 2005

# Distinguishability and Noise in the Sensitivity-Volume EIT Method

Claire Onsager[1], Chulin Wang[1], Charles Costakis[1], Can Aygen[1], Lauren Lang[1], Suzan van der Lee[2], Matthew A Grayson[1]

[1]Department of Electrical and Computer Engineering, Northwestern University, Evanston, IL, USA, claireonsager2024@u.northwestern.edu

[2]Department of Earth and Planetary Sciences, Northwestern University, Evanston, IL, USA

**Abstract:** Electrical impedance tomography (EIT) experiments must tolerate the presence of experimental noise. Thus, high fidelity reconstructions require optimally noise-robust measurements to distinguish features. This work uses a modified distinguishability metric in the sensitivity-volume method to show increased noise tolerance.

## 1 Introduction

In the application of EIT for medical imaging, for example, it is necessary to differentiate between two similar states, such as the size of the heart, in the presence of experimental noise. In such EIT monitoring systems, measurement sets, defined as a collection of four-point measurements taken by electrodes around the body, must be noise-robust to produce high-fidelity results. In the sensitivity-volume method introduced by the authors [1], the sensitivity information in the Jacobian is utilized for optimal measurement-set selection. Following Adler [2], a distinguishability metric for EIT allows measurement-set comparisons of noise tolerance in the the sensitivity-volume method [1].

## 2 Methods

Inspired by Ref [2], the sensitivity-volume method defines distinguishability as follows. Each inverse-solve in the presence of noise produces a model-vector $\mathbf{m}$ within a neighborhood of the noiseless inverse solution in model-space. A thousand inverse solves under noise produce a mean model-space vector $\overline{\mathbf{m}} = E[\mathbf{m}]$ with a covariance matrix $\mathbf{\Sigma}$. In the present example, consider a "normal heart" with mean model-vector $\overline{\mathbf{m}}_\mathrm{n}$ to be distinguished from an "enlarged heart" with mean model-vector $\overline{\mathbf{m}}_\mathrm{l}$. The projected-covariances $\Delta m_\mathrm{n}$ and $\Delta m_\mathrm{l}$ are the components of $\mathbf{\Sigma}_\mathrm{n}$ and $\mathbf{\Sigma}_\mathrm{l}$ along the difference in mean model-vectors, $\Delta m^2_{\mathrm{n,l}} = \hat{\mathbf{u}}^\mathsf{T}\mathbf{\Sigma}_{\mathrm{n,l}}\hat{\mathbf{u}}$, where $\hat{\mathbf{u}}$ is the unit vector pointing from $\overline{\mathbf{m}}_\mathrm{n}$ to $\overline{\mathbf{m}}_\mathrm{l}$. Distinguishability $z$ can then be defined as the model-space distance between the two mean model-vectors relative to the combined projected-covariances,

$$z = \frac{||\overline{\mathbf{m}}_\mathrm{l} - \overline{\mathbf{m}}_\mathrm{n}||}{\sqrt{\Delta m^2_\mathrm{n} + \Delta m^2_\mathrm{l}}}, \tag{1}$$

where $z = 1$ is the threshold for distinguishability and $z < 1$ is considered indistinguishable. The corresponding noise threshold $\eta_t$ is the noise $\eta$ at which $z = 1$. This work used EIDORS to simulate the forward problem for a circular sample with offset interior circles representing normal and enlarged hearts [3]. Gaussian noise of various standard deviations $\eta$ was added to each dataset before inverse solving using a Zernike polynomial-based, non-iterative Singular Value Decomposition (SVD) solver as described in Ref [1]. One thousand solves were done at each $\eta$. Distinguishability, as defined above, was used to compare the standard Sheffield measurement-set [2] with a Sensitivity-volume method derived measurement-set [1].

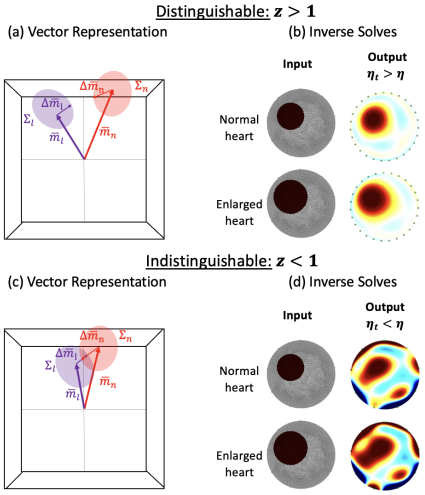


**Figure 1:** (a) Vector representation of distinguishable results ($z > 1$), where the mean inverse solutions ($\bar{m}_l, \bar{m}_n$) are far enough apart in model-space such that the projected covariances ($\Delta\bar{m}_l, \Delta\bar{m}_n$) do not overlap. (b) Normal and enlarged heart inverse reconstructions in the distinguishable case. (c) Vector representation of indistinguishable results ($z < 1$), where the mean inverse solutions are close together in model-space and the projected covariances overlap. (d) Normal and enlarged heart inverse reconstructions in the indistinguishable case.

## 3 Results

Upon comparison with this distinguishability metric, it was found that the sensitivity-volume measurement-sets [1] could withstand $30\times$ more noise before the normal and an enlarged heart became indistinguishable. The sensitivity-volume optimized measurement-set demonstrated distinguishability $z > 1$ for any noise less than the threshold $\eta_t = 3.2 \times 10^{-6}$. By contrast, the standard Sheffield measurement-set for the same number of measurements had a noise threshold of only $\eta_t = 0.13 \times 10^{-6}$.

## 4 Conclusions

The definition of distinguishability for the sensitivity-volume method described here provides an intuitive visual representation of the enhanced noise tolerance in model-space. In biomedical EIT, such measurement-sets will produce reliable, high quality EIT data.

## 5 Acknowledgements

This work was supported by NSF grants ECCS-1912694 and DMR-1720139.

## References

[1] C Onsager, et al. *arXiv PREPRINT:* 2111.01397, 2021
[2] A Adler, P O Gaggero, Y Maimaitijiang *Physiol. Meas.*, 32:731, 2011
[3] A Adler, W R B Lionheart *Physiol. Meas.*, 27:S25-S42, 2006

# Using Machine Learning to Detect Prostate Cancer intraoperatively: A Simulation Study

Kofi Odame[1], Ethan Murphy[1], and Ryan Halter[1]

[1]Thayer School of Engineering, Dartmouth College, Hanover, NH, USA,

**Abstract:** This work describes preliminary results in using machine learning (ML) to quickly determine if tissue probed by an impedance-based surgical margin assessment (SMA) device is in contact with prostate cancer. Simulated ex vivo prostate slices are generated with tumor inclusions and a smooth noisy background. A gated recurrent unit (GRU) neural network is trained to detect cancer, yielding an accuracy of 98%.

## 1 Introduction

Prostate cancer is the 2nd most common cancer in the United States (US). In 2019, there were 224,730 new diagnoses of prostate cancer in the US and 1.4 million new cases globally [1]. Many of these patients (> 1/3rd) are expected to undergo radical prostatectomy (RP) [2], wherein the entire prostate is removed. To improve outcomes, we have been investigating the use of an impedance-based SMA probe to provide real-time feedback to surgeons about the extent of remaining cancer. One aspect of this research is exploring fast ways to relate the impedance values to the presence of prostate cancer. Machine learning (ML) appears to be a promising method to do this – as long as the training and network are sufficiently robust to noise and disconnected or partially connecting electrodes.

## 2 Methods

In order to explore ML for SMA, we constructed a 5 mm thick 3D finite element method (FEM) mesh with the SMA probe's electrodes encoded on the top surface (Fig. 1A). This is used to replicate an ex vivo prostate slice, which we have used in prior and ongoing validation studies. A general software toolbox to output meshes like these is available on GitHub [3]. Tumor and background tissue are based on ex vivo tissues values ([4]) at 10 kHz. Smooth noise is added to the background via a radial-basis-function neural network, which is tuned to produce an overall standard deviation of background noise to be 10% - similar to what we might expect from real tissue (Fig. 1B). We created 4265 digital phantoms of prostate tissue slices that each contain a single circular inclusion of cancerous lesion. The diameters of the inclusions range uniformly from 0 mm to 3 mm, and each inclusion is located in a random part of the phantom. If a phantom contains an inclusion of diameter 1 mm or more, then we consider this phantom to be positive for cancer, otherwise it was as negative for cancer.

We simulated bioimpedance measurements for each phantom to produce a corresponding matrix of 28x33 single-ended voltages. These are the voltages generated at the 33 electrodes in response to each of the 28 current injection patterns used. We separated the 4265 matrices of single-ended voltages into three sets: 2559 for training, 853 for validation and 853 held out for testing. We used these datasets to train, validate and test a neural network for classifying a phantom sample as either positive or negative for cancer.

Our gated recurrent unit neural network has the following architecture. Layer 1: 33-unit input layer; Layer 2: gated recurrent unit layer (4 units); Layer 3: fully-connected layer (2 units); Layer 4: softmax (2 units). To train the neural network, we performed backpropagation over 500 epochs, using the ADAM optimizer and a mini-batch size of 400.

## 3 Conclusions

Figure 1C shows the confusion matrix results when the trained neural network is presented with the previously-unseen, held out test dataset. The classification accuracy for the test dataset is 98%. Additional simulation experiments have been performed with up to 5 bad electrodes, which reduced the accuracy to 93%. Ex vivo bovine tests are planned to help validate the approach. Following this we plan to evaluate the approach on ex vivo prostate data.

## References

[1] USCS Data Visualizations - CDC. (n.d.). Retrieved January 04, 2023, from https://gis.cdc.gov/Cancer/USCS/DataViz.html
[2] W Lowrance, et al. *J Urol*, 187(6):2087-2093, 2012
[3] https://github.com/ethankmurphy/flatPCB_EIT_mesh_construction
[4] Halter, R. J. of Urol., 182(4), pp.1600-1607, 2009

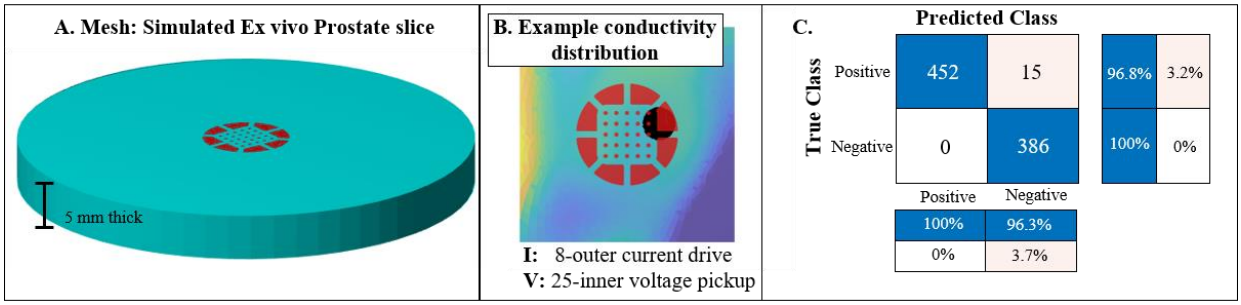


**Figure 1: A.** Mesh representing SMA probe measuring on the surface of an ex vivo prostate slice (generally ~5 mm in thickness) B. An example conductivity distribution; smooth background noise constructed with an RBF network aiming for 10% background noise, and a cylindrical inclusion on the top right of the SMA probe. The large 8 red electrodes are current drive and the 25 small electrodes are used for voltage pick-up. C. Shows the ML results in terms of a confusion matrix.

# Resolution as a function of Stimulation and Measurement Patterns

Andy Adler[1] and Zhanqi Zhao[2]

[1]Systems and Computer Engineering, Carleton University, Ottawa, Canada
[2]Institute of Technical Medicine, Furtwangen University, Villingen-Schwenningen, Germany

**Abstract:** Pair-drive EIT systems can be described by a *skip* parameter – the separation between excitiation and measurement pairs. A larger skip distance increases the current flow through the centre of the body and thus improves the distinguishability of the EIT images. Low skip values improve resolution. We discuss the origin of this result.

## 1 Introduction

Most EIT systems use pair drive and measurements: current is applied between electrodes separated by $skip_{\text{stim}}$ and voltage is measured separated by $skip_{\text{meas}}$. In this scenario the adjacent (Sheffield) configuration is $skip_{\text{stim}} = skip_{\text{meas}} = 0$. A number of authors have looked at the distinguishability of EIT and shown that it increases as a function of *skip* [2–4]. However, our experience shows that stimulation and measurement patterns (SMP) which maximize distinguishability do not show the best resolution.

For example, Fig 1 shows typical images with adjacent and larger skip patterns. Left shows better lung separation, but also a central inverse region.

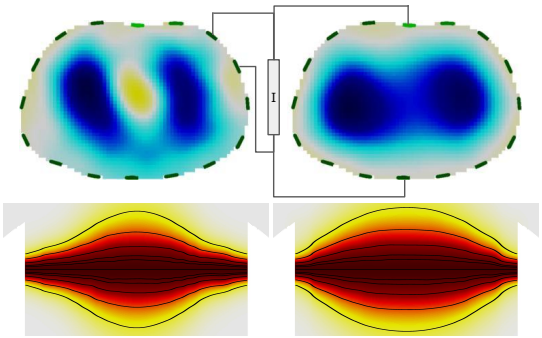

**Figure 1:** *Top*: Tidal breathing in healthy subject for different SMP. Left: $skip_{\text{stim}} = skip_{\text{meas}} = 0$. Right: $skip_{\text{stim}} = 7$, $skip_{\text{meas}} = 0$. *Bottom*: Vertical sensitivity in coronal plane; contour lines show sensitivity fraction of maximum: 25%, 50%, 75%, 90%, 95%.

The goal of our study is to explore this unexpected result: why do adjacent SMP have improved resolution but decreased distinguishability compared to larger skip patterns. Fig 1 (bottom) shows adjacent patterns have lower off-plane sensitivity [1]. These lung regions are "pushed" toward the image centre, and this effect increases with skip.

## 2 Methods and Results

Difference EIT reconstruction estimates an image (2D for this paper) $\hat{\mathbf{x}} = \mathbf{R}_{\text{SMP}}\mathbf{y}$, from difference measurements $\mathbf{y}$ and a SMP-dependent reconstruction matrix $\mathbf{R}$.

Our calculations of image resolution vs SMP are shown in Fig 2. The *distinguishability* of EIT has been defined as area-weighted image amplitude $\sum_A \hat{\mathbf{x}}$ for a small contrast (Fig 2B). This parameter varies with spatial position and is largest near the electrodes. Image resolution can be defined by the ability of EIT to resolve high spatial-resolution features. Fig 2C and 2D show horizontal and vertical circles split into positive and negative halves.

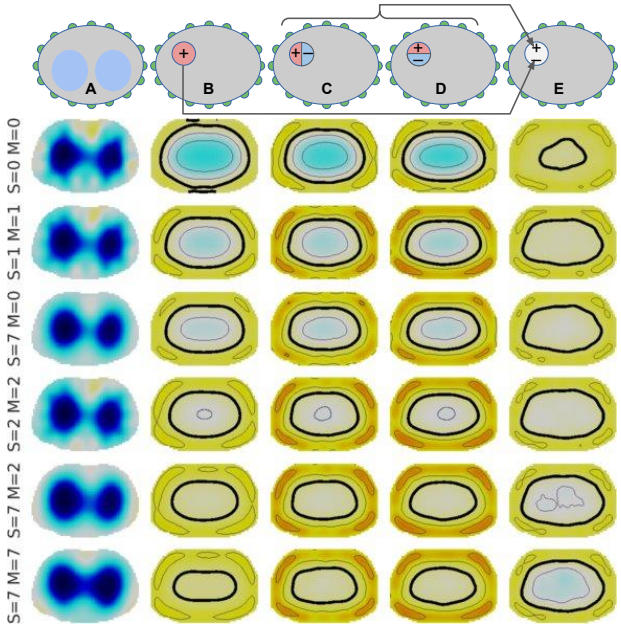


**Figure 2:** Distinguishability and resolution for several SMP (Stim(S) and Meas(M) skip at right). From left to right: amplitude image, distinguishability, horizontal and vertical resolution and ratio (resolution/distinguishability). The top row illustrates the calculation: each circle in rows B–E is swepth across the image to each pixel location. Colours correspond to log-sensitivity (yellow larger, blue smaller) Contour lines and shown with a bold reference level across images.

Reconstruction of such a target requires resolution. Finally, the ratio between resolution and distinguishability is shown in Fig 2E. Several features can be seen in Fig 2. First, in the amplitude image, we see poor resolution as skip increases. The adjacent (S=0,M=0) protocol has low distinguishability and a higher resolution, but has a larger ratio in the center (2E). Conversely, as skip increases, the ratio decreases in the center, even as the overall distinguishability and resolution increase.

## 3 Discussion

We consider the paradoxical result that adjacent SMP give often improved resolution images, while providing overall poor distinguishability. Here we show a measure of resolution based on nearby contrasts, and calculate the distinguishability/resolution ratio. Also, increased off-plane sensitivity at higher skip values "projects" more lung regions to the centre, and may also explain this effect.

## References

[1] A Adler, I Frerichs, B Grychtol "Off-plane sensitivity of EIT", p.68, Conf EIT 2015, Neuchâtel, Switzerland

[2] A Adler, PO Gaggero, Y Maimaitijiang, "Adjacent Stimulation and Measurement Patterns Considered Harmful", *Physiol Meas*, 32:731–744, 2011.

[3] D Isaacson, "Distinguishability of conductivities by electric current computed tomography", *IEEE T Med Imaging* 5:91–95, 1986.

[4] WRB Lionheart *et al*"Generalized optimal current patterns and electrical safety in EIT", *Physiol Meas* 22:85–90, 2001.

# Reciprocity in electromagnetic systems

Andy Adler[1] and William R.B. Lionheart[2]

[1]Systems and Computer Engineering, Carleton University, Ottawa, Canada
[2]School of Mathematics, University of Manchester, UK

**Abstract:** We review reciprocity for electromagnetic (E&M) systems, including EIT. We note that reciprocity is valid for all linear E&M systems and that it is closely related to reciprocity in circuit theory. The correct reference for earliest work is Lorentz (1895).

## 1 Introduction

"Reciprocity" refers to a mutual and equivalent exchange. The term has been used in electrical engineering and phyics to refer to the equivalences when exchanging electromagnetic sources and fields. In Fig 1, $V_{ab} = V_{cd}$ if $I_{cd} = I_{ab}$, since the electrode positions, electrical networks and roles are reciprocal. This example illustrates the two reciprocity results, for electrical networks and for electromagentic systems generally.

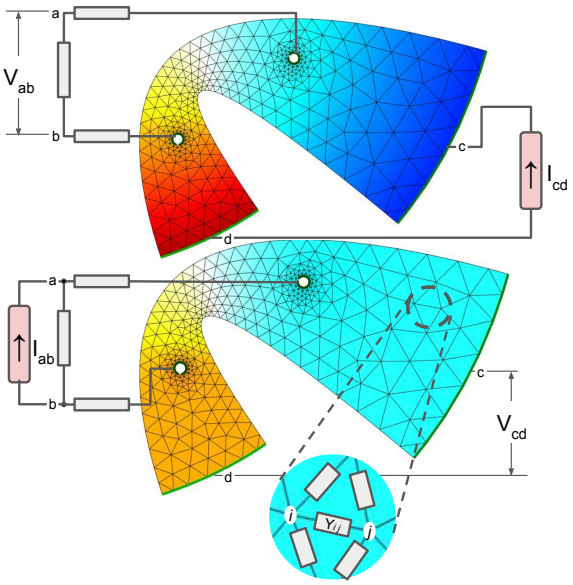


**Figure 1:** Illustration of reciprocity. In the upper figure, current ($I_{cd}$) is applied between outer electrodes and voltage ($V_{ab}$) meausured through a resistor network. In the lower figure these are reversed. Colour corresponds to voltage in the medium. The lower inset illustrates the discretization of the medium onto an electrical network, where nodes $i$ and $j$ are connected by admittance $Y_{ij}$.

## 2 Reciprocity in Electromagnetic Systems

Reciprocity is valid for linear, passive electromagnetic media, with sinusoidal electric field ($\vec{E}$) and current density ($\vec{J}$) and complex conductivity $\sigma^* = \sigma + i\omega\epsilon$.

$$\vec{J} = \left[\sigma^* - (i\omega\mu)^{-1}(\nabla \times \nabla\times)\right] \vec{E} \qquad (1)$$

where $\times$ represents the cross product.

Consider a current density $\vec{J}_1$ with angular frequency $\omega$ which produces electric and magentic fields $\vec{E}_1$ and $\vec{H}_1$, as well as another current $\vec{J}_2$ and fields $\vec{E}_2, \vec{H}_2$. If we have an isolated system with no energy from the outside, the reciprocity theorem [2] says:

$$\int \vec{J}_1 \cdot \vec{E}_2 dV = \int \vec{J}_2 \cdot \vec{E}_1 dV \qquad (2)$$

This is the Lorentz reciprocity, published in 1895 following analogous results on sound and light (for a history, see [3]).

Within the EIT community, it has been common to cite Geselowitz [1] who rediscovered the analogous theorem in electrostatics (Green's reciprocity). The Lorentz reciprocity is more general and applies to all linear electromagnetic networks. It is not valid for non-linear elements (e.g. diodes).

## 3 Reciprocity in Electrical Networks

Linear, passive electrical networks are reciprocal for currents and voltages measured at any two ports (such as A and B in Fig 1). Such networks can be characterized by an admittance matrix $\mathbf{Y}$, which relates the voltage on all nodes, $\mathbf{V}$, to the current flowing into each note, $\mathbf{I}$, via $\mathbf{I} = \mathbf{YV}$. Setting $V = 0$ on a ground node we have reduced matrices (not including the ground node) $\tilde{\mathbf{I}}$, $\tilde{\mathbf{V}}$, and $\tilde{\mathbf{Y}}$, and calculate an impedance matrix $\tilde{\mathbf{Z}} = \tilde{\mathbf{Y}}^{-1}$, such that $\tilde{\mathbf{V}} = \tilde{\mathbf{Z}}\tilde{\mathbf{I}}$.

Any voltage measured on the network can be described by $v = \mathbf{t}^T\mathbf{ZI}$, where *test* vector $\mathbf{t}$ represents the gain on each network node (and specifically those corresponding to electrodes). For pair-drive EIT where current flows between nodes $a$ and $b$, $\mathbf{I}_a = -\mathbf{I}_b = I_{\text{applied}}$, with other elements in $\mathbf{I}_{ab}$ zero. Using a gain, G, between electrodes $c$ and $d$, $\tilde{\mathbf{t}}_{cd} = 0$ except for $\tilde{\mathbf{t}}_c = -\tilde{\mathbf{t}}_d = G$, Reciprocity follows from $\mathbf{Y}$ being symmetric, and thus $\mathbf{t}^t_{ab}\tilde{\mathbf{Z}}\tilde{\mathbf{I}}_{cd} = \mathbf{t}^t_{cd}\tilde{\mathbf{Z}}\tilde{\mathbf{I}}_{ad}$.

The symmetrical nature of $\mathbf{Y}$ may be motivated as follows: the body is discretized into points characterized by a voltage and current source. We conceptually build up the space from empty (no connections between points). When adding admittance $Y_{jk}$ then current $Y_{jk}(V_j - V_k)$ flows into $j$ and $Y_{jk}(V_k - V_j)$ flows into $k$. The admittance matrix, $\mathbf{Y}$, will increase by $Y_{jk}$ at $(j,k)$ and $(k,j)$ and decrease by $Y_{jk}$ at $(j,j)$ and $(k,k)$. $\mathbf{Y}$ will remain symmetrical unless external power drives more current into $j$ than leaves $k$.

## 4 Discussion

Within the EIT community, it has sometimes not been clear that reciprocity has a longstanding mathematical consideration and that it applies to all electromagnetic problems. The goal of this abstract is to illustrate the relationship between reciprocity in electromagnetic systems and electrical networks, and to describe its origin in less mathematical terms. We recommend that for EIT papers citing the *reciprocity theorem*, the best and original reference is [2].

## References

[1] DB Geselowitz, "An Application of Electrocardiographic Lead Theory to Impedance Plethysmography" IEEE T Biomed Eng, 18:38–41, 1971

[2] HA Lorentz, "Het theorema van Poynting over de energie in het electromagnetisch veld en een paar algemeene stellingen over de voortplanting van het licht" Proc Koninklijke Akademie van Wetenschappen 4:176–187, 1895.

[3] RJ Potton, "Reciprocity in optics" Prog Physics 67:717–754, 2004.

# A Deep Neural Network for a Hemiarray EIT System

Mason Manning[1], Nicholas Wharff[2], Shelby Horth[3], Jacob Roarty[4], *Malena I. Español[4], *Rosalind Sadleir[5]

[1]School of Human Evolution and Social Change, Arizona State University (ASU), Tempe, AZ, United States
[2]Department of Mathematics and Computer Science, Drake University, Des Moines, IA, United States
[3]Department of Applied Mathematics and Computer Science, Wake Forest University, Winston-Salem, NC, United States
[4]School of Mathematical and Statistical Sciences, Arizona State University, Tempe, AZ, United States, mespanol@asu.edu

[5]School of Biological and Health System Engineering, Arizona State University, Tempe, AZ, United States, rsadleir@asu.edu

**Abstract:** We extend the deep neural network EIT algorithm presented in [2] to the case of an electrode array placed only on an anterior portion of the body.

## 1 Introduction

We introduce a deep neural network (DNN) algorithm for the case where we have a hemiarray (HA) of electrodes. This topology is appropriate for applications where part of a subject abdomen is unavailable. For example, when a patient has spinal injuries. We followed the work of [2], where a DNN was developed for a full array (FA) of electrodes.

## 2 Methods

The EIT inverse problem is highly ill-posed and provides limited information about the internal voltage distribution. An HA configuration exacerbates this issue by further reducing available information. The reduction in information makes pattern recognition harder, increasing the likelihood of a DNN picking up on idiosyncrasies or patterns in the training data that do not represent the broader problem (i.e., overfitting). However, since the voltage measurements of the FA configuration almost entirely cover the HA configuration, except for the 1st and 8th electrodes, we initialized the shared weights of the HA-DNN with the trained FA-DNN to reduce the risk of overfitting. While this can also make the DNNs more logically consistent, it is not guaranteed since fine-tuning is required for the weights associated with the 1st and 8th electrode measurements.

**FA DNN:** The network consisted of three hidden layers of fully connected layers, with 60 nodes in each layer, and used the logistic sigmoid function as the activation function. The input layer contained 208 boundary voltage inputs, while the output layer contained the conductivity of the 576 pixels in the mesh. The DNN was trained for 300 epochs with mean squared error (MSE) loss, using 100 batch size. Techniques including Dropout, L2 regularization, and stacked autoencoders (for pretraining) were used to optimize fit.

**HA DNN:** The HA-DNN has 40 boundary voltage inputs, 29 of which are shared with the FA-DNN. The weights associated with the shared measurements were initialized based on the trained FA-DNN, while the remaining weights were randomly assigned. The network was fine-tuned for 80 epochs using a batch size of 100 and the MSE loss function on a training set of 10,000 unique samples with randomly placed circular and square anomalies with various conductivities [1]. Test data was created with a finer mesh to check for overfitting and introduce new complexities.

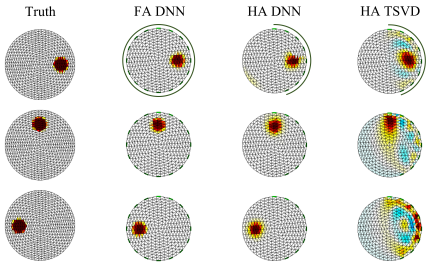


**Figure 1:** The first column shows the true internal conductivity, while the second and third columns show predictions by FA-DNN and HA-DNN, respectively. The fourth column shows TSVD prediction using hemiarray data.

## 3 Conclusions

The HA-DNN outperformed traditional methods such as TSVD and Tikhonov when using the hemiarray configuration. Moreover, despite having significantly fewer inputs than the FA-DNN, the HA-DNN produced only slightly worse predictions. These findings suggest that DNNs, particularly the HA-DNN, are promising for accurately predicting internal conductivity. Further research is needed to assess these results' generalizability and optimize DNN architectures for specific applications.

## 4 Acknowledgements

This work was initiated during the 2022 QRLSSP REU at the Levin Center at ASU and was partially supported by grants from the NSF (DMS-1757968 and FAIN-2150492), the NSA (H98230-20-1-0164), the Office of the President, and the Office of the Provost of ASU.

## References

[1] Adler, A., & Lionheart, W. R. *Physiol Meas*, 27(5), S25, 2006
[2] Li, X., et al. *Trans. Inst. Meas. Control*, 41.14: 4035-4049, 2019

**Table 1:** The table presents a comparison of the out-of-sample amplitude response (AR) across various radial and angular positions. AR measures the ratio of image pixel amplitudes in the target to that in the reconstructed image.

| | FA-DNN | HA-DNN | HA-TSVD | HA-Tikhonov |
|---|---|---|---|---|
| MEAN | 0.994 | 1.10 | 0.82 | 0.958 |
| STD | 0.03 | 0.11 | 0.27 | 0.43 |

# On the required number of electrodes in an EIT-related problem

Andrej Brojatsch[1] and Bastian Harrach[1]

[1]Chair for Numerical Analysis, Goethe University, Frankfurt, Germany, brojatsch@math.uni-frankfurt.de

**Abstract:** We consider the problem of reconstructing an unknown Robin transmission coefficient on a known interior boundary from voltage/current measurements on electrodes attached to an outer boundary. We derive a criterion to check whether the number of electrodes is sufficient for unique solvability of the resulting non-linear inverse problem.

## 1 Design considerations

Non-destructive EIT-based corrosion detection holds the challenge of solving the inverse Robin transmission problem where the corrosion function on the boundary of an interior object $D$ is to be determined from voltage/current measurements on the boundary of an outer domain $\Omega$ (as in Fig. 1).

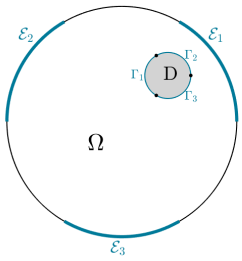


**Figure 1:** Domain $D \subset \Omega$ with electrodes $\mathcal{E}_1, \dots, \mathcal{E}_m \subset \partial\Omega$.

Our model: Applying electric currents $I_1, \dots, I_m \in \mathbb{R}$ to electrodes $\mathcal{E}_1, \dots, \mathcal{E}_m \subset \partial\Omega$ and measure the necessary voltages $U_1, \dots, U_m \in \mathbb{R}$. The aim is to detect the corrosion parameter $\hat{\gamma} \in L^\infty_+$ on the inner boundary $\Gamma$ from measurements. The electric potential $u \in H^1(\Omega)$ solves

$$(*) \quad \begin{cases} \Delta u &= 0 & \text{in } \Omega \setminus \Gamma, \\ \int_{\mathcal{E}_k} \partial_\nu u \, \mathrm{d}s &= I_k & \text{for } k = 1, \dots, m, \\ \partial_\nu u &= 0 & \text{on } \partial\Omega \setminus \bigcup_{k=1}^m \mathcal{E}_k, \\ [\![u]\!]_\Gamma &= 0 & \text{on } \Gamma, \\ [\![\partial_\nu u]\!]_\Gamma &= \hat{\gamma} u & \text{on } \Gamma, \\ u\big|_{\mathcal{E}_k} = \text{const.} &=: U_k & \text{for } k = 1, \dots, m \end{cases}$$

with $[\![\varphi]\!]_\Gamma = \operatorname{trace}\left(\phi|_{\Omega\setminus D}\right) - \operatorname{trace}\left(\phi|_D\right)$.

The measurement of the voltage $U \in \mathbb{R}^m$ along the electrodes corresponding to the applied currents $I \in \mathbb{R}^m$ is given by the map $\mathcal{F}\colon [a,b]^n \to \mathbb{R}^{m\times m}$ with

$$\mathcal{F}(\gamma) I = U, \quad \text{where } u_\gamma^{(I)} \text{ solves (*) and } u_\gamma^{(I)}\big|_{\mathcal{E}_k} = U_k,$$

with a priori bounds $a < b$ for the piecewise constant $\hat{\gamma}$ s.t. $a \le \left(\sum_{i=1}^n \hat{\gamma}_i \chi_{\Gamma_i}\right) \le b$. Here the $(jk)$-th component of $\mathcal{F}(\hat{\gamma})$ is the voltage at $\mathcal{E}_j$ when a current is applied to $\mathcal{E}_k$.

The resulting inverse problem states as

(**) determine $\hat{\gamma} \in [a,b]^n$ from the knowledge of $\mathcal{F}(\hat{\gamma})$.

**Remark:** The measurement map $\mathcal{F}$ is monotonically non-increasing, convex with respect to the componentwise order on $\mathbb{R}^n$ and the Loewner order on $\mathbb{R}^{m\times m}$ and

$$I^T \left(\mathcal{F}'(\gamma)\delta\right) J = -\int_\Gamma \delta u_\gamma^{(I)} u_\gamma^{(J)} \, \mathrm{d}x.$$

## 2 Main result

We formulate a sufficient criterion for a number of electrodes s.t. the considered inverse problem (**) is uniquely solvable. We also provide an equivalent convex reformulation and error estimates for noisy data.

For the resolution $\Gamma_1 \cup \dots \cup \Gamma_n$ we check if the model with fixed electrodes $\mathcal{E}_1, \dots, \mathcal{E}_m$ fulfills: If the directional derivatives possess at least one positive eigenvalue, i.e. if

**Criterion for reconstruction guarantee**

$$\mathcal{F}'(z_{j,k})\, d_j \not\preceq 0 \quad \text{for } j = 1, \dots, n \; k = 2, \dots, K$$

$z_{j,k} = \frac{a}{2} e'_j + \left(a + k\frac{a}{4(n-1)}\right) e_j \in \mathbb{R}^n_+$, $d_j = \frac{2b-a}{a}(n-1)e'_j - \frac{1}{2}e_j$
"$\preceq$"-Loewner-order, $K = \lceil \frac{4(n-1)b}{a} \rceil - 4n + 5$, $e'_j = (1, \dots, 1) - e_j$.

then the following holds:

(a) The inverse problem (**) is uniquely solvable and $\hat{\gamma}$ is the unique minimizer of the convex problem:

$$\texttt{minimize } \|\gamma_i\|_1 \text{ s.t. } \gamma \in [a,b]^n, \; \mathcal{F}(\gamma) \preceq \mathcal{F}(\hat{\gamma}).$$

(b) For $\hat{\gamma} \in [a,b]^n$, $\delta > 0$ and $Y^\delta \in \mathbb{R}^{m\times m}$ with $\|\mathcal{F}(\hat{\gamma}) - Y^\delta\|_2 \le \delta$ the convex problem:

$$\texttt{minimize } \|\gamma_i\|_1 \text{ s.t. } \gamma \in [a,b]^n, \; \mathcal{F}(\gamma) \preceq Y^\delta + \delta I$$

possesses a minimum, and every minimum $\gamma^\delta$ fulfills

$$\|\hat{\gamma} - \gamma^\delta\|_\infty \le \frac{2\delta(n-1)}{\lambda}$$

with $\lambda = \min_{j,k} \lambda_{\max}\left(\mathcal{F}'(z_{j,k}) d_k\right)$.

This result is an extension of [1] to an electrode model. Last we check the criterion in Table 1.

## References

[1] B Harrach *Solving an inverse elliptic coefficient problem by convex non-linear semidefinite programming*, Optim.Lett.16:1599–1609, 2022.

**Table 1:** Required number of electrodes for a partition of $\Gamma_1, \dots, \Gamma_n$ for $n = 2, \dots, 10$ (geometry as in Fig.1).

| Resolution size $n$ | 2 | 3 | 4 | 5 | 6 | 7 | 8 | 9 | 10 |
|---|---|---|---|---|---|---|---|---|---|
| Required electrodes $m$ | 3 | 6 | 8 | 10 | 13 | 16 | 18 | 21 | 24 |

# Separation of ventilation and cardiac related signals from thoracic EIT image streams using Empirical Mode Decomposition

Alfred Hülkenberg[1] and Steffen Leonhardt[1]

[1]Chair for Medical Information Technology, RWTH Aachen University, Aachen, Germany, huelkenberg@hia.rwth-aachen.de

**Abstract:** So far, there is no effective way to decompose an EIT image stream into physiological processes as a ventilation and cardiac-related signal. Here the potential of the heuristic Complete Ensemble Empirical Mode Decomposition with Adaptive Noise (CEEMDAN) approach was analysed for source separation.

## 1 Introduction

Electrical Impedance Tomography (EIT) a radiation-free, non-invasive application, applied at the bedside for monitoring spontaneous and artificial ventilation [1, 2]. Considering a *column index* $x$ and a *row index* $y$ within $1 \leq \ldots \leq 32$ over *time* $t$, the corresponding *temporal EIT signal* $Z_{x,y}(t)$ captures variations of bioimpedance [1]. As Fig. 1 suggests, $Z_{x,y}(t)$ is interpretable as a superposition of at least one *steady state component* $Z^{DC}_{x,y}(t)$, *ventilation-related signal* $Z^{VS}_{x,y}(t)$, *cardiac-related signal* $Z^{CS}_{x,y}(t)$ and a disturbing *noise-related signal* $Z^{NS}_{x,y}(t)$

$$Z_{x,y}(t) = Z^{DC}_{x,y}(t) + Z^{VS}_{x,y}(t) + Z^{CS}_{x,y}(t) + Z^{NS}_{x,y}(t)\ . \quad (1)$$

A separation of these is of clinical interest, but a feasible approach to do so is still missing. Typical approaches often rely on non-physiological conditions (i.e. apnoea) [2] or neglect conditions as the requirement of linearity or stationarity of the processed signal (i.e. filtering) [3].

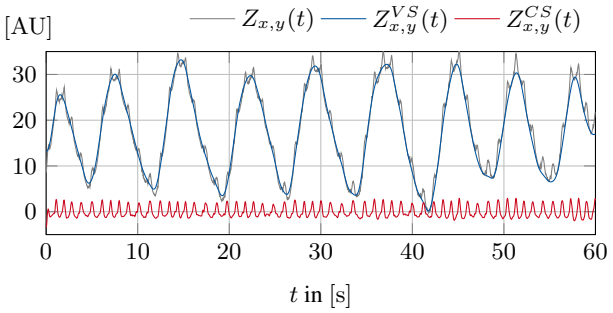


**Figure 1:** EIT signal acquired near the heart region at $(x, y) = (18, 7)$. The orginal signal $Z_{x,y}(t)$ is shown in gray, the ventilation $Z^{VS}_{x,y}(t)$ in blue and cardiac activity $Z^{CS}_{x,y}(t)$ in red.

## 2 Methods

The heuristic CEEMDAN approach [4] was applied, which is designed for processing of non-linear, non-stationary data. It separates a signal into a finite number $I-1$ of *Intrinsic Mode Functions* $\mathrm{IMF}_i(t)$ varying in amplitude and frequencies, plus a residuum $r_I(t)$ (signal trend)

$$s(t) = \sum_{i=1}^{I-1} IMF_i(t) + r_I(t). \quad (2)$$

To prevent mode-mixing, CEEMDANs dynamic filter bank property was enbaled, by addition of multiple versions of random noise $n^j(t)$, averaging of the whitend signals [5]

$$\mathrm{IMF}_i(t) = \frac{1}{J}\sum_{j=1}^{J} \widetilde{\mathrm{IMF}}^j_i(t), \widetilde{\mathrm{IMF}}^j_i(t) = s(t) + n^j(t)\ . \quad (3)$$

Based on their maximal amplitude in f-domain the resulting $\mathrm{IMF}_i(t)$ were assigned to physiological bandwidths, here $f_{DC} \leq 1$ Hz $< f_{VS} \leq 20$ Hz $< f_{CS} \leq 200 < f_{NS}$.

The CEEMDAN implementation provided by [4] was used to analyse the data acquired from 9 healthy male test subjects sitting upright in a chair. EIT was acquired using a Pulmovista 500 (Dräger, Lübeck, Germany) and a reference PPG was monitored using a SOMNOLab2 (Weinmann, Hamburg, Germany).

## 3 Discussion and Conclusions

The signal in Fig. 1 reveals a fair separation of $Z^{VS}_{x,y}(t)$ and $Z^{CS}_{x,y}(t)$, establishing periodically occurring processes with a similar shape. Complementary in the frequency domain the corresponding spectra are dominant within their respective bandwidth, see the amplitude values in Fig. 2 within range of $f_{VS}, f_{CS}, f_{NS}$. Besides, after a synchronization of $Z^{CS}_{x,y}(t)$ and PPG the beat-to-beat time shows a feasible correlation of 0.905 during linear regression analysis.

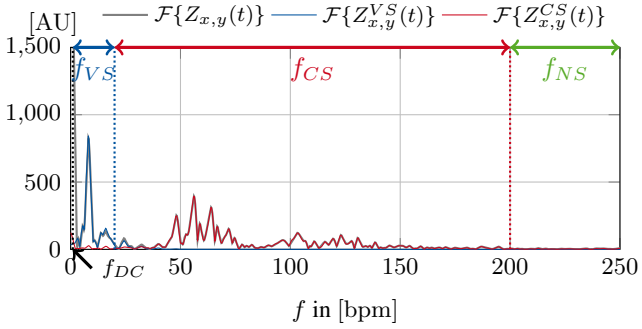


**Figure 2:** Comparison of the spectra of the signal in Fig. 1.

In the future, a real time impelmentation of CEEMDAN may enable a continuous and simultaneous tracking of both breathing and heart activity.

## References

[1] I. Frerichs, M. B. P. Amato, A. H. van Kaam, D. G. Tingay, Z. Zhao, B. Grychtol, M. Bodenstein, H. Gagnon, S. H. Böhm, E. Teschner, O. Stenqvist, T. Mauri, V. Torsani, L. Camporota, A. Schibler, G. K. Wolf, D. Gommers, S. Leonhardt, A. Adler, and TREND study group. *Thorax*, 72:83–93, 2017; doi: 10.1109/LSP.2003.821662

[2] S. Leonhardt and B. Lachmann. *Intensive Care Med* 38:1917–1929, 2012; doi: 10.1007/s00134-012-2684-z

[3] N. E. Huang, Z. Shen, S. R. Long, M. C. Wu, H. H. Shih, Q. Zheng, N.-C. Yen, C. C. Tung, and H. H. Liu. *Proc. R. Soc. Lond. A.*, 454:903–995, 1998; doi: 10.1098/rspa.1998.0193

[4] M. A. Colominas, G. Schlotthauer, and M. E. Torres. *Biomed Signal Process Control*, 14:19-29, 2014; doi: 10.1016/j.bspc.2014.06.009

[5] P. Flandrin, G. Rilling, and P. Goncalves. *IEEE Signal Processing Letters*, 11:112–114; doi: 10.1109/LSP.2003.821662

# Machine learning based breast cancer classification algorithm in an Electrical Impedance Tomography set up

Jöran Rixen[1], Nico Blass[1], Steffen Leonhardt[1]

[1]Chair for Medical Information Technology, RWTH Aachen University, Aachen, Germany, rixen@hia.rwth-aachen.de

**Abstract:** Breast cancer is the major cause of cancer related death among women. Due to pain of mammography, patients often avoid screening. A potential alternative is electrical impedance tomography. However, its low resolution can prevent robust diagnostics. In this work, we conduct a simulation study and train a Support Vector Machine for distinguishing between cancerous and non-cancerous breasts.

## 1 Introduction

With 2.3 million cases worldwide and 0.68 million deaths in 2022, breast cancer is the leading cause of death from cancer among women [1]. Early detection of breast cancer can increase the relative 5-year survival rate significantly. When the cancer has not yet spread, 99 % of patients survive. While this figure drops to 20 % when, the cancer has begun to spread in the body [2]. Thus, early detection of breast cancer is of great importance. X-Ray mammography is an established technique for breast cancer screening. The need for breast compression, however, makes patients hesitant to use it. AS cancer has a higher conductivity compared to the surrounding breast tissue, electrical impedance tomography (EIT) might help in detection of breast cancer. However, as EIT is known for its low spatial resolution, which is made even worse by the fact that time difference EIT is not applicable in this case, an additional classification based on the voltages can help in diagnosing breast cancer. We, thus, analyze the performance of a support vector machine (SVM) for analysis of breast cancer in an time-independed set up.

## 2 Methods

We created an FEM model in a cuboid shape. This represents a breast that is fixed in between two plates with electrodes. The shape resembles the setup of mammography, but less pressure is required. Another advantage is the fixed position of the electrodes. On two sides of the cuboid 15 electrodes are placed. The whole set up can be seen in Figure 1.

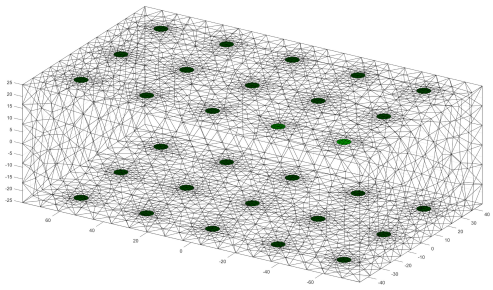

**Figure 1:** FEM model on which the simulations were performed.

Each 5 opposite electrodes planes were stimulated using the adjacent-adjacent pattern, thus there are 3 electrode planes. All, but one face were covered with 2 mm of skin, inside the middle glandular (form of a truncated cone) tissue was placed, inside it glandular lobes were placed. Tumors were randomly placed inside the domain. All mesh elements with no tissue type were set to fatty tissue. For the generation of training data, all placed elements were randomly shuffled, 7500 different realizations of the model were created, thus the position of the lobes, tumors, and gland structures are varying. 50 % of all models did not contain any tumor.

We used an SVM to classify the samples into either tumor or non-tumor breast. An SVM maps the data into a high dimensional space, and tries to fit a hyper-plane to separate the two classes. For evaluation of the model we used the F1-Score, which is the harmonic mean of the precision and recall and, thus, allows for the evaluation of both the tumor and non-tumor labels.

### 2.1 Results

The smaller tumor sizes have a lower F1-Score, which means that the SVM cannot separate the two cases as accurately. The bigger the tumor radius $r$, the higher the F1-Score. When the SNR of the voltages drop very low, the F1-Score decreases for all tumor radii.

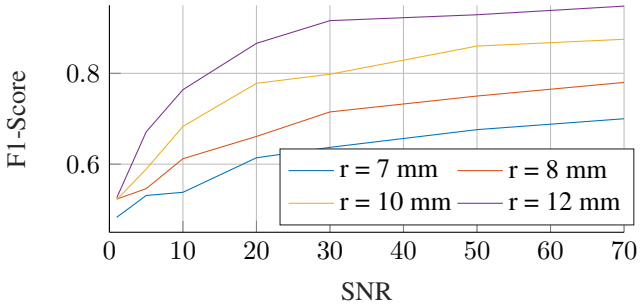


**Figure 2:** F1-Scores of the simulated cases.

## 3 Conclusions

The SVM is able to provide reliable estimations on the presence of breast cancer even under noisy conditions, which were included during training. However, this needs to be validated through an experiment.

## 4 Acknowledgements

The authors thank the project InDiThera (13GW0361E) through the Federal Ministry of Education and Research for their financial support.

## References

[1] https://www.iarc.who.int/cancer-type/breast-cancer/
[2] https://www.cancer.org/cancer/breast-cancer/understanding-a-breast-cancer-diagnosis/breast-cancer-survival-rates.html

## Session 5: Hardware

# Wearable EIT Systems with Central Powering

Josias Wacker[1], Michaël Rapin[1], Fabian Braun[1], Olivier Chételat[1]

[1]Centre Suisse d'Electronique et de Microtechnique, Bern, Switzerland, jwr@csem.ch

**Abstract:** We present two fully wearable EIT instruments with novel electronics. The first one was realized with discrete off-the-shelf components, the second one with an application-specific integrated circuit. The devices provide high EIT signal quality and wearing comfort, as shown in a clinical study.

## 1 Introduction

EIT has been shown to be a valuable tool in cardiorespiratory monitoring [1]. Most EIT instruments presented so far are bed-side monitors, not allowing ambulatory or remote recording of pulmonary functions. One of the main challenges in making an EIT wearable is to reduce the cabling complexity and to reduce the size of the bioimpedance sensors. Here, we introduce bioimpedance sensing wearables with minimal cabling complexity and small sensors. The first EIT wearable presented in the following is realized with discrete electronics components, the second one with an application-specific integrated circuit (ASIC).

## 2 Methods

### 2.1 Functional Vest with Discrete Components

Figure 1 shows photos of a mannequin wearing the so-called WELMO vest made with discrete electronics components. The main components of the vest are:

- a removable master on the outside of the vest,
- 18 sensors on the inside of the vest,
- the vest textile,
- 2 wires connecting all sensors and the master (not visible in Figure 1).

The master concentrates the data measured by the sensors and transfers it via Bluetooth to a mobile device, and coordinates and powers the sensors. The master also contains an accelerometer for measuring the wearer's physical activity and body position. As shown in Figure 1, sixteen sensors are placed equidistantly around the thorax on one transverse plane at the level of the apex of the sternum and measure bioimpedances. Four of these sensors additionally record chest sounds. Two additional sensors which only measure chest sounds are placed below the clavicles. All sensors are integrated in a tightly fitting vest which assures a firm contact between the sensors and the skin. The vest has a zipper on the front for easy donning and doffing. The two wires connecting the sensors and the master are integrated between the two textile layers of the vest. One of the ground-breaking achievements of the WELMO sensing technology is that it sends and measures delicate signals of differing magnitudes through the same two unshielded wires. These signals are powering, sensor synchronization, and bioimpedances (requiring a very stable reference potential). This 2-wire bus is a further development of CSEM's cooperative sensor technology [2]. The high EIT signal quality and wearing comfort of this system have been demonstrated in a clinical study [3].

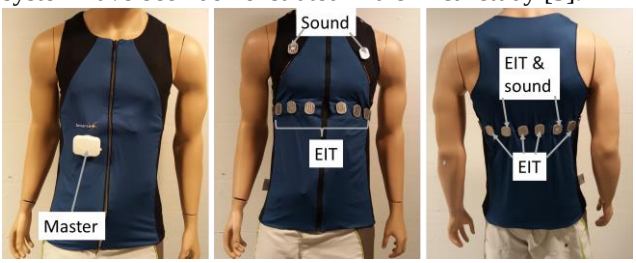


**Figure 1:** WELMO vest with discrete electronics components. Left: Vest worn outside-out, front view. Middle: Vest worn inside-out, front view. Right: Vest worn inside-out, back view.

### 2.2 Demonstrator with ASIC

**Figure 2** shows a demonstrator of the WELMO wearable made with an ASIC. This wearable is realized as a harness. It benefits from the same advantages as the vest, described above. Thanks to the integration of the electronics in a chip of 1.8 × 2.2 mm$^2$ the volume of the sensors was reduced to the size of clothing buttons. The wearing comfort was further improved by integrating the main part of the sensors in the textile. In addition, the ASIC consumes about 20 times less energy than the discrete component sensor, thus allowing to reduce the size of the battery in the master.

**Figure 2:** WELMO vest with ASICs.

## 3 Conclusions

This paper presented two novel EIT instruments. As opposed to most other EIT devices, the WELMO vest and harness are fully wearable. This is made possible thanks to: (1) the small volume of the sensors which is achieved by remote powering of the sensors and by integrating the sensor electronics in an ASIC, and (2) the simple connection of the sensors in a two-wire bus.

## 4 Acknowledgements

This work was funded by the European Union (Grant No. 825572).

## References

[1] I Frerichs *et al.* Thorax, 72:83-93,2017
[2] M Rapin, F Braun, A Adler, J Wacker, I Frerichs, B Vogt, O Chételat IEEE Trans Biomed Eng, 66(3):810-820,2019
[3] I Frerichs *et al. Conf EIT 2023,* Aachen, Germany, June 2023

# Peripheral vein scanner using Electrical Impedance Tomography

Miguel-Ángel San-Pablo-Juárez[1] and Dulce-María Orozco-Corona[2]

[1]Institute of Physics, Benemérita Universidad Autónoma de Puebla (BUAP), Mexico. miguel.sanpablo@ieee.org
[1]School of Engineering, Universidad de las Américas Puebla (UDLAP), Mexico.
[2]Automation and Information Technologies Department, Universidad Tecnológica de Querétaro, Mexico.

**Abstract:** In this work is proposed the design of a scanner using EIT for finding the location of veins inside the arm, this scanner is intended to help reducing the pain due to complications when searching the vein to make a venipuncture. The hardware design and some simulations of spatial location of a vein using the scanner are shown.

## 1 Introduction

About 14 million of venipunctures around the world are not performed successfully on the first attempt each year causing discomfort and pain in a patient [1]. An apparatus to find the veins location inside the arm may help to reduce errors making a venipuncture on the first attempt, especially in children, reducing the pain levels and performance of venipunctures.

Many factors as obesity, small diameter of the veins, poorly contoured veins, abnormal location, and the skill of the person performing the extraction of blood, make venipuncture difficult [1]. There are infrared devices to find the location of the veins [2] but the main disadvantage is the poor contrast and the infrared noise; in the other hand, there exist ultrasonic detectors too [3], the last method offers a good quality of image but is relatively expensive. Electrical impedance is another technique to locate veins [1] but in the first studies it needs to apply a contrast agent because the measurement does not offer good contrast and this measurement is done only in one dimension. Recently the technique of Electrical Impedance Tomography (EIT) was used to develop a method for detecting veins with high contrast in the surface of the arm skin [4] and EIT measures over all directions where the electrical current is applied.

In his work a scanner for finding the location of veins and tell where to do a venipuncture is simulated.

## 2 Methods

This work uses a straight array of 8 electrodes placed over the arm skin with a surface configuration for making the tomography as is shown in Figure 1a. The number of electrodes is due to the reduced space of the arm. Once the EIT was obtained, results are displayed in a squared screen as is shown in Figure 1b. The resolution is 32x32 pixels, but it has high contrast, useful to see a vein up to 2 mm in diameter at least in simulation. Potentials between electrodes are obtained using a simple EIT single source hardware that uses the synchronous demodulation method at 10 kHz. Image reconstruction was done using EIDORS software [5] with a straight spatial distribution of 8 electrodes of Ag/AgCl.

A difference solver was used to get the EIT image, the forward model was based on a geophysical 2D model of EIDORS software.

A high contrast image of the location of the vein is obtained.

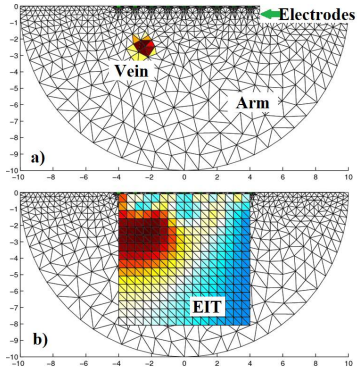


**Figure 1:** Location of the vein in a square screen using EIT.

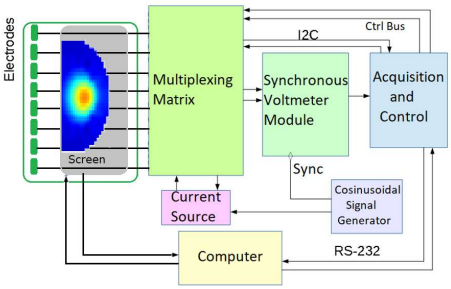


**Figure 2:** Module diagram of the built EIT measuring instrument.

Figure 2 shows the block diagram of the designed hardware. The location of the vein may be displayed directly over the arm with a mirrored screen with the EIT of the arm inside. Both simulation and hardware work fine separately. In future work the scanner will be implemented.

## 3 Conclusions

This work has a design that can detect peripheral veins up to 2 mm of diameter. This scanner works fine at the simulation level.

## 4 Acknowledgements

Thanks to CONACyT for supporting the project 286633 of Ciencia Básica CB-2016 and the postdoctoral scholarship I1200/224/2021.

## References

[1] MB Al-Harosh, SI Shchukin *J. Electr. Bioimp*, *8*: 79-83, 2017.
[2] CT Pan, MD Francisco, CK Yen, SY Wang, YL Shiue. *Sensors 19*, 2019.
[3] G Maiocco, C Coole C, *J Nurs Care Qual.* 27(1):51-5, 2012.
[4] San-Pablo-Juarez MA, Orozco-Corona DM *J. Phys.: Conf. Ser. 2008, 4th LACBIO* 2021.
[5] A Adler, WR Lionhearth, *PhysiolMeas*, 27(5):S25-42,2006.

# Evaluating high-channel electrical impedance tomography

Barry Belmont[1], Simon Ghionea[1], Anjali Sehrawat[1], and Matthew D Keller[1]

[1]Global Health Labs, Inc, Bellevue, Washington, United States of America, barry.belmont@ghlabs.org

**Abstract:** For electrical impedance tomography to become an effective non-invasive anatomical imaging modality, more electrodes are needed than are currently used in clinical practice. The accuracy of image reconstruction using a 256-channel system is herein demonstrated.

## 1 Introduction

Electrical impedance tomography (EIT) determines a volumetric conductivity distribution of a material by measuring surface potentials elicited by injected current and solving an ill-posed, ill-conditioned inverse problem to resolve internal passive electrical properties. Due to the nature of the inverse problem, spatial resolution of the reconstructed conductivity distribution is a function of the material being measured (e.g., its composition, its structure) and the number of electrodes used. Current clinically deployed EIT systems use 16- or 32-electrodes to image a local region of a patient. Most systems deploy 'functional imaging' to monitor physiological conditions, such as pulmonary perfusion or cardiac output, rather than 'anatomical imaging' in which the structure of tissues or organs is assessed. This is due in large part to the resolving limitations of small numbers of electrodes.

To date, few EIT systems have been constructed with over 100 electrodes. In the late 1970s, Henderson and Webster [1] constructed an 'impedance camera' using 144 electrodes to obtain 100 spatially specific measurements of a human thorax with the intent of monitoring pulmonary oedema. More recently, Xu et al. [2] created a 128-electrode system with 64 driving electrodes and 64 measuring electrodes to evaluate the feasibility of higher-resolution three-dimensional (3D) imaging.

To validate the anatomical imaging capabilities of high-channel EIT, herein we demonstrate 3D reconstruction using a 256-channel system.

## 2 Methods

A cylindrical tank was made from acrylic (inner diameter of 11.5", height of 17") and filled with a saline (deionized water (>18 MΩ-cm) mixed with 0.15 wt% NaCl) of known conductivity (0.3 S/m) to simulate bulk human thorax. A sphere (3" dia.) was created by fused deposition modelling (100% in-fill, LulzBot Mini) of a composite conductive polymer (Protopasta, 2.85 mm dia.) with a measured conductivity of 4.17 ± 0.92 S/m. The sphere was fitted to a positioning mechanism comprising a threaded polymer rod with top and bottom wingnuts that connected to a top lid, allowing for precise x-, y-, and z-placement within the tank and rotational orientation along the axis of the polymer rod.

Electrodes made of stainless steel (18/8, ISO 7380) button socket head cap screws (diameter of 4 mm, length of 10 mm) coupled to stainless steel (18/8, ASTM A582) standoffs (8 mm, hex, length of 14 mm) were embedded equidistant from one another (1.13") along the circumference of the tank in eight rings of 32 electrodes each for a total of 256 electrodes.

The electrodes were connected via their standoffs to a distal end of shielded cables through male banana plugs (4 mm dia.). The proximal end of the cables terminated in a Mini Delta Ribbon connector (MDR40), which in turn connected to an adapter to interface with an EIT system by way of a Mini Edge Card socket (MEC1-130).

The EIT system used was a custom-built 256-channel system designed and produced by Sciospec Scientific Instruments GmbH (Bennewitz, Germany). The system utilizes a pseudo differential current source for single sine excitation that may be connected across any two channels, while potential is measured simultaneously on all channels.

As an initial assessment of the system, a subset of 224 electrodes (seven rings of 32 electrodes each) on the tank were used to stimulate (1 mA at 50 kHz in a skip0 pattern) and measure from to resolve the sphere in a known location. The experimental setup and an example of its EIT reconstruction (Gauss Newton solver with NOSER prior, EIDORS v3.11) are shown in Figure 1.

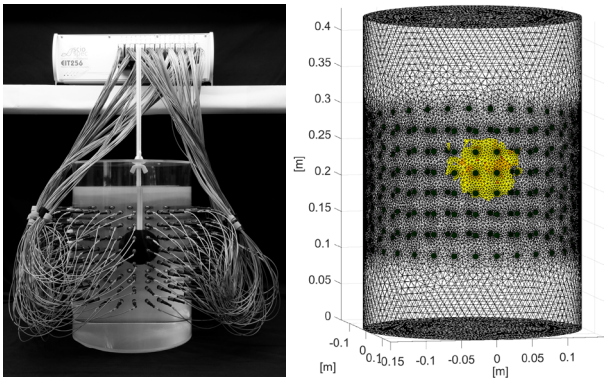


**Figure 1:** Experimental setup and reconstruction of the sphere.

## 3 Conclusions

As hardware and algorithms continue to progress, next generation EIT systems will increase spatial resolution and improve clinical analysis of patient physiology and anatomy. High-channel, 3D EIT holds immense promise as most gross anatomical imaging systems, such as x-ray computed tomography and magnetic resonance imaging, are unavailable to certain patient populations during periods of treatment, such as neonates and their mothers during the intrapartum period of pregnancy, while many point-of-care systems, such as ultrasound or tocodynamometry, are unable to evaluate the entirety of relevant anatomy or physiological processes. Healthcare settings in low- and middle-income countries could especially benefit.

Having demonstrated high-channel EIT acquisition under laboratory conditions, our future development of this next generation system includes more complex phantom models and, ultimately, clinical evaluation.

## References

[1] RP Henderson, JG Webster *IEEE Trans on BME.* 3:250-254, 1978.
[2] G. Xu et al., *29th Int Conf of the IEEE EMBS*, p. 4386-4389, 2007.

# Development of a Wide-bandwidth FPGA-based EIT System with Multitone Implementation for Medical Imaging in Space

Kendall Farnham[1] and Ryan Halter[1,2]

[1]Thayer School of Engineering, [2]Geisel School of Medicine, Dartmouth College, Hanover, NH USA,
kendall.farnham@dartmouth.edu

**Abstract:** We are developing a multi-use, space-compliant EIT data acquisition system (DAQ) to be integrated with state-of-the-art ultrasound for enhancing medical imaging in space. Integrating the small form factor EIT DAQ with ultrasound will provide a low-cost imaging system that can produce high contrast, high resolution images, ultimately enabling astronauts to independently monitor health without the need for telemedical support.

## 1 Introduction

Ultrasound is the current imaging system used on the International Space Station, but this complex technique requires telemedical support for guiding acquisition and diagnosis, limiting its standalone effectiveness to near-Earth missions [1]. One method to improve ultrasound image readability is to increase the contrast at injury sites with electrical impedance tomography (EIT), as impedance is sensitive to cellular content, blood flow, tissue type, and tissue injury, all of which are relevant for monitoring physiological effects of the space environment (e.g., tissue injury, muscle atrophy, thoracic function, cancer presence) [2]. Critical design features of a space deployable EIT system include small form factor (low mass/volume), low power, multi-use, compatible with spacecraft systems, and able to meet NASA EMI/EMC requirements and Technical Standards. Additionally, the system should have high SNR (>80 dB) to ensure accurate EIT reconstruction and high-speed acquisition (>30 fps) to capture fast moving processes like blood flow and provide real-time feedback while imaging. We are developing a wide bandwidth (100 Hz to 1 MHz), multitone, FPGA-based EIT data acquisition system (DAQ) to be integrated with ultrasound for more intuitive acquisition and interpretation by a non-specialist. The FPGA provides low-cost design flexibility and a low-power, high-speed platform for the DAQ. The multitone implementation allows for high-speed spectroscopic acquisition, and the wide bandwidth provides sensitivity for a range of medical conditions applicable to long duration and deep space travel. Ultimately, we aim to provide a low cost, low resource, integrated ultrasound and EIT (US-EIT) system that can accurately characterize internal injury (e.g., detect internal bleeding that needs immediate intervention) while meeting spacecraft constraints, enabling autonomous medical care for deep space missions.

## 2 Methods

A wide bandwidth, 64-channel DAQ with a multitone voltage source and semi-parallel voltage measurement scheme is being designed on an Artix-7 FPGA (Xilinx, San Jose, CA, USA) for the space-deployable EIT system. A custom analog front end (AFE) has been designed to stack on top of a Trenz Electronics (TE0703/TE0711) FPGA carrier board for a compact (5x6x10 cm), low noise implementation (Figure 1). The AFE includes power conversion from a medically compliant power supply (IEC 60601-1), a voltage source circuit with current sensing, two voltage measurement channels, and multiplexers for switching functionality (source, sink, measure) of the 64 electrodes. A multitone direct digital synthesis (DDS) signal generated on the FPGA is converted to the analog domain via a 14-bit, 125 MSPS digital-to-analog converter (DAC) (THS5671A), and three 16-bit, 15 MSPS analog-to-digital converters (ADCs) (LTC2387-16) are used for converting sensed current and measured voltages back to the digital domain for demodulation. VHDL code is being developed in Vivado 2018.2.2 (Xilinx) for synchronous control of the DAQ modules, and a MATLAB user interface allows control of frequency and channel selection.

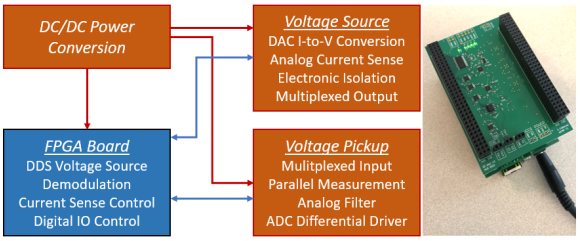


**Figure 1.** Left) block diagram of EIT DAQ functionality, where analog modules are in orange and digital functions in blue. Right) the AFE stacks on top of the FPGA carrier via 96-pin connectors for a small form factor implementation (size 5x6x10 cm).

Benchtop tests are in progress to assess DAQ performance and ensure requirements are met. Once completed, the DAQ will be integrated with the GE Vivid E95 ultrasound system to validate US-EIT for enhanced image acquisition and readability.

## 3 Conclusions

A wideband FPGA-based EIT DAQ with a multitone source and 64-channel interface will provide a low cost, low resource imaging system that can monitor a wide range of medical conditions associated with long-duration space travel. Integrating the DAQ with ultrasound will improve image readability and enable astronauts to self-monitor and diagnose injury when isolated in deep space.

## 4 Acknowledgements

This work was supported by a NASA Space Technology Graduate Research Fellowship.

## References

[1] Antonsen, E et al, *NASA HRP Evidence Report*, 5-79, 2017
[2] Paulsen K et al, *Radiation Research*, 152(1), 41-50, 1999

# Preliminary Human-Subject Results of ACT5 EIT System

Omid Rajabi Shishvan[1], Nilton Barbosa da Rosa Junior[2], Gary J. Saulnier[1], Jennifer Mueller[2,3], Jonathan C. Newell[4], David Isaacson[5]

[1]Department of Electrical & Computer Engineering, University at Albany - SUNY, NY, USA, orajabishishvan@albany.edu
[2]School of Biomedical Engineering, Colorado State University
[3]Department of Mathematics, Colorado State University
[4]Department of Biomedical Engineering, Rensselaer Polytechnic Institute
[5]Mathematical Sciences, Rensselaer Polytechnic Institute

**Abstract:** Initial human-subject results from the ACT5 EIT system are presented. The results include images showing pulsatile perfusion at a sequence of time snapshots in the cardiac cycle in addition to electrocardiogram (ECG) measurements collected simultaneously from multiple electrodes.

## 1 Introduction

The ACT5 EIT is a multiple-source applied-current EIT system that has recently been developed and is in use in the hospital environment for imaging the lung performance of cystic fibrosis patients. The deployed ACT5 system has 32 electrodes, with each electrode equipped with a current source and a voltmeter. This makes it possible to use a fewer number of electrodes in cases where attaching all 32 electrodes to the patient is not possible. Maximum amplitude of the applied current from one electrode is 350 µA and the frequency of the applied currents is set at 99.6 kHz. ACT5 collects data at a rate of 27 frames/sec and the frame rate can be doubled to 54 frames/sec when 16 or fewer electrodes are used. Each electrode in the ACT5 system collects ECG data simultaneous with the EIT data with a sampling frequency of 864 Hz [1]. Recording ECG signals from all electrodes in parallel with EIT imaging provides the opportunity to use ACT5 data to solve the inverse ECG problem.

## 2 Methods & Results

Data was collected from a healthy adult subject. The electrode configuration is set as two rings of 16 electrodes around the thorax region to provide a 3D image as shown in Fig. 1. Data was collected with the subject in the supine position during breath holding. Images were reconstructed using the ToDLeR algorithm [2].

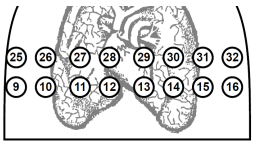


**Figure 1:** Electrode placement on subject (front view).

The reconstructed images of four stages in the cardiac cycle are shown in Fig. 2, which are displayed in DICOM orientation. The stages include the beginning of the P wave (top left), end of diastole (top right), beginning of T wave (bottom left), and end of systole (bottom right).

The ECG measurements from eight electrodes are shown in Fig. 3. The ECG measurements are referenced to common voltage and filtered for 60 kHz and harmonics of the frame rate frequency.

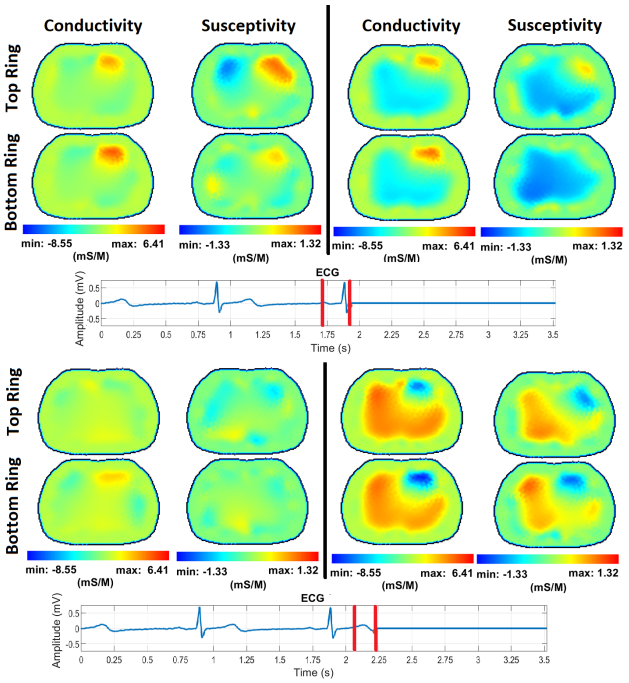


**Figure 2:** Reconstruction of four stages in the cardiac cycle.

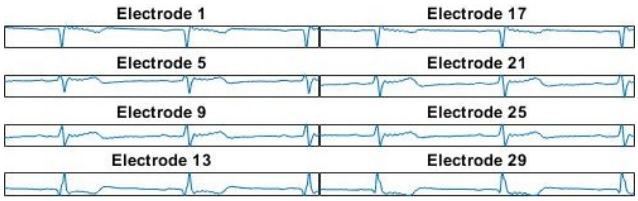


**Figure 3:** ECG signal recordings on 8 select electrodes.

## 3 Conclusions

This demonstrates the ability of ACT5 to simultaneously measure EIT data and ECG data from each of its 32 electrodes while making impedance images during the cardiac cycle. These impedance images show the 4 distinct phases of conductivity distributed withing the chest in synchrony with the 4 moments of the cardiac cycle indicated on the ECGs.

## 4 Acknowledgements

This project was supported by Award Number 5R01EB026710 from the National Institute Of Biomedical Imaging And Bioengineering. The content is solely the responsibility of the authors and does not necessarily represent the official view of the National Institute Of Biomedical Imaging And Bioengineering or the National Institutes of Health.

Human data collection is in accordance with the amended Declaration of Helsinki–Ethical Principles for Medical Research Involving Human Subjects under the approval of the Colorado State University Institutional Review Board (approval number 2943) with informed written consent.

## References

[1] A Abdelwahab, O Rajabi Shishvan, GJ Saulnier *Conf 14th ICBEM & 18th ICBEI & 22nd EIT*, p.208–211, Seoul, South Korea, Jun 2022

[2] RS Blue, D Isaacson, JC Newell *Physiol Meas*, 21:15–26, 2000

# Development of multifrequency device for bioimpedance measurements

Alberto Battistel[1], Hegoa Craamer Lizarraga[2], Maite Termenon[2], Knut Möller[1]

[1]Institute of Technical Medicine (ITeM), Furtwangen University, Jakob-Kienzle-Strasse 17, 78054 Villingen-Schwenningen, Germany
[2]Biomedical Engineering Department, Faculty of Engineering, Mondragon Unibertsitatea (MU-ENG), Loramendi, 4; 20500 Mondragón, Spain.

**Abstract:** Bioimpedance measurements are usually performed on cell cultures, tissues, and human body, measuring sequentially the impedance at different frequencies. However, when stationary conditions are violated these measurements are not consistent. Here we develop a custom device based on an multifrequency approach.

## 1 Introduction

Bioimpedance is measured through the injection of small alternating currents into tissues or human body. For safety concern these currents are limited by the IEC 60601 standard to the milliampere or sub-milliampere range [1].

The measurements can be performed with either two or four electrodes, where the latter is usually preferred. On the other side, the impedance is usually measured sequentially at different frequencies. However, if the bioimpedance changes even slightly with time, the measurement is no longer consistent and different approaches are necessary to validate the quantities measured.

The multifrequency approach overcomes this problem. In fact, all the frequencies of interest are injected simultaneously through a broadband signal. Such approach is developed here in a custom device whose functional schematic is depicted in Fig. 1, where the operational amplifier OPAMP1 functions as voltage controlled current source converting an arbitrary waveform at $v_{in}$ into the current $i$. The magnitude of this current is set by the size of the sensing resistor $R$. The impedance to determine is depicted by $Z$ while the four $Z_{cont.}$ represent the contact impedances of the four electrodes and are usually unknown. Two of these electrodes are connected directly to an instrumentation amplifier (INA1) which measures the ohmic drop across $Z$. The other two electrodes carry the current $i$ through the system. A second instrumentation amplifier (INA2) measures the ohmic drop across $R$ which is proportional to the injected current $i$.

A Field-Programmable-Gate-Array (FPGA) –powered device provides the digital-to-analog and the analog-to-digital conversion for $v_{in}$, $v_{Ch1}$, and $v_{Ch2}$, together with the power rails to feed the circuit (not showed).

## 2 Methods

An LMC6001 and two INA128P were used for OPAMP1 and INA1–2, respectively and several resistor values were tested for the sensing resistor $R$. The broadband multifrequency signal was a multisine comprising 19 sinusoidal waves with equal amplitude and frequencies distributed quasi-logarithmically between $0.5\,\mathrm{kHz}$ and $400\,\mathrm{kHz}$. The acquisition was performed at $1\,\mathrm{MHz}$ with the Analog Discover 2 from Digilent controlled using the library `pydwf`. The performances of the device were characterized with several passive elements to substitute $Z$ and $Z_{cont.}$.

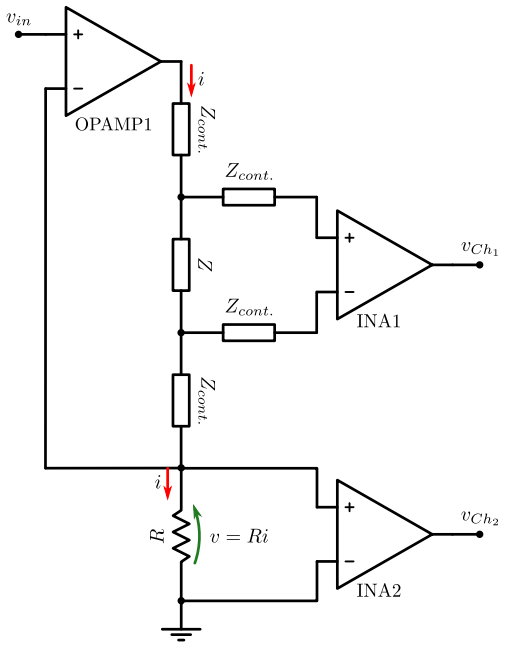


**Figure 1:** Functional schematic of the custom bioimpedance device. $Z$ represents the impedance to measure.

## 3 Results

The system performs well up to a sampling rate of $1\,\mathrm{MHz}$. However for accurate measurements a calibration is required well below that value. In fact, at frequencies higher than $100\,\mathrm{kHz}$, the measurements depart from ideality and a inductive behavior is observed. This is characterized by an extra apparent $R \parallel L$ component in series with the measured impedance.

Calibrated measurements give an error in the range of $0.01\,\%$ at the lowest frequencies and of $0.07\,\%$ at the highest. On the other hand, the maximum phase error is $0.02°$ at $400\,\mathrm{kHz}$.

## 4 Conclusions

We successfully developed and characterized a custom device for bioimpedance measurements in four electrodes configuration. This device is capable of accurate measurements employing a broadband multisine with frequencies between $0.5\,\mathrm{kHz}$ and $400\,\mathrm{kHz}$.

## 5 Acknowledgments

This research was partially funded by the Deutsche Forschungsgemeinschaft (DFG) project TAP (project number 498224366) and the project AIRLobe (32-7545.220/42/1).

## References

[1] D Naranjo-Hernández, J Reina-Tosina, M Min *J. Sensors*, 2019: Article ID 9210258, 2019

# Towards intraoperative surgical margin assessment: Validation of an electrical impedance-based probe with ex vivo bovine tissue

Allaire Doussan[1], Ethan Murphy[1], and Ryan Halter[1]

[1]Thayer School of Engineering, Dartmouth College, Hanover, NH, USA, allaire.f.doussan.th@dartmouth.edu

**Abstract:** This work characterizes an impedance sensing surgical margin assessment (SMA) probe for us in radical prostatectomies. 3D electrical impedance tomography (EIT) reconstructions were generated from ex vivo bovine tissue. Experimental AUCs ≥0.82 differentiating adipose and muscle tissue were maintained up to 50 kHz.

## 1 Introduction

Prostate cancer is the 2nd most common cancer in the United States (US). In 2019, there were 224,730 new diagnoses of prostate cancer in the US and 1.4 million new cases globally [1,2]. Of these patients, at least one third are expected to undergo radical prostatectomy (RP) [3]. The primary goal of a RP is to remove the entire tumor and avoid positive surgical margins (PSM). However, there is a delicate balance between removing excess tissue to ensure wide margins for cancer eradication and sparing neurovascular tissue and maintaining maximal urethral length to preserve erectile function and continence. This results in a high PSM rate for RP ranging from 4-48% (average: 21%) [4-7]. This work focuses on characterizing a novel electrode array designed for EIT-based margin assessment in RP through simulations and ex vivo bovine tissue recordings.

## 2 Methods

### 2.1 Ex vivo bovine data collection

Impedance data was recorded from eleven separate locations on ex vivo bovine tissue with the custom SMA probe (Fig 1A). A 1 mA injection current was used across 41 log-spaced frequencies from 100 Hz to 1 MHz (EIT32, Sciospec Scientific Instruments GmbH, Bennewitz, Germany). Homogenous muscle, homogenous adipose, and heterogenous muscle/adipose tissue regions were probed to determine the accuracy of tissue identification and classification using EIT.

### 2.2 Registration and Segmentation

A photograph of each tissue location was captured with and without the probe in place. A semi-automatic scheme was developed in Matlab to register the probe location and orientation on the tissue to the Finite Element Method (FEM) mesh used for image reconstruction (Fig 1C). Each sample image is then segmented to delineate adipose and muscle tissues (Fig 1D). A binary map of the ground truth is created from the segmented image for each probed location on the coarse grid used for EIT reconstruction (Fig 1E, adipose is blue and muscle is yellow). Experimental AUCs were calculated by comparing EIT reconstructions with the ground truth binary map.

## 3 Conclusions

AUCs ≥0.82 differentiating adipose and muscle tissue in EIT images were maintained up to 50 kHz (Fig 1F shows one sample's reconstructions that correspond to Fig. 1E). This paper demonstrates the ability of the designed impedance sensing SMA probe to classify tissue types in an ex vivo bovine model of muscle and adipose tissue. Ongoing work focuses on increasing the bandwidth of the probe by implementing signal conditioning electronics at the probe tip and interfacing the probe with a custom EIT system. Additional data collection from ex vivo and in vivo prostate and periprostatic tissue is in progress to evaluate the clinical potential of this technology.

## References

[1] USCS Data Visualizations - CDC. (n.d.). Retrieved January 04, 2023, from https://gis.cdc.gov/Cancer/USCS/DataViz.html
[2] World Cancer Research Fund International. https://www.wcrf.org/cancer-trends/prostate-cancer-statistics/
[3] W Lowrance, et al. *J Urol*, 187(6):2087-2093, 2012
[4] R Orosco, et al. *Sci Rep*, 8(1):5686, 2018
[5] O Yossepowitch, et al. *Eur Urol*, 65(2):303–313, 2014
[6] J Silberstein & J Eastham *IJU*, 30(4):423–428, 2014
[7] M Cookson, & S Chang *Urol Oncol*, 28(2):205–209, 2010

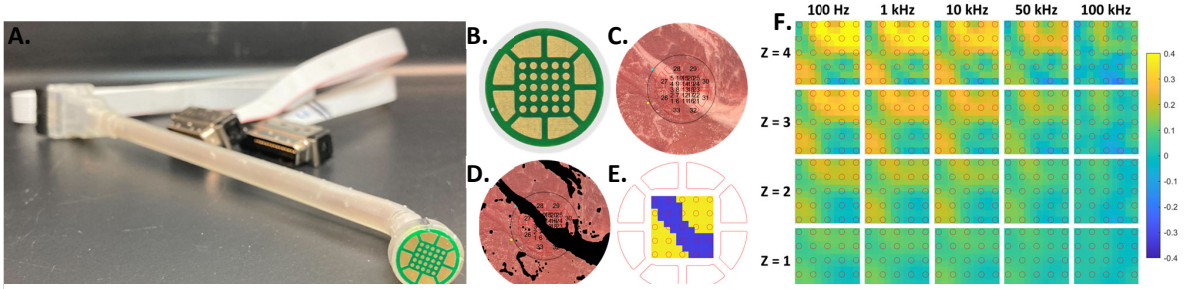


**Figure 1: A)** Custom 3D printed SMA probe and electrode array, **B)** SMA probe electrode array, **C)** image of probed location registered to mesh, **D)** thresholded adipose tissue on ex vivo data set, **E)** binary map of adipose tissue on EIT coarse grid (blue = adipose tissue, yellow = muscle), **F)** Experimental ex vivo bovine tissue 3D EIT difference reconstructions of a strip of fat through muscle at 100 Hz, 1 kHz, 10 kHz, 50 kHz, and 100 kHz (same location as C-E). Yellow is more conductive (muscle), blue is less conductive (adipose). Z is the distance perpendicular to the electrode array. Z = 4 is the XY plane 0.39 mm beneath the electrode array surface, Z = 3 is the XY plane 0.65 mm beneath the electrode array surface, Z = 2 is the XY plane 0.91 mm beneath the electrode array surface, Z = 1 is 1.18 mm beneath the electrode array surface.

# The Entry-Level Electrical Impedance Tomography (EIT) Device You can Assemble without Soldering!

Marcin J. Kraśny[1,2,3], Ross Creaven[1], Ardra Venugopal[3], Eoghan Dunne[1] and Niall Colgan[3]

[1]Translational Medical Device Lab, University of Galway, Ireland m.j.krasny@universityofgalway.ie [2]Smart Sensors Lab, University of Galway, Ireland, [3]Advanced Biological Imaging Lab, University of Galway, Ireland

**Abstract:** EIT is an emerging imaging technique, but access to EIT devices is limited. Previously presented solutions require expensive equipment or advanced electronics knowledge. Here, we present a simple and affordable hardware based entirely on an Arduino Uno board to make EIT universally accessible to everyone.

## 1 Introduction

Electrical impedance tomography (EIT) is a non-invasive spectroscopic imaging modality that applies impedance measurements. The technology has applications in fields ranging from geology through industry to medicine.

However, due to the high price of commercially available EIT devices, wide availability of the technology is prohibited. The equipment required for our previously presented solution [1] also limited the entry level of the approach as it needed a laboratory grade LCR meter, which can be expensive (~€1000 for a basic unit, to ~€3000 for a higher performance device). Therefore, the solution was not suitable and accessible for everyone. Here, we propose a simplified, but full-featured EIT hardware, which only needs one Arduino Uno board as a signal generator and measuring device. Additional hardware components: 2 shift registers & 4 multiplexers (as described in [1]), are all supplied as ready-made modules that can be connected to a prototyping board without (or with minimal) use of a soldering iron. This setup is all you need to get started in the great world of the EIT!

## 2 Methods

The primary operation of a lab-based EIT hardware is the application of a constant current source (signal generation) to a set of electrode pairs around the phantom (e.g., a cylindrical water tank) and a differential voltage measurement from the remaining electrode pairs [2].

### 2.1 Hardware setup

The current source is realised with the current-limiting resistor ($R_S$) connected in series to the digital output of the Arduino Uno. Rs limits the current to ~4 mA across the 10 cm tank filled with 0.9 wt. % saline solution (conductivity of ~16 mS/cm) (see Fig. 1a). Differential voltage measurement is realised with the use of 2 analogue-to-digital converter (ADC) inputs of the Arduino Uno. The whole setup is built with prototype breadboards and standard prototype wires. We use 16 electrodes made of M4 bolts. Rubber seals protect against water leakage.

### 2.2 System control and image reconstruction

Similar to the solution described in [1], the control of the device is developed using the Python language. With this project, we have prepared Jupyter Notebooks [3] that can be easily shared and modified by the user to experiment with the setup. Using the Gauss-Newton reconstruction algorithm implemented in the pyEIT library [4], time difference reconstructed images are displayed directly in the Notebook.

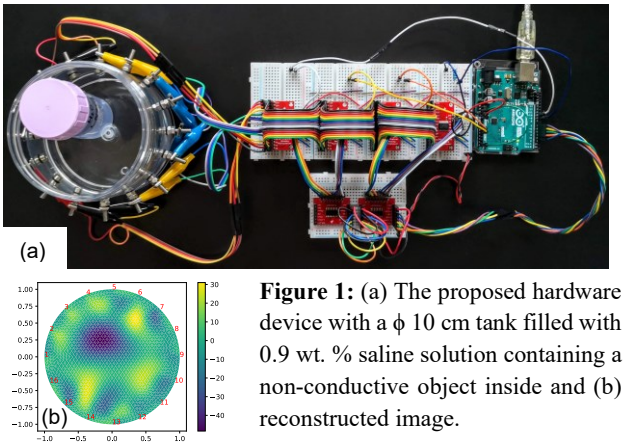


**Figure 1:** (a) The proposed hardware device with a ϕ 10 cm tank filled with 0.9 wt. % saline solution containing a non-conductive object inside and (b) reconstructed image.

## 3 Results & Discussion

To show the capabilities of the constructed EIT system, we present a recording of an image created with the phantom container holding a non-conductive plastic object (ϕ 3.4 cm), as shown in Fig. 1a. Resulting image reconstruction is shown in Fig. 1b.

The speed of the ADC, which with Arduino is limited to ~100 µs per measurement, is the primary drawback of the suggested solution. It also determines the operating frequency of the system to 4 kHz as the differential voltage measurement (between the chosen pair of electrodes) requires two ADC runs. Together with the overhead time (electrodes set-up & image reconstruction) this results in an image refresh rate of about 3.5 seconds.

## 4 Conclusions

In order to lower the high barrier to entry for the application of EIT in various fields, a basic, but fully functional, adaptable, and scalable EIT system is proposed. It requires no electronic hardware development and provides a simple assembly process from *off-the-shelf* accessible, ready-to-use components. The total estimated cost of the setup shown in Fig. 1a is < 100 EUR. The circuit described here could be expanded with a specialised current source and differential voltage measurement modules to further increase the functionality of the device. Future work will apply performance metrics to assess the performance of the system and the quality of the image.

**Acknowledgements**

The project was co-financed by the 2019 NUIG internal grant for new and small equipment fund & by the Disruptive Technologies Innovation Fund, Grant agreement: DT20200189.

**References**

[1] M. J. Kraśny, *et al.*, DOI: 10.5281/zenodo.4635479
[2] A. Adler and D. Holder, DOI: 10.1201/9780429399886.
[3] F. Pérez, and B. E. Granger, DOI: 10.1109/MCSE.2007.53
[4] B. Liu, *et al.*, DOI: 10.1016/j.softx.2018.09.005

# Expandable EIT Electrode Array for Human Vagus Nerve

Ahmad Shah Idil[1], David Holder[1] and Kirill Aristovich[1]

[1]Electrical Impedance Tomography Group, University College London, UK.

a.shahidil@ucl.ac.uk

**Abstract:** Stainless-steel electrodes were developed for use in an expandable vagus nerve cuff for EIT and selective vagus nerve stimulation (sVNS) in humans. Electrical impedance spectroscopy (EIS) was used for characterisation. Three different electrode surfaces were compared (1) laser-patterned; (2) laser-patterned and acid-etched; and (3) PEDOT:PTS electro-coated; no significant impedance differences were observed at the operating frequency (6kHz).

## 1 Introduction

We are planning an acute study of EIT coupled with selective stimulation in the vagus nerve of humans. Non-expandable cuffs were observed to damage nerves in animal experiments. A prototype non-crushing expandable cuff electrode was subsequently developed and tested in porcine models (Fig. 1). Fatigue resistance was a requirement for a cuff that may experience repeated expansion cycles due to post-surgical inflammation and also respiration cycles. Stainless steel is more fatigue resistant than platinum and thus was used as the track material (Fig. 2). The electrochemical properties of pure stainless steel require additional surface treatment such as previously used PEDOT:PTS coating. However, it is unsuitable for use in human studies and therefore alternative approaches should be used.

The purpose of this work was to investigate whether laser-patterning stainless steel used for human-implantable stretchable design will give the electrodes the required electrochemical properties to function as electrodes for EIT & sVNS.

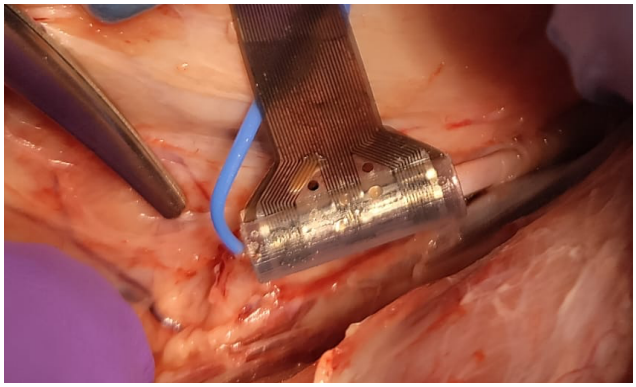

***Figure 1*** *– Expandible cuff electrodes after 12 hours of implantation on pig vagus nerve caused no haematoma*

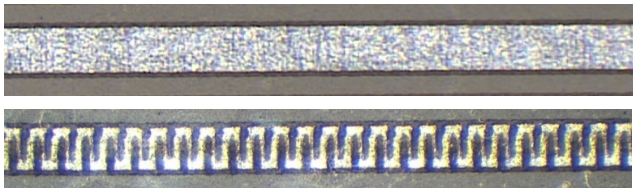

***Figure 2*** *– Non-extensible tracks (top) made into extensible tracks (bottom) by laser cutting metal foils with alternating notches*

## 2 Methods

The devices were fabricated as described in [1]. The metal foil used was 12.5µm 304 stainless steel (Advent Research Materials, UK). The exposed stainless steel electrodes were laser-patterned using bidirectional cross-hatching with 0.1mm gaps at ±45° to the length of the electrode.

The electrodes were 14 pairs of 3×0.35mm rectangles as defined in [2]. Of the 28 electrodes, 5 were chosen using a random number generator. These 5 electrodes were electrochemically characterised at 3 stages: (1) laser-patterned; (2) laser-patterned and acid-etched; and (3) PEDOT:PTS electro-coated as the gold standard. Potentiostatic electrochemical impedance spectroscopy ($1 < f < 100$kHz) was used. The tests were performed on a Solartron Modulab XM (Ametek, US) in phosphate-buffered saline in a 3-electrode set-up: (1) the working electrode was the electrode-under-test; (2) the reference electrode was a KCl-saturated Ag/AgCl electrode (Accumet: cat: #13-620-273); and (3) the counter electrode was a ⌀4mm aluminium bar submerged to a depth of ~40mm. Electrodes were sprayed with 70% isopropanol solution before being submerged in the saline to remove air bubbles.

## 3 Results

The average contact impedance in saline for patterned stainless steel at 6.3kHz was 388±23Ω compared to 375±24Ω for PEDOT:PTS ($P>0.5$, Fig. 3); the impedance of acid-etched stainless steel was 425±37Ω (Fig. 3).

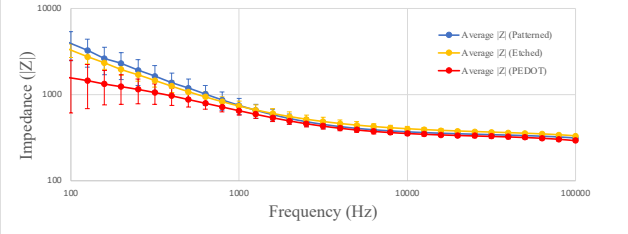


***Figure 3*** *– EIS plots comparing laser-patterned, acid-etched and PEDOT:PTS coated electrodes*

## 4 Conclusions

At the operating frequency of nerve EIT (6kHz) use of laser-patterned stainless steel is possible. Combined with the cuff expandability, this device can be safely implanted in humans, and can thus be an enabling technology for chronic neuromodulation studies in humans, including closed-loop studies that require both recording and stimulation. Work in progress is further characterisation of the electrodes using chronoamperometry at the expected maximum pulsing of the device (1mA/1ms biphasic) and further safety studies in animals.

## References

[1] Chapman et al., 2019, doi: 10.1088/1741-2552/aae868
[2] Aristovich et al., 2021 doi: 10.1016/j.jneumeth.2021.10907

# Shape tracking with mutual inductance from an array of coils

Gavin Dingley[1], Emanuela Semaj[1], Maria Petrou[1], and Manuchehr Soleimani[1]

[1]Authors are with the Electrical and Electronic Engineering Department, University of Bath, UK, ms350@bath.ac.uk

**Abstract:** Real-time tracking of the exterior shape can be valuable in various medical imaging applications. It has also applications in soft robotics. Magnetic induction tomography (MIT) shows great promise in many industrial and medical applications. This study shows how the MIT data is used for shape imaging and topographic shape tracking.

## 1 Introduction

In some medical imaging application the possibility of boundary shape tracking is useful, such as EIT lung imaging [1]. In robotic surgery, the detection of the size and geometry of balloons and catheters is critical [2]. In this work we use the mutual inductance between coils in an array of MIT sensors to determine their relative position in 3D space. This enables the shape reconstruction as well as the quantification of the forces that cause the shape change.

## 2 Method

An 8 channel MIT system consists of (i) an array of equally spaced inductive coils arranged around the object periphery, (ii) a purpose build data acquisition system, and (iii) a host computer is used here. The shape reconstruction module extracts 28 MIT independent measurements with which to perform the reconstruction algorithm, displaying real-time updates of the reconstructed shape. The MIT device will allow 10 frames/s data collection, such that 10 shapes per second can be recovered. In this study, we deal with the geometrical orientation of the coils concerning their mutual inductance. A topological derivative function has been implemented based on a mutual inductance calculation, allowing for both linear (real-time) and fully nonlinear reconstruction of the coil sensor positions. The array sensor can provide information on shapes by tracking the sensors' relative positions in 3D space.

## 3 Results

Figure 1 shows the reconstruction of the *shape changes* on a 2D circular ring array. The reference shape is a circular shape and changes from this reference shape can be tracked. This is done by tracking the displacement in xy directions. Figure 2 shows the reconstruction of *normal forces* applied to a surface that contains the 8 coil sensor array. This is measured by the displacement of the sensors in z direction. Figure 3 shows the dynamical response of a linear array when extended with a soft actuator. This can represent the *shear force* applied to an array of sensors aligned along a line. This is done with tracking displacements in x direction. Calibration steps are needed to link these displacements to the force applied. Due to high sensitivity of the sensors to their own positions, sub mm displacement can be detected using this method.

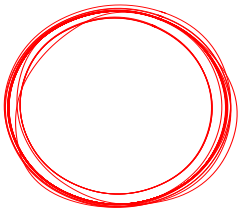

Figure 1: Shape tracking with 8 sensor arranged on a circular array, displacement in xy directions

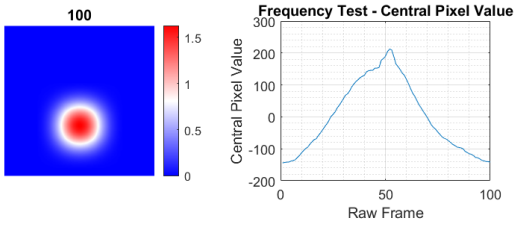


Figure 2: Normal force over 100 frames, showing increasing and decreasing applied force; 8 sensors are distributed on surface of the plane. Image of displacement in z direction and its dynamical tracking in 100 frames

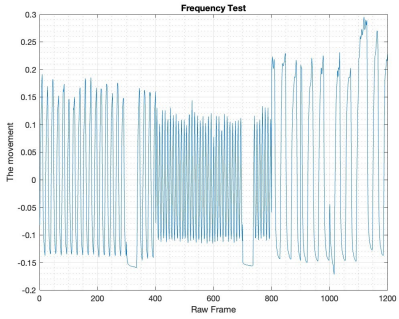


Figure 3: Shear force applied to a linear array at various frequencies. 8 Sensors are arranged in a line, displacement in x direction.

## 4 Conclusions

This paper shows the shape tracking using mutual inductance in a coil array. Sensors are arranged in circular array, distributed on a surface of a plane and in arranged in line, producing a variety of shape recovery methods. A low frequency MIT device will only be disturbed by presence of metallic or magnetic objects, making it a reliable shape tracking device in many situations.

## References

[1] Grychtol B, *et al.*"Impact of model shape mismatch on reconstruction quality in electrical impedance tomography" , IEEE Trans. Med. Imaging 31 1754–60, 2012.

[2] J. Avery, *et al* "Tactile Sensor for Minimally Invasive Surgery Using Electrical Impedance Tomography," IEEE Trans. Med. Robot. Bionics, vol. 2, no. 4, pp. 561–564, Nov. 2020

## Session 6: Brain & Nerve

# Towards the electrical impedance tomography for detection and classification of tumours in human brain

Yahor Zaikou[1,3], Danny Echtermeyer[1], Angelina Nazarenus[2], Tammam Abboud[2], Uwe Pliquett[1]

[1]Institute for Bioprocessing and Analytical Measurement Techniques, Heilbad Heiligenstadt, Germany
[2]Department of Neurosurgery, University Medical Center Göttingen, Göttingen, Germany
[3]yahor.zaikou@iba-heiligenstadt.de

**Abstract:** We present a method for classifying typical tumours in the brain. It utilizes the electrical properties, that are determined using a tetrapolar electrode arrangement in a frequency range between 1 kHz and 10 MHz. After adapting the measured impedance to a corresponding equivalent circuit diagram, its elements are used for classification using a multi-parameter analysis. We present results based on real tissue measurements after ectomy.

## 1 Introduction

Impedimetric methods for diagnostics in neuroscience are employed since decades [3]. Besides, as described in [1] impedance measurement is a promising tool for assistance during operations. However, due to the often used narrow-bandwidth or even one-frequency measurements [3] stable discrimination is challenging. Wideband measurements followed by fitting to proper models allows the extraction of more useful information about the biological tissue. Here we demonstrate this approach.
According to [1] development of EIT system for neurooncology is an extremely challenging task since human scalp and skull attenuate useful signal. It was reported in [2] that no correlations between the tumours and multifrequency EIT measurements could be found after testing seven patients. However, we consider our work as a step towards the development of tomographical methods, for instance with electrode arrays inside the skull during surgery.

## 2 Methods

A tetrapolar system where one current injecting electrode together with a voltage pickup electrode are arranged interdigitally with an electrode surface of 2.4 mm² was mounted at the bottom of the chamber while in a distance of 1.9 mm a second pair of such electrodes was mounted at the sealing. Since the cut tumor slice had a thickness of 2 mm, a good contact with homogeneous pressure was ensured. The chamber was completely filled with the tissue sample. We measured in time domain, making use of a periodic voltage step function as a stimulus. After averaging over ten periods measured signal was transformed into frequency domain and, impedance over frequency range of 1 kHz- 10 MHz was calculated. Moreover, logarithmic averaging in frequency domain was used in order to improve signal to noise ratio.

The model for a biological tissue between electrodes consists of the electrodes including electrode-tissue interface and the bulk tissue. A suitable equivalent circuit as shown in Fig.1 reflects two dispersions: the one related to tissue inhomogeneity but is also influenced by the electrodes (R0,R1 and CPE1) and the one reflecting the cell properties (R2 and CPE2). The dispersion caused by cells is modeled as CPE2 in parallel to R1 which together with R0 yields a Cole element. The second CPE/R – combination results mainly from inhomogeneity of the tissue but is also influenced by the electrode behavior.

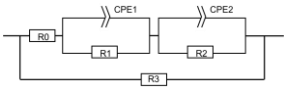


**Figure 1:** Equivalent circuit for discrimination of tumour tissue

The results of several measurement campaigns on different tumor tissue are shown in Fig. 2. Data were scaled on the parallel resistor R3 and subsequently fitted to the two-dispersion circuit. It can be seen, that when using three parameters of R2-CPE2 dispersion, measurements of different tumors usually form different clusters. This can serve as a basis for detailed characterization of tissue.

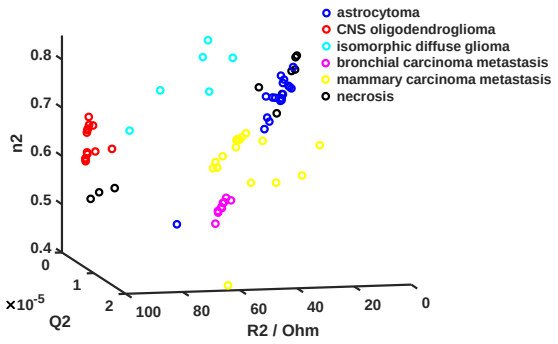


**Figure 2:** Three fitted circuit parameters for impedance measurements. n2 is the distribution parameter for the CPE2.

## 3 Conclusions

The feasibility to discriminate different intracranial tumours by means of impedance spectroscopy is demonstrated. In the future it could serve as a basis for development of a tool for assistance during surgery or even full-scale EIT

## References

[1] Abboud T, Mielke D and Rohde V (2022) Mini Review: Impedance Measurement in Neuroscience and Its Prospective Application in the Field of Surgical Neurooncology. Front. Neurol. 12:825012. doi: 10.3389/fneur.2021.825012
[2] Romsauerova A, McEwan A, Horesh L, Yerworth R, Bayford RH, Holder DS. Multi-frequency electrical impedance tomography (EIT) of the adult human head: initial findings in brain tumours, arteriovenous malformations and chronic stroke, development of an analysis method and calibration. Physiol Meas. (2006) 27:S147–61. doi: 10.1088/0967-3334/27/5/S13
[3] Latikka J, Kuurne T, Eskola H. Conductivity of living intracranial tissues. Phys Med Biol. (2001) 46:1611–6. doi: 10.1088/0031-9155/46/6/3

# Pulmonary function in early Parkinson's disease measured with EIT

Chenxi Zhang[1], Jia Deng[1], Hongying Jiang[1], Zhanqi Zhao[2],

1. Beijing Rehabilitation Hospital of Capital Medical University, Beijing, China. Correspondence to 6jhy@163.com.
2. Furtwangen University, Villingen-Schwenningen, Germany

**Abstract:** We analysed EIT data from 5 patients with Parkinson's disease during tidal breathing. The patients were in various disease stages and had different lung function. We demonstrated that intra-tidal gas distribution showed different patterns characterized the disease stages and maximal voluntary ventilation.

## 1 Introduction

Parkinson's disease (PD) is a progressive motor extrapyramidal disorder leading to disability and immobility. While most prevalent PD symptoms are motor function impairments, non-motor dysfunction may present earlier before motor impairments. PD may cause respiratory dysfunction [1]. However, due to their muscle weakness, spirometry such as forced vital capacity manoeuvre might not be conducted properly, so that the assessment of lung function could be sometimes difficult.
Electrical impedance tomography (EIT) may assess inspiratory efforts [2]. We conducted a preliminary study to assess whether an EIT-based parameter (intra-tidal gas distribution, ITGD) can be used to evaluate the degree of respiratory dysfunction in PD patients.

## 2 Methods

The study was approved by Ethics Committee of Beijing Rehabilitation Hospital, Capital Medical University. A total of 5 PD patients were included (modified Hoehn and Yahr stage, H&Y 1.5-3). The age ranged from 48 to 70 years and body mass index ranged from 19.8 to 25.4 kg/m$^2$. Only one patient was a smoker. Pulmonary function test was performed after oral administration of Parkinson's disease drugs. EIT measurement was conducted during quiet tidal breathing in sitting position. ITGD index calculating the tidal volume distribution during inspiration [3].

$$ITGD_k = \frac{\sum_{ROI}(I_{j,k}-I_{j,0})}{\sum_{Lung}(I_{j,k}-I_{j,0})} \times 100\% \qquad (1)$$

where ROI, region of interest, represents the dorsal regions or ventral regions. Pixel j and i are pixels that belong to ROI and the defined lung regions, respectively. Time point 0 depicts the beginning of inspiration. Inspiration time was divided into 8 equal parts (time point k). Averaging data from 1 minutes were conducted to reduce the variation during spontaneous breathing.
According to a previous study [4], predicted value for maximal voluntary ventilation (MVV) was the most sensitive parameter distinguishing the severity of PD. Therefore, the results were presented qualitatively according to the H&Y stages and MVV% predicted.

## 3 Results

Patients MVV% ranged from 37 to 102% (Fig. 1). The ITGD patterns were very different among patients. For patients with higher H&Y stages and low MVV%, ventral and dorsal distribution within inspiration separated from each other. As the PD severity decreased, the distribution between ventral and dorsal regions became more homogeneous.

## 4 Discussion and Conclusions

Respiratory muscle dysfunction is often presented in PD patients. Consequently, the reduction of the respiratory muscle strength might lead to the deterioration of pulmonary function. In a previous study, we have demonstrated that ITGD might reflect diaphragm activities and predict weaning outcomes [5]. In the present preliminary study, we found that it also reflected the H&Y stage and MVV% in PD patients. Further studies are warranted to confirm this finding.
In summary, the severity of respiratory dysfunction in PD patients might be assessed with EIT during tidal breathing.

## References

[1] EM Guilherme, et al. *J Parkinsons Dis*, 11: 993-1010, 2021.
[2] Z Zhao, et al. *Aust Crit Care*, 2019;32:79-80.
[3] K Lowhagen et al. *Minerva Anestesiol*, 76:1024-35, 2010
[4] C Zhang et al. *Lung*, 200:325-29, 2022.
[5] Z Zhao et al. *Acta Anaesthesiol Scand*, 61:1166-75, 2017
[6] I Frerichs et al. *Front Physiol*, 12:762791, 2021

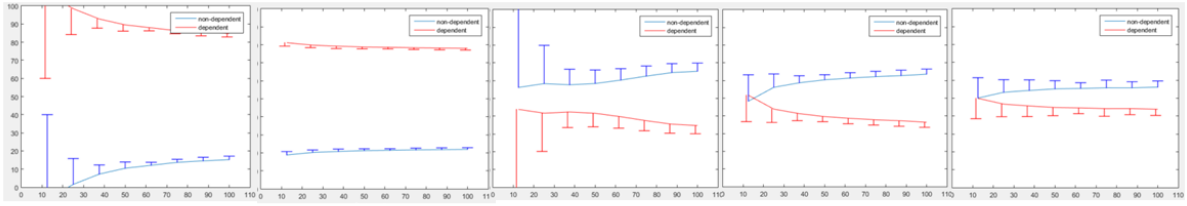

| | | | | | |
|---|---|---|---|---|---|
| H&Y stage | 3.0 | 3.0 | 2.0 | 2.5 | 1.5 |
| MVV% | 37 | 62 | 62 | 98 | 102 |

**Figure 1:** The intra-tidal gas distribution showing ventral (blue) and dorsal (red) regions distribution during inspiration. Mean and standard deviation of the inspirations during 1 minutes at different inspiratory fractions were plotted. Hoehn and Yahr (H&Y) stages and maximal voluntary ventilation (MVV) percent predicted of each individual patients are indicated underneath the plots.

# Imaging circuit activity in the rat brain with an intracortical probe and fast neural EIT

Adam Fitchett[1], Karolina Kozenauskaite[1], Jason Fabbri[2], Justin Hu[2], Kenneth Shepard[2], David S. Holder[1] & Kirill Aristovich[1]

[1]Medical Physics & Biomedical Engineering, University College London, [2]Electrical Engineering, Columbia University
*Correspondence*: adam.fitchett.16@ucl.ac.uk

**Abstract:** Fast neural EIT (fnEIT) with depth arrays has the potential to image neural circuit activity in the brain with high temporal (~1 ms) and spatial (~100 μm) resolution. Here we present preliminary data in the rat brain showing the feasibility of fnEIT to image the propagation of thalamocortical circuit activity.

## 1 Introduction

Novel techniques are required to study the brain at the mesoscopic level of neural circuits. Fast neural EIT (fnEIT) provides images of brain activity at a higher spatial resolution and with more accurate image reconstruction than existing techniques such as local field potentials (LFP) [1].

The **purpose** of this study was to investigate if fnEIT with an optimised depth probe geometry[2] is capable of imaging the propagation of thalamocortical circuit activity in the rat brain at a high enough resolution to distinguish between activity in specific thalamic nuclei.

## 2 Methods

Adult Sprague-Dawley rats were maintained under isoflurane anaesthesia with vitals continuously monitored. A dental drill was used to create a craniotomy window exposing most of the right hemisphere. A 38 electrode epicortical array was placed on the cortical surface with a 4 mm square aperture centred around the primary somatosensory cortex.

The contralateral forepaw, whisker and hindpaw were separately stimulated with current at 2 mA, 2 Hz for 2 mins. Once the presence of somatosensory evoked potentials (SEPs) had been confirmed, the depth probe was inserted into the centre of the aperture to a depth of 8 mm.

The depth probe had 36 PEDOT-coated gold electrodes (500*100 μm) arranged in a 4*3*3 grid, spaced by 2 mm in the vertical axis and 1 mm in the horizontal axes. The electrodes were mounted in nine 120*50 μm silicon shanks with gold tracks.

SEPs were evoked continuously while fnEIT was performed. Current of 20 μA was injected through the set of 35 linearly-independent injection pairs, and the resulting voltages measured. The voltage changes were used to reconstruct conductivity changes on a finite element mesh of rat brain tissue.

## 3 Results

In a preliminary experiment performed in one rat, two distinct brain regions were active after the stimulation of the forepaw (Figure 1). The first appeared at 3 ms after stimulation. centred 2.5 mm posterior and 3 mm lateral to bregma at a depth of 5 mm below the cortical surface. The second appeared 8 ms after stimulation, centred 1.5 mm posterior and 4 mm lateral to bregma at a depth of 2.5 mm below the cortical surface.

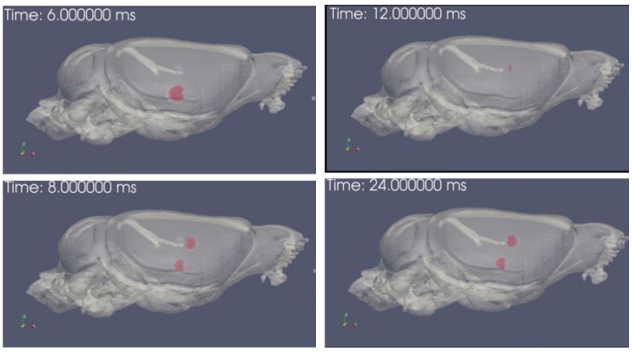


Figure 1: The propagation of thalamocortical circuit activity in the rat brain, as imaged by fast neural EIT. Thalamic activity appeared after 3 ms and cortical activity after 8 ms.

The location, timing and size (maximum diameter 1.5 mm) of the first active region are consistent with activity in the ventral posterolateral nucleus of the thalamus. The size (max diameter 1.4 mm) and timing of the second active region are consistent with activity in the forelimb region of the primary somatosensory cortex, although the region was centred 0.5 mm more lateral than expected. .

## 4 Conclusions

These preliminary data show that fnEIT is capable of imaging thalamocortical circuit activity in the rat brain at a spatial resolution high enough to distinguish activity in specific thalamic nuclei. The spatial error in reconstructing thalamic activity was ≤0.2 mm. This is the first time that circuit activity in the rat brain has been imaged at such a high spatial and temporal resolution.

The higher error in localising cortical activity was likely due to inaccuracy in probe placement. Future work will focus on acquiring statistically significant dataset, improving probe placement, increasing signal-to-noise-ratio, and attempting to image activity during multiple somatosensory stimulation paradigms in the same rat.

## 5 Acknowledgements

The authors would like to than Eric Pollman, Joel Jaso and the staff of the Columbia University CNI and UPenn Quattrone cleanrooms.

## References

[1] A Fitchett, DS Holder, K Aristovich. *Proc. 21st. Int. Conf. Biomed Applications of EIT*, 2021
[2] A Fitchett, A Hewchaiyaphum, DS Holder, K Aristovich. *Proc. Int. Conf. Bioelectromagnetism, Electrical Bioimpedance & EIT*, 2022

# A Pilot Study on Brain EIT Monitoring in External Lumbal Drainage

Bin Yang[1], Shijie Hu[2], XueChao Liu[1], Meng Dai[1], Feng Fu[1]

[1]Department of Biomedical Engineering, Fourth Military Medical University, Xi'an, China, fengfu@fmmu.edu.cn
[2]Neurosurgical Unit of Xijing Hospital, Fourth Military Medical University, Xi'an, China

**Abstract:** This paper presents a pilot study using brain EIT to monitor external lumbar drainage in patients with subarachnoid haemorrhage. Preliminary results show that EIT can detect changes in intracranial impedance caused by cerebrospinal fluid (CSF) drainage and indicate the possibility that EIT may characterize the reduction in CSF volume which reflects the earliest compensation for cerebral edema.

## 1 Introduction

Stroke is one of the diseases seriously endangering human life health, characterized by rapid onset, high mortality, slow recovery, and often led to various degrees of neurological dysfunction. It is the second most common cause of death after ischemic heart disease, but, it ranks first in the Asian regions that have the highest population in the world.

Cerebral edema is the most common complication after stroke and develops in the hours to days after stroke [1]. This pathological increase in brain water and hemispheric volume can lead to mass effect with a rise in local compartmental pressure which may lead to midline shift and neurological deterioration. Up to now the time course and implications of edema formation are not well characterized across the spectrum of stroke. Previous studies focused primarily on measuring and comparing the electrical impedance properties of healthy and edematous brain tissues. However, dynamic brain EIT monitoring in cerebral edema is still unreported.

According to the Monro-Kellie law, intracranial volume should remain constant and volumetric compensation should be achieved by the progressive displacement of cerebrospinal fluid (CSF) from all these CSF-containing spaces for edema-related brain expansion during early cerebral edema. As ΔCSF reflects the earliest compensation for brain swelling [2], we propose that imaging ΔCSF may allow us to recognize cerebral edema at the earlier time points.

## 2 Methods

Six patients with subarachnoid haemorrhage who underwent external lumbar drainage (ELD) were included.ELD was performed by (1) a single lumbar puncture on intermittent drainage via a lumbar catheter and (2) measuring CSF pressure with a spinal manometer and (3) intermittently draining 6-10 mL each hour via a lumbar catheter placed at the level of the foramen of Monro for decreasing ICP slowly when intracranial pressure (ICP) exceeding 340 mm$H_2O$. All patients underwent CT prior to ELD to confirm the presence of open and definable basal cisterns and absence of a space-occupying lesion.

EIT data were measured in real time using an EIT monitoring system FMMU EIT5 developed by our group for brain imaging [3]. 16 electrodes were placed around the head and 1mA-50kHz alternating currents were driven in turn through pairs of electrodes opposite each other and voltages on other adjacent electrode pairs were measured. Each data frame is comprised of 192 independent potentials over 1 s. The reconstruction algorithm is the damped least square method incorporating the patient-specific finite element model which contains the realistic multilayer boundary of the head.

## 3 Results

EIT images of ELD within the first 1 h from all patients had shown continuous impedance changes inside the cranial cavity and Figure A illustrated the image change process for one of the patients. As the amount of lumbar CSF removal increased, blue area in EIT images gradually became deeper in colour, which suggested that the parameters derived from EIT could respond to CSF volume changes in the subarachnoid space.

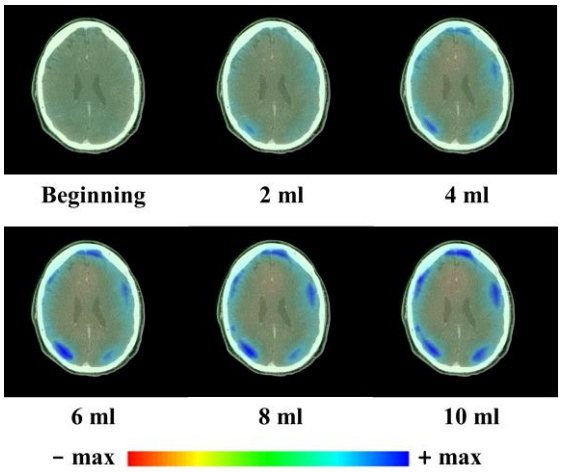


Figure 1: EIT images of lumbar CSF removal

## 4 Conclusions

CSF volumetrics provides quantitative evaluation of early edema formation and ΔCSF could be reflected by EIT. The results suggest that EIT is a potential approach for recognizing the development of cerebral edema and accessing worse neurological outcome.

## 5 Acknowledgements

This work was supported in part by National Natural Science Foundation of China under Grant 51837011 and Key Research and Development Program of Shaanxi Province of China under Grant 2021SF-060.

## References

[1] S Mohanty, SK Swain, C Biswal. A Ann Natl Acad Med Sci, 55:189-192
[2] R Dhar, Y Chen, A Hamzehloo, et al. *Stroke*, 51: 462-467,2020
[3] XT Shi, W Li, F You, et al. *IEEE Sensors Journal*, 18:5974-5984,2018

# Modelling of Neural Imaging with Magnetic Detection EIT (MDEIT)

Kai Mason, Kirill Aristovich, David Holder

Department of Medical Physics and Biomedical Engineering, University College London, London, UK kai.mason@ucl.ac.uk

**Abstract:** Image reconstruction was performed with EIT and MDEIT for 4 simulated perturbations representing neural activity. MDEIT with 1 or 3-axis measurements reconstructed images of higher quality than EIT.

## 1 Introduction

Fast neural EIT with scalp electrodes has been shown to be infeasible, partially due to signal attenuation by the skull [1]. Biological tissue does not attenuate the magnetic field, so MDEIT has the potential to overcome this problem and provide a method of non-invasive neural imaging.

## 2 Purpose

The purpose of this work was to compare reconstructed images of simulated perturbations using MDEIT and EIT for three different noise cases.

## 3 Experimental Design

Noise was simulated for scalp EEG and MEG as follows 1) current measured EEG noise and literature MEG noise during current injection, 2) 60-fold reduction in current source noise and 3) 60-fold reduction in current source noise with a 1000-fold increase in magnetometer sensitivity (Table 1).

## 4 Methods

Forward and inverse modelling was performed on an anatomically realistic finite element model of a human head comprising 3.2M tetrahedral elements and seven tissue types with 32 scalp electrodes of 5mm radius in the EEG 10-20 positions for injection and measurement, 34 additional electrodes placed by eye for measurement and 64 magnetometers at a distance of 7mm from the scalp. AC was injected at 1mA between 31 pairs of electrodes and four perturbations of 3.86cm$^3$ and 1% increase in conductivity were considered (Figure 1). Forward modelling was performed using EIDORS and custom code and the Jacobian was calculated using the adjoint state method in COMSOL. Images were reconstructed using 0$^{\text{th}}$ order Tikhonov Regularisation with noise-based correction and simulated noise at three different levels (Table 1) for 1 and 3-axis MDEIT and EIT. 100 reconstructions were performed and the error was compared using repeated measures ANOVA with multiple comparison tests. The reconstructed images were assessed on their total reconstruction error, comprising volume and position error.

| Noise Case | Magnetic Noise | Electric Noise |
|---|---|---|
| 1 | 21.2fT + $3.67\times10^{-3}$% | 0.0880μV + $3.67\times10^{-3}$% |
| 2 | 21.2fT + $6.57\times10^{-5}$% | 0.0880μV + $6.57\times10^{-5}$% |
| 3 | 0.436fT + $6.57\times10^{-5}$% | 0.0880μV + $6.57\times10^{-5}$% |

Table 1: The noise cases considered in this work. Multiplicative noise is expressed as a percentage of the standing field.

## 5 Results

EIT reconstructed images with a significantly larger reconstruction error than 3-axis MDEIT for all noise cases and perturbations ($P < 0.001$). EIT reconstructed images with a larger reconstruction error than 1-axis MDEIT for all perturbations and noise cases which was significant for all perturbations for noise case 3 ($P < 0.001$) and perturbations 1,2 and 4 for noise cases 1 and 2 ($P < 0.05$). 1-axis MDEIT reconstructed images with larger total reconstruction error than 3-axis MDEIT for 11 of 12 noise-perturbation combinations which were significant in 9 cases ($P < 0.05$). A rank analysis of the Jacobians concluded that the EIT Jacobian was more rank-deficient than the MDEIT Jacobians.

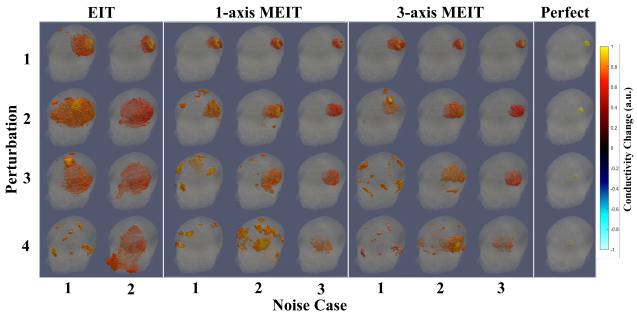


Figure 1: One example of a reconstructed image for each perturbation, noise case and technique considered.

## 6 Discussion

**Summary of Results** On visual inspection, MDEIT reconstructed superior images to EIT and 3-axis MDEIT reconstructed superior images to 1-axis MDEIT (Figure 1). This was supported by an analysis of the reconstruction error and a rank analysis of the Jacobians.

**Does MDEIT reconstruct superior images to EIT?** Yes, MDEIT reconstructed images of superior quality to EIT for all cases considered; this may be explained by the Jacobian for EIT being more rank deficient than for MDEIT, which could correspond to the skull blurring the signal.

**Technical Considerations** The MDEIT Jacobian was calculated using different software to the forward modelling whereas the EIT Jacobian was calculated using the same software as the forward, which could favour the EIT reconstructions.

**Future Work** Future work will include performing MDEIT and EIT in realistic head-shaped saline-filled tanks and *in vivo*.

## References

[1] O. Gilad and D. S. Holder. Impedance changes recorded with scalp electrodes during visual evoked responses: Implications for Electrical Impedance Tomography of fast neural activity. *NeuroImage*, 47(2): 514–522, 8 2009. ISSN 10538119. doi: 10.1016/j.neuroimage.2009.04.085.

# Electrical Impedance Tomography to Assess Pulmonary Function in Amyotrophic Lateral Sclerosis Patients

Allaire Doussan[1], Ethan Murphy[1], Courtney McIlduff[2], Soleil Samaan[2], Hilda Guitierrez[2]
Chebet Yator[2], Sarah Verga[2], Sophie Lloyd[1], Christy Smith[2], Sean Levy[2], Elijah Stommel[3], Seward Rutkove[2], and Ryan Halter[1]

[1]Thayer School of Engineering, Dartmouth College, Hanover, NH, USA, allaire.f.doussan.th@dartmouth.edu
[2]Department of Neurology, Beth Israel Deaconess Medical Center, Boston, MA, USA
[3]Department of Neurology, Dartmouth Hitchcock Medical Center, Lebanon, NH, USA

**Abstract:** Thoracic electrical impedance tomography (EIT) is a promising tool to measure vital capacity in Amyotrophic Lateral Sclerosis (ALS) patients. Multiple linear regressions with EIT and patient data (29 subjects with ALS, 25 healthy controls) have a strong correlation with raw lung volume measured with a spirometer ($r^2$=0.7).

## 1 Introduction

Amyotrophic Lateral Sclerosis (ALS) is the most common degenerative motor neuron disease in adults with an incidence of 2 to 3 people per 100,000 individuals [1]. Primary symptoms of ALS are progressive muscle weakness and spasticity. One of the main clinical metrics for prognosis and planning interventions is pulmonary function testing (PFT) [2]. However, patients with orofacial weakness have unreliable spirometry data due to the inability to form a seal around a mouthpiece [3]. We propose to use an impedance (Z) metric [4] combined with inspiratory and expiratory time constants [5] from electrical impedance tomography (EIT) data as a relative measure of lung vital capacity.

## 2 Methods

### 2.1 Data Collection

EIT data was captured by positioning a custom 32-electrode belt circumferentially around the patient's chest to record during standard of care PFTs. An EIT Pioneer System (SenTec AG, Landquart, Switzerland) with a 3 mA injection current at 195 kHz, 47.8 Hz frame rate, and 4-skip injection pattern was used. Data was collected during 4 types of PFTs: upright forced vital capacity (FVC), supine FVC, upright slow vital capacity (SVC), and supine SVC. Two baseline EIT measurements of normal tidal breathing were recorded for 30 seconds, one at the beginning of the study and one at the end. ALS functional rating scale-revised score (ALSFRS-R) and presence of orofacial weakness was recorded on the day of the study [6]. Healthy controls were age and gender matched to the ALS population (±5 years). All procedures were approved by the Institutional Review Board of Dartmouth Hitchcock Medical Center (DHMC) and subjects provided written informed consent. Data collection was performed at DHMC and Beth Israel Deaconess Medical Center.

### 2.2 Impedance Metric

The Z-Metric looks at the difference in the global maximum and minimum over time of the average Z across a set of IIVV patterns and is normalized by patient specific baseline measurements (eq. 1). This metric was developed as a relative measure of the Z change between maximum inspiration and maximum expiration [5]. $Z_{max}$ is the maximum average Z over time during a PFT effort, $Z_{FEV1}$ is the Z 1 second after $Z_{max}$ and is used to approximate the clinical forced expiratory volume after 1 second (FEV1), $Z_{avg}$ is the average across the average Z for an interval of normal tidal breathing.

$$ZMetric = \frac{Z_{max} - Z_{FEV1}}{Z_{avg}} \times 100 \quad (1)$$

### 2.3 Inspiratory and Expiratory Time Constants

An inspiratory time constant, $\tau_{ins}$, and expiratory time constant, $\tau_{exp}$, were computed from the global average Z during normal tidal breathing intervals using

$$Z(t) = Z_0 \exp(-t/\tau_{exp}) + Z_C, \quad (2)$$

$$Z(t) = Z_1 t^{\tau_{ins}} + Z_D, \quad (3)$$

where constant $Z_0$, $Z_1$, $Z_C$, and $Z_D$ are chosen to match the curves start and end of inspiration/expiration, and $\tau_{exp}$, $\tau_{ins}$ are calculated to best-fit the shape of the curves.

## 3 Conclusions

To date, 29 individuals (20 males, 9 females) with ALS and 25 healthy controls (16 males, 9 females) have been recruited. A multiple linear regression including the Z-Metric, $\tau_{ins}$, $\tau_{exp}$, and height was used to predict the raw upright FVC volume. A strong positive correlation, $r^2$ = 0.70, exists across all participants first visit (n=47) for the multiple linear regression described above. Data from 7 visits was not useable due to bad electrode contact. Future work focuses on continuing data collection to evaluate the use of EIT as a relative measure of vital capacity in patients with and without orofacial weakness.

## 4 Acknowledgements

The authors would like to express their gratitude to the clinical staff that made this work possible. This work was supported by the NIH (1R21NS118434-01).

## References

[1] O Hardiman, et al. *Nat Rev Dis Primers*, 3:17071, 2017
[2] A Pirola, et al. *Clin Neurol Neurosurg*, 184:105456, 2019
[3] G Pellegrino, et al. *Respir Med*, 176:106277, 2021
[4] B Munir, et al. *Physiol meas*, 41(4):044005, 2020
[5] C Strodthoff C, et al. *Physiol meas*, 43(10):10.1088/1361-6579/ac9450, 2022
[6] J Cedarbaum, et al. *J Neurol Sci*, 169(1-2):13–21, 1999
[7] P Quanjer, et al. *Eur Respir J*, 40(6):1324–1343, 2012

# Application of Capacitively Coupled Electrical Impedance Tomography (CCEIT) in Brain Imaging

Yandan Jiang[1], Manuchehr Soleimani[2] and Baoliang Wang[1]

[1] State Key Laboratory of Industrial Control Technology, College of Control Science and Engineering, Zhejiang University, Hangzhou, China, ydjiang@zju.edu.cn

[2] Engineering Tomography Laboratory (ETL), Department of Electronic and Electrical Engineering, University of Bath, Bath, UK, M.Soleimani@bath.ac.uk

**Abstract:** Capacitively coupled electrical impedance tomography (CCEIT) is a new contactless alternative of electrical impedance tomography (EIT). This work focuses on the application of CCEIT in 3D brain imaging.

## 1 Introduction

Electrical impedance tomography (EIT) has been widely studied and applied in medical field since it was proposed. Due to the various advantages such as safe, fast and portable, EIT is now a very promising technique for brain imaging [1]. However, traditional EIT suffers from the electrode-skin contact impedance problem, which is usually high and quite variable or sensitive due to body surface condition and body movement [2]. In the past decades, efforts have been made to model or calculate the contact impedance, but the adverse influence of the contact impedance is still exist. Capacitively coupled electrical impedance tomography (CCEIT) is proposed as a contactless alternative of EIT, which provides a new effective and totally contactless approach for biomedical applications [3]. Our previous work has introduced CCEIT to biomedical applications [4-5]. This work focuses on the application of CCEIT in 3D brain imaging. First, a 3D CCEIT phantom will be designed and optimized for brain imaging. Then, mathematical model of the CCEIT phantom will be established to solve the forward problem and get the sensitivity matrix. Finally, image reconstruction performance of the 3D CCEIT in brain imaging will be investigated.

## 2 Measurement Principle

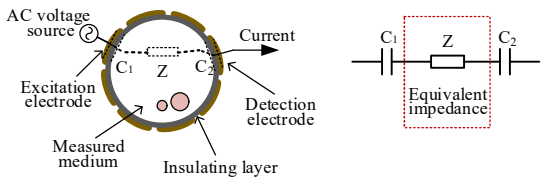


**Figure 1:** Measurement principle of CCEIT.

Fig.1 shows the measurement principle of CCEIT (assume that there are 8 electrodes visible on the cross section), where an insulating layer is introduced to keep the electrodes and the measured biomedical medium not in direct contact. For each measurement electrode pair, the excitation electrode and the detection electrode will respectively form coupling capacitances $C_1$ and $C_2$ with the insulating layer and the measured medium. The measured biomedical medium can be regarded as an equivalent impedance Z. When the excitation AC voltage applied, the current reflects the conductivity distribution of the measured medium can be measured.

## 3 Forward Modelling

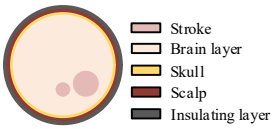


**Figure 2:** The geometric model of brain.

Fig. 2 shows the geometric model of brain, including the internal brain layer (0.15 S/m), the stroke (0.6 S/m), the skull (0.06 S/m), the scalp (0.44 S/m) and the insulating layer (0 S/m). Based on the geometric model, the mathematical model of CCEIT is developed as

$$\begin{cases} \nabla\cdot((\sigma(x,y)+jw\varepsilon(x,y))\nabla\phi(x,y))=0 & (x,y)\subseteq\Omega \\ \phi_a(x,y)=V_0 & (x,y)\subseteq\Gamma_a \\ \phi_b(x,y)=0 & (x,y)\subseteq\Gamma_b \\ \dfrac{\partial\phi(x,y)}{\partial\vec{n}}=0 & (x,y)\subseteq\Gamma_c,(c\neq a,b) \end{cases} \quad (1)$$

where $\sigma(x,y)$, $\varepsilon(x,y)$ and $\phi(x,y)$ are the spatial conductivity, permittivity and potential distributions. $w$ is the angular frequency of the AC voltage source. $\vec{n}$ is the outward unit normal vector. $\Gamma$ represents the boundary of the electrode. $a$, $b$ and $c$ represent the excitation electrode, detection electrode and floating electrodes, respectively. With this model, the sensitivity matrix is calculated.

## 4 Image Reconstruction Results

Experiments were carried out with saline to simulate the brain layer and sodium chloride mixture to simulate stroke and other parts of the brain model. Fig. 3 shows the image reconstruction results reconstructed by LBP at 15 MHz. Results show that the reconstructed images are in accordance with the practical medium distribution.

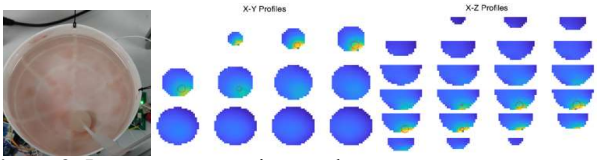


**Figure 3:** Image reconstruction results

## 5 Conclusions

This work verifies the feasibility and potential of CCEIT in 3D brain imaging.

## References

[1] T Dowrick, et al. *Physiol Meas*, 36(6): 1273-1282, 2015.
[2] V Kolehmainen, et al. *IEEE Trans Med Imag*, 27(10): 1404-1414, 2008.
[3] BL Wang, et al. *IEEE Trans Instrum Meas*, 62(5): 1017-1024, 2013.
[4] YD Jiang, et al. *IEEE Access*, 6: 27069-27079, 2018.
[5] YD Jiang, et al. *IEEE Trans Med Imag*, 38(9): 2104-2113, 2019.

# Author Index

EIT 2023

# Thank You!

See you soon!